Development of Energy Efficient Tunable Solid-State Lasers with Low Power Consumption

by

Ersen Beyatlı

A Thesis Submitted to the
Graduate School of Sciences and Engineering
in Partial Fulfillment of the Requirements for
the Degree of

Doctor of Philosophy
in
Electrical and Electronics Engineering

Koç University

January 2014

Koc University

Graduate School of Sciences and Engineering

This is to certify that I have examined this copy of a doctor of philosophy thesis

by

Ersen Beyatlı

and have found that it is complete and satisfactory in all respects,

and that any and all revisions required by the final

examining committee have been made.

Committee Members:

_____

Alphan Sennaroğlu, Ph.D. (Advisor)

_____

M. İrşadi Aksun, Ph.D.

_____

Özgür Müstecaplıoğlu, Ph.D.

_____

Sarper Özharar, Ph.D.

_____

Ümit Demirbaş, Ph.D.

Date: _____

ABSTRACT

The work presented in this thesis aims at the development of highly efficient and low-cost tunable solid-state lasers at different wavelength regions and in different operation regimes. We show that employing inexpensive, high brightness laser diodes as pump sources greatly reduces the cost of the systems. By utilizing low-threshold cavity designs, we also demonstrate experimentally that the laser performance can be greatly enhanced. Moreover, we have also designed and developed these systems in a very compact manner for easy integration into other measurement systems. To achieve this goal, at first, we developed a laser cavity design software that simplifies the determination of the optimum cavity and beam parameters for the laser. Then, we applied these techniques to different laser systems operating in different wavelength ranges.

In the experiments, we first developed low-threshold 2-μm lasers based on the Tm^{3+} doped YAG and LuAG crystals. These lasers were pumped with single-mode 785-nm laser diodes which are widely used in optical data storage (CD-ROM technologies). In these systems, we obtained continuous-wave power efficiencies approaching the theoretical limit. Moreover, by incorporating saturable absorbers into the cavities, we obtained Q-switched mode-locked pulses with pulse energies in the pico-joule levels. In particular, 22% and 19% slope efficiency was obtained from continuous-wave laser experiments of Tm:YAG and Tm:LuAG lasers, respectively, where the theoretically expected limits for these systems were 23% and 21%. In the Q-switched mode-locked experiments, the pulse energies around 250 pJ were obtained.

In another set of experiments, we applied the low-threshold design principles to characterize the self-q-switching properties of a Cr^{3+} doped LiCAF laser by using 660-nm single-mode pump diodes used in DVD-ROM technologies. Here, we obtained Q-switched pulses with μJ energies without adding any extra modulators into the resonator. In these

experiments, we obtained 4 microsecond-long pulses at a repetition rate of 24 kHz. 400 mW of peak power and 1.6 μJ of pulse energy were obtained at the wavelength of 795 nm in this configuration. Moreover, we estimated that the effective modulation depth of the self-Q-switching mechanism was 0.5%.

We then employed recently developed high-brightness tapered diode lasers as pump sources to excite the Alexandrite gain medium and obtained power efficiencies close to the theoretical limit at the output wavelength of 755 nm. In particular, with 900 mW of pump power, we obtained 200 mW of continuous-wave output power. In this system, the intrinsic slope efficiency was estimated to be 63%, where 65% is the theoretical limit for Alexandrite lasers.

In the last part of the thesis, we discuss a series of experiments which investigated efficient femtosecond pulse generation from Cr:LiSAF lasers by using single-mode and tapered diodes as pump sources. In particular, we obtained as short as 13 fs and 14.5 fs pulses with 200 pJ and 940 pJ of pulse energy from single-mode diode pumping and tapered diode pumping configurations, respectively. Finally, temperature dependence of spectroscopic properties and laser performance of an Alexandrite laser was investigated by pumping with single mode-diodes. In these experiments, the laser wavelengths can be tuned from 736 nm to 823 nm and as low as 13 mW of lasing threshold pump power could be achieved

All of these experiments described in this thesis clearly show that the low-threshold cavity design approach is a very effective method in the development of low-cost, energy efficient tunable solid-state lasers in the 700-2100 nm wavelength region of the electromagnetic spectrum and should find numerous applications in biomedical optics, spectroscopy, and materials processing.

ÖZET

Bu doktora tezinde, farklı dalgaboylarında ve rejimlerde çalışan enerji verimliliği yüksek, düşük maliyetli dalgaboyu değiştirilebilinen katı hal lazerlerinin geliştirilmesi amaçlanmıştır. Yüksek parlaklığa sahip ekonomik lazer diyotlarının pompa kaynağı olarak kullanımı ile lazer sistemlerinin maliyeti önemli ölçüde azaltılmıştır. Düşük pompa eşik güçlerinde çalışmaya izin veren kavite tasarımı ile lazerlerin performansı arttırılmıştır. Bununla birlikte oluşturulan sistemler, gerekli alanlarda kullanımını kolaylaştırmak için kompakt bir şekilde tasarlanmıştır. Bu amaçla ilk once en uygun dizayn parametrelerinin tespitini kolaylaştıran bir bilgisayar program geliştirildi. Daha sonra bahsedilen bu teknikler, değişik dalgaboylarında çalışan lazer sistemlerine uygulandı.

Deneylerde ilk önce, 2 μm bölgesine ışıma yapan Tm^{3+} iyonları katkılı YAG ve LuAG lazerleri geliştirildi. Bu lazerler cd-rom teknolojisinde kullanılan tek-kipli 785 nm'de ışınım yapan lazer diyotlarıyla uyarıldı. Bu sistemler ilk olarak sürekli-dalga rejiminde çalıştırıldı. Deneylerde Tm:YAG lazerinden teorik limit olan %23'e çok yakın olan %22 güç verimliliği elde ediliriken; Tm:LuAG lazerinde elde edilen %19 çıkış gücü verimliliği teorik limit olan %21'e oldukça yakındır. Daha sonra bu sistemlerde doyabilen soğurma özelliği olan yarıiletken Bragg geçirgenler kullanarak Q-anahtarlamalı kip-kilitli darbeler elde edilmiştir. Bu darbelerin tepe güçleri ortalama 250 pJ civarındadır.

Bu tez kapsamında, düşük pompa eşik gücü tekniği ve DVD-rom teknolojisinde kullanılan tek-kipli 660 nm de ışıyan lazer diyotları kullanılarak Cr^{3+} katkılı LiCAF lazerlerinin kendiliğinden Q-anahtarlamalı özelliği karakterize edilmiştir. Bu sistemlerde herhangi bir modülasyon elemanı kullanmadan μJ seviyesinde darbeler elde edilmiştir. Elde edilen darbeler 795 nm'de 4 mikrosaniye genişliğine ve 24 kHz tekrarlanma frekansına sahiptir. Söz konusu darbelerin tepe güçleri 400 mW ve darbe enerjileri 1.6

μJ'dür. Bununla birlikte sistemin %0.5 modülasyon derinliğine sahip bir doyabilen yarıiletken özelliğine sahip olduğu gözlemlenmiştir.

Daha sonra, yeni geliştirilmiş yüksek parlaklığa sahip daralan kılavuz yapılı diyotlar kullanılarak Aleksandrite lazerleri çalıştırılmış ve teorik limitlere yakın güç verimliliği gözlemlenmiştir. Bu sistemde 755 nm'de 900 mW pompa gücüyle 200 mW çıkış gücü elde edilmiştir. Bununla birlikte sistemin gerçek verimliliği %63 olup teorik limit olan %65'e çok yakın sonuç elde edilmiştir.

Bu tezin son kısmında, Cr:LiSAF lazerlerinin tek-kipli ve daralan kılavuz yapılı diyotlarla uyarılarak kip-kilitli rejimindeki çalışmalarımızdan bahsedilmiştir. Bu sistemlerde tek-kipli diyotlarla 13 fs genişliğinde ve 200 pJ darbe enerjisine sahip darbeler elde edilmiştir. Daralan kılavuz yapılı diyotlar kullanılarak 14.5 fs genişliğinde 940 pJ darbe enerjisine sahip kip-kilitli darbeler elde edilmiştir. Son olarak, Aleksandrite lazerinin değişik sıcaklıklardaki spektroskopik özellikleri ve lazer performansı tek kipli diyotlarla uyarılarak incelenmiştir. Bu sistemin çıkış dalgaboyu 736 ile 823 nm arasında değiştirilmiştir. Aynı zamanda bu sistemin 13 mW ile çalışması da gözlemlenmiştir.

Bu tez kapsamında tamamlanan çalışmalar, düşük pompa eşik gücünde çalışmaya izin veren kavite dizayn yönteminin 700-2100 nm dalgaboyları arasında düşük maliyetli ve enerji verimliği yüksek katı hal lazer sistemlerinin geliştirilmesine imkan veren çok etkili bir yöntem olduğunu göstermiştir. Bu yöntemle üretilen lazerlerin biyomedikal optik, spektrsokopi ve madde işlemeciliği gibi alanlarda önemli bir rol oynayacağı düşünülmektedir.

Dayan be ersen, biçare değilsin Yaradan sana yar
Kimsesiz değilsin, yanında kimsesizler kimsesi var
Biliyorum, sığmazsın hiçbir yere, bu sevdayla dünya sana dar
Ama dayan be ersen, her karanlık gecenin mutlak bir sabahı var

Mevlana

en başından beri benimle olana (hatta çok daha öncesinden beri)

ACKNOWLEDGMENTS

Obtaining a Ph.D. degree is not an easy and straightforward process. In fact, it can be considered as a granted gift. After many continuously hardworking years I earn this degree. However, this achievement does not belong to me only. It is a result of collaborative works with the right people and institutions. In here, I want to express my deepest gratitude's to them. In fact, they deserve more than my thanks, but this is all I can do for them.

First and foremost, I want to present my most special thanks to my supervisor Alphan Sennaroğlu for providing me this rare opportunity to conduct research in one of the best laboratory Koç University Laser Research Laboratory. I appreciate his patience, encouragement and support during my doctorial program. Also his vision, experience and enthusiasm significantly improve my research, skills and knowledge. I am very grateful I met such a professor and I hope his guidance will be with me rest of my career.

I would like to also my deepest thank to Ümit Demirbaş. Without him this thesis will not be as complete as it is right now. His academically contributions, advices, insights in many experiments are priceless. However, together with his wife Meryem Demirbaş, their emotional support is even more priceless. I hope our friendship and collaborations will continue rest of our lives.

I would like to especially thank to Adnan Kurt. Without his technical contributions in our researches, I cannot reach at this level. He is also the only person who makes me truly feel that I am an electrical and electronics engineer and I want this feeling to continue forever.

I would like to thank to M. İrşadi Aksun. His support and guidance in the early phase of my graduate program shape my academic career. Moreover, his belief on me was one of the milestones of my life that makes me continue my Ph.D. I also especially thank to him for serving in my thesis committee despite his busy schedule.

I would like to thank to also Özgür E. Müstecaplıoğlu and Sarper Özharar for their advices and support. And I wish to thank to them for serving on my research qualification and Ph.D. committee.

I want to express my deepest appreciation to my master Hüseyin Çankaya. I learned a lot when he was trying to transfer his laser skills and experiences to me. And also I want to thank to my second master Natali Çizmeciyan for continuing this support after he left.

The friendly environment in our group motivates me a lot for research. I want to express my deepest thanks to them, Işınsu Baylam, Ferda Canbaz, Can Cihan, İsmail Yorulmaz and former member of our group Adil Tolga Görgülü.

I also want to thank some of my friends from Bilkent University. Beginning from my closest friend Abdullah Bülbül, they are Gamze Bülbül, Emre Kacar, Eren Algan, Onur Küçüktunç, Safa Çağatay Çelenk and Selman Özbayat. Their valuable friendship keeps me in line throughout my last decade.

I also want to thank some my friends from Koç University and Antalya International University, Mustafa Eryürek, Necati Vardar, Mehdi Yavuz Yüce, Yasin Karadağ, Gül Seda Ünal, Emine Pınar Karabulut, Gökçen Mahmutoğlu, Arif Engin Çetin, Hüseyin Rahmi Seren, Ömer An, İbrahim Hocaoğlu, İlyes Baali for their friendship.

I would like to thank some of our outside collaborators Alfred Leitenstorfer, Franz X. Kaertner, Bernd Sumpf, Götz Erbert, Li-jin Chen and Ramez Hamed for providing the necessary equipments and devices for our experiments.

I would like to express my deepest gratitude to TUBİTAK for their financial support during my doctorial process and Koç University for giving me this rare opportunity.

Beginning from Antalya International University, I want to thank Teknofil Inc., Ferdinand-Braun Institute, Konstanz University, DESY, Marie Curie Foundations, Alexander von Humboldt and RLE group in MIT for their financial support and providing some of the component for our projects.

Behind every success there is a family. Last but perhaps most, I want to express my deepest gratitude and love to my family, my mother Leyla Beyatlı, my father Kemal Beyatlı, my brother Muhammed Habib Beyatlı, my closest cousin Barış Süleymanoğlu, my aunt Buşra Kutub and all of my relatives. Their prayer for me was what sustained me thus far.

TABLE of CONTENTS

LIST of TABLES

LIST of FIGURES

NOMENCLATURE

A	element of the ray transfer matrix / proportionality constant / cross-sectional area
A_{eff}	effective absorbance
A_{max}	maximum absorbance
B	element of the ray transfer matrix / brightness of a diode
c	speed of light
C	element of the ray transfer matrix
cw	continuous-wave regime
d	length of a gain medium / distance
D	element of the ray transfer matrix
Δv	free spectral range
$\Delta\lambda$	spectral bandwith
E_x	energy level of |x> state / Electric field amplitude of the x^{th} mode
$E_x(t)$	Electric field variation of the x^{th} mode
f	focal length of a thin lens
f_{rep}	repetition rate
$g_D(\lambda)$	spectral intensity distribution of a diode
G_o	small-signal gain
G_{th}	fractional threshold gain
h	Planck's constant
HR	highly reflecting mirror
k	wave vector
L	cavity length / cavity loss
M	number of modes oscillating inside a cavity

M^2	M-square factor of a Gaussian beam
M_T	ray transfer matrix
n	refractive index
η	slope efficiency
$n(I)$	intensity dependent refractive index
η_0	intrinsic slope efficiency
n_2	non-linear refractive index
η_A	pump beam absorption
OC	output coupler
$P(z)$	axial phase factor
PBS	polarizing beam splitter
P_{out}	output power
P_{sat}	saturation power
P_{th}	threshold pump power
$q(z)$	Gaussian q-parameter
Q_o	modulation depth
r	transverse radial coordinate / ray height with respect to optical axis / ratio of the pump power to the threshold pump power
R	radius of curvature of a curved mirror
$R(z)$	radius of curvature of the equiphase surfaces
$\bar{r}_x$	ray vector
SMD	single-mode diode
t	time
T	transmission of the output coupler / crystal transmission
TD	tapered diode
v_x	resonance frequency of the x^{th} mode

w_R	relaxation oscillation frequency
z	longitudinal coordinate
z_0	Rayleigh range
z_f	focus location of a Gaussian beam
θ	ray angle
λ	wavelength
σ_e	emission cross-section
τ_f	fluorescence lifetime
τ_p	pulse width
$\phi_x(t)$	phase of the x^{th} mode
$\omega(z)$	spot size distribution
ω_0	beam waist of a Gaussian beam

Chapter 1

INTRODUCTION and MOTIVATION

The invention of the first ruby laser in 1960 triggered intensive research on solid-state lasers [1]. Since then, different gain materials and pumping techniques have been investigated to obtain desired properties i.e. special wavelengths, pulse widths, resonator frequencies and so on. Providing narrow line width and diffraction limited beams makes these systems an ideal light source in many scientific and industrial areas, such as medical procedures, computer technology, material processing and spectroscopy. These world-wide applications, especially in medical operations, made the energy and cost efficiency of the laser systems two very important parameters to optimize. For this purpose, different pumping techniques and resonator designs are tested to achieve the most efficient and most economical laser architecture.

The development of low-threshold, diode-pumped, solid-state lasers has attracted a lot of interest in recent years because of their energy and cost efficiency properties. Since the cost of the pump laser increases with the output power, a considerable reduction of the overall system cost becomes possible with the use of special resonator geometries that allow low-threshold operation. If diode pump sources are further employed, the laser can be constructed in a compact layout, hence enabling its large-scale production and integration into other measurement systems. Recently, this approach was applied to the development of low-cost, low threshold chromium-doped colquiriite lasers, which can be broadly tuned around 800 nm. By using commercially available single-mode AlGaInP laser diodes that operate near 660 nm and produce 100-150 mW power, an efficient low-threshold tunable operation was demonstrated with Cr:LiCAF, Cr:LiSAF, and Cr:LiSGAF lasers in the 754-1042 nm range [2-4]. Along with these initial promising systems, there

occurs an increasing demand for similar low-cost, low-threshold solid-state lasers operating at different wavelengths for a wide range of applications. Additionally, the results that are obtained from Cr:Colquiirite laser systems can be further examined, because of having the self-modulation properties of Cr^{3+} ions in several hosts [5, 6].

One of the most desirable wavelength regions is the 2 μm band, due to the important role that it plays in urological cancer treatment, as demonstrated by recent studies [7-9]. One of the most commonly used schemes employs thulium-doped gain media to access this wavelength range. Depending on the particular host used, the central excitation wavelength varies between 775 and 810 nm [10-20] and laser tuning can be obtained over the wavelength range of 1.8-2.2 μm. Typically, when 4-mirror resonator geometries are used, tunable Ti:sapphire lasers are used to excite these gain media [10, 15, 16]. Other pumping schemes include flash lamp pumping [21], and medium- or high-power diode pumping [22-26]. In the case of high-power diode pumping, multi spatial-mode diodes were used with large pump volumes and the laser operation typically occurred at high threshold powers [26]. These techniques bring electrical and economic inefficiency to the laser systems and make more difficult the integration into the necessary fields. One of the best pumping alternatives for those systems is pumping with low-cost single-mode laser diodes by employing architectures that allow low lasing thresholds. In this method, an economic advantage could be obtained by using low-cost single-mode laser diodes, and superior electrical efficiency could be achieved as a result of low-lasing threshold.

With the development of tapered diode technologies, more powerful diodes (1 W) that can provide an almost single-mode beam around 670 nm were used for pumping the same Cr:colquiirite systems. As a result, further increase in the output laser power could be obtained [27]. However, due to wavelength limitations in the Cr:colquiirite crystals, alternative systems will be more attractive for different applications. For example, Alexandrite (Cr^{3+}:$BeAl_2O_4$) systems mainly used in hair removal operations have

maximum gain at 750 nm, where Cr:colquiirite systems have lower power in this wavelength region. This region is quite important for optimum excitation of several widely used fluorophores in multiphoton microscopy [28-31]. As a result, development of a low-cost alexandrite laser has the potential to revolutionize the field of biomedical imaging based on multi-photon microscopy.

In this thesis, low-threshold diode-pumped operation of several solid-state laser systems was examined. With this technique, laser output was obtained in the wavelength ranges of 724-935 nm and 1935-2045 nm. Furthermore, different regimes of operation such as continuous-wave and self-Q-switching were demonstrated with different systems.

Chapter 2 provides the necessary background on solid-state lasers. The fundamental aspects of laser operation and resonator analysis for designing an efficient low-threshold cavity are reviewed.

In chapter 3, a stand-alone application powered in MATLAB is presented, based on the resonator design rules described in Chapter 2. This program is designed for determining the optimum cavity parameters in different types of resonator architectures.

Chapters 4 and 5 describe the application of the low-threshold laser design to 2 micron lasers. Tm^{3+} doped YAG and LuAG hosts were used as the gain media to generate laser radiation. Chapter 4 examines the continuous wave operation of these lasers in detail, while in chapter 5 describes their passively Q-switched operation.

In chapter 6, based on the self-pulsing properties of Cr^{3+} ions in several hosts, the development and the results of the self-Q-switched Cr:LiCAF lasers were investigated experimentally. In this study, the curved mirror separation of the 4-mirror resonator was varied to initiate pulsed operation at discrete mirror locations.

Chapter 7 describes the first demonstration of tapered diode pumping of Alexandrite lasers. This method provides an alternative approach to power scaling in Alexandrite lasers, based on the most recent developments in tapered diode technology.

In chapter 8, the collaborative experiments conducted with other members of the Laser Research Laboratory are briefly described. More specifically, a single mode diode pumped Alexandrite system with high intrinsic slope efficiency was developed to explore the possibility of building a low-cost version of this laser system. In addition, Kerr-lens mode locking of a diode-pumped Cr:LiSAF laser was investigated by using a Gain Matched Output Coupler (GMOC), which increases the effective modulation depth during Kerr-lens mode-locking. Successful application of the GMOC technology to Cr:LiSAF laser yielded pulses as short as 13 fs.

Chapter 2

THEORETICAL BACKGROUND

Lasers are optical oscillators that combine optical amplification with positive feedback provided by highly reflecting mirrors to produce highly directional and intense light beams. The amplification occurs in the gain medium of the oscillator. Then, with the help of a stable resonator, the coherent light enhancement occurs in the system. In the first section of this chapter, the amplification process will be described briefly. Next, a stable resonator design that produces efficient lasing will be described. Once the laser operation is obtained, the lasers can operate in two different regimes - continuous wave or pulsed. Moreover, the pulsed regime can be divided into two different categories depending on their pulse durations and repetition rates, i.e. q-switching and mode-locking. In the last section of this chapter, these regimes will be described shortly.

2.1. Optical Amplification

As the abbreviation of the LASER (light amplification by stimulated emission of radiation) implies, lasers are the systems that optically amplify (i.e. increase or enhance) the light waves. To understand the amplification process, first we need to understand the interaction of light with atoms or molecules.

The atoms or molecules have energy levels and they tend to occupy the lowest energy states (ground state) in equilibrium. Consider a 4-level energy system (Fig. 2.1.1). When the light at a certain frequency comes in, (three photons are incident on these atoms in Fig 2.1.2 a), they will interact with the atoms and excite them to a higher energy state (state |3> in the Fig. 2.1.1. b). If the wavelength (frequency) of the light meets the resonance

condition, in other words, if the photon energy is nearly equal to the energy separation between the levels, the atoms are excited from one level to another level. When the atom is excited, it takes energy (or photons) from the light, since the atom now has a higher energy than it started with. As a result, the light gives up its energy to the atom and therefore has less energy when it leaves the medium. This process is called absorption.

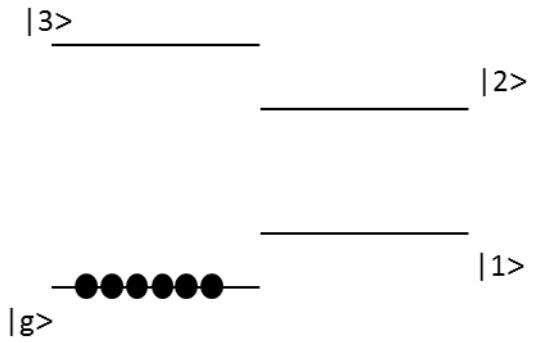

Figure 2.1.1 Energy States for a 4-Level System

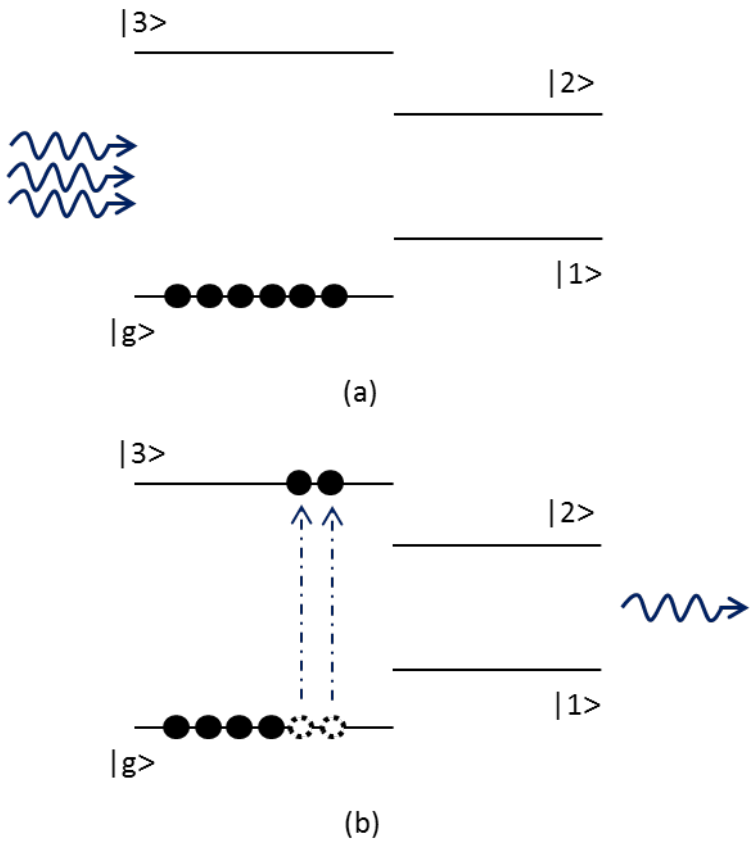

Figure 2.1.2 Absorption Scheme

The resonance frequency (v) for maximum absorption is given by

$$\nu = \frac{E_3 - E_g}{h} \tag{2.1.1}$$

where E_3 and E_g are energy levels of the states |3> and |g>, respectively, and h is the Planck's constant. In a laser system, the pumping system that provides light at this absorption frequency is chosen to obtain maximum transfer of atoms from the ground level to the upper energy level. Once the pump is determined, it is arranged for the most effective excitation with a proper focusing lens system. The procedure for this lens combination is described later in this chapter.

When the atoms are excited, they decay from state |3> to state |2>, and then from |2> to|1> until the atoms finally go down to the ground state |g> (Fig. 2.1.3). In each transition, the atoms emit light at the transition frequency in random directions. This random decaying process is called spontaneous emission.

For a 4 level system, the decays (or emission) from |3>-|2> and |1>-|g> states are very fast. On the other hand, the emission from |2>-|1> states is relatively slow. This decaying time is called the fluorescence lifetime (τ_f). The resonance frequency in this decay is expressed as

$$\nu = \frac{E_2 - E_1}{h} \tag{2.1.2}$$

where E_2 and E_1 are energy levels of the states |2> and |1>, respectively. If a photon at the decaying frequency (Eq. 2.1.2) comes into the crystal, the atoms in state |2> will be stimulated to decay to state |1> and emit light in the same direction as the incoming light. This process is called stimulated emission. This is where the optical amplification occurs because the number of incoming photons (the energy of the incoming light wave) is increased at the end of the crystal and the direction of the new photons is the same as the incoming ones (Figure 2.1.4). When the number of atoms in the state |2> is equal to the state |1>, amplification due to stimulated emission process vanishes. The rapid transition from state |1> to state |g> means that there are always more atoms in the state |2> than state |1>; as a result, the condition for optical amplification is automatically satisfied in a 4- level system.

For a 3-level system, the state |1> does not exist. Because of this, the atoms decay directly from the state |2> to the ground state |g>. As a result, the stimulated emission becomes harder, because the number of atoms in the state |2> should now exceed the number of atoms in the ground state |g>.

To obtain directional laser output based on stimulated emission, it is important to design a stable resonator so that photons emitted by spontaneous emission and aligned along the

optical axis of the resonator can initiate the amplification process. General rules for the design of a stable resonator are described in the following section. Minimum input power that initiates optical amplification is called threshold power. Designing a proper lensing mechanism for the pump beam and an ideal stable resonator design will reduce the threshold power for a laser. So, decreasing the threshold value for a laser improves it's efficiency. In our experiments we are aiming to obtain laser system with a threshold pump power as low as possible.

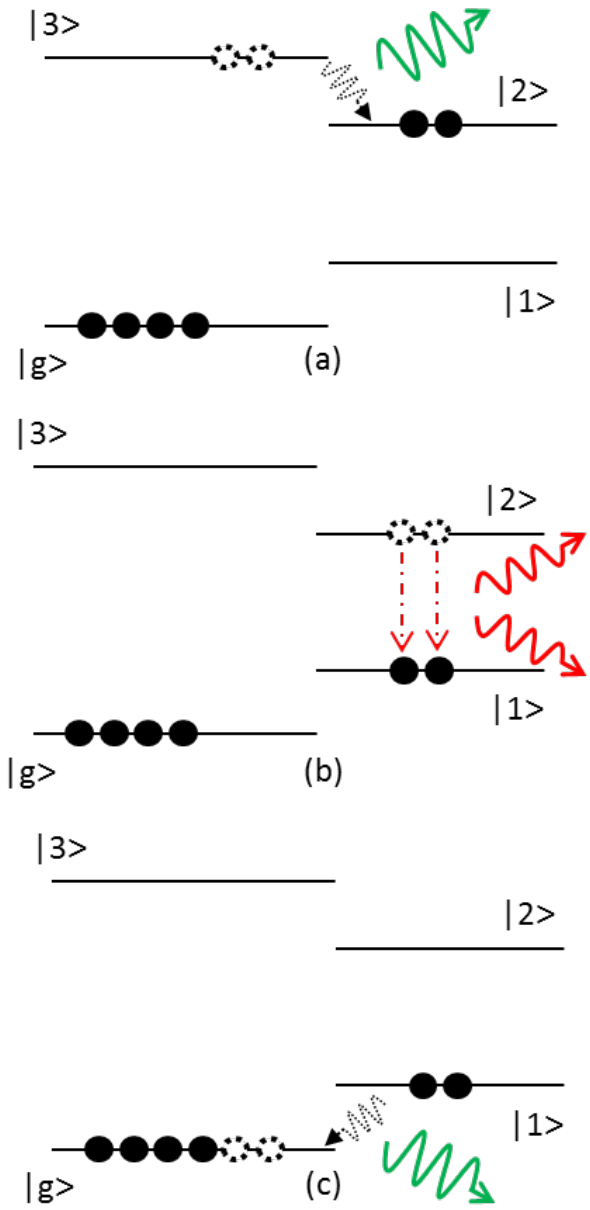

Figure 2.1.3 Spontaneous emission decays (a) from |3> to |2> (b) from |2> to |1> and (c) from |1> to |g>

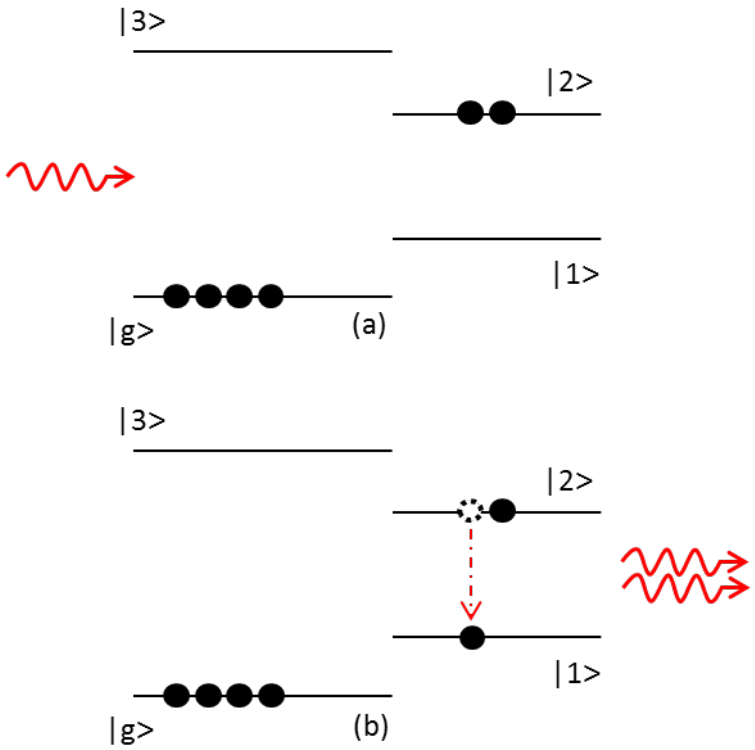

Figure 2.1.4 Stimulated emission process (a) incoming photons (b) optical amplification

2.2. Designing Laser Resonators

As mentioned before, lasers are optical oscillators. The resonator which is used for generating laser light determines the spatial mode properties and the frequency of the output. To develop a very simple view, we can say that a laser resonator is very similar to a stretched string. We need two ends (in the case of the laser, two end mirrors) that are a certain distance L apart. The wavelength of the lowest electromagnetic mode that can oscillate between these two mirrors satisfies

$$\lambda = 2L, \tag{2.2.1}$$

where λ is the wavelength. Since $\lambda\nu=c$ (where ν is the frequency and c is the speed of light), we obtain

$$\nu_1 = \frac{c}{2L}. \tag{2.2.2}$$

This is the lowest frequency that is supported for a laser resonator. It can easily be observed by drawing half of a sinusoidal wave between the end mirrors (Fig 2.2.1)

The corresponding electric field over time for this mode can be written as

$$E_1(t) = E_1 e^{i(2\pi\nu_1 t+\phi_1(t))}. \tag{2.2.3}$$

Here E_1 is the amplitude of the mode, t is the time and $\phi_1(t)$ is the phase of the mode.

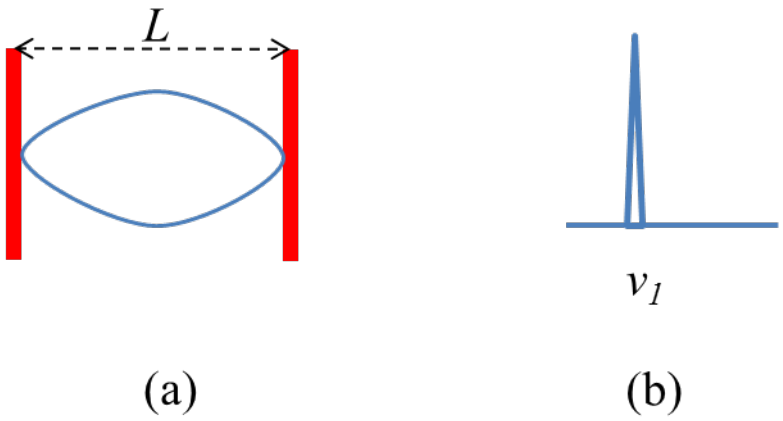

Figure 2.2.1 Lowest resonant mode (a) Sketch of the field distribution inside the cavity (b) Corresponding spectral distribution of the mode

We can also determine the conditions for a full wavelength that fits between the two mirrors (Fig 2.2.2). In this case

$$\lambda = \frac{2L}{2}, \tag{2.2.4}$$

$$\nu_2 = 2\frac{c}{2L}, \tag{2.2.5}$$

and the corresponding electric field is

$$E_2(t) = E_2 e^{i(2\pi\nu_2 t + \phi_2(t))}. \tag{2.2.6}$$

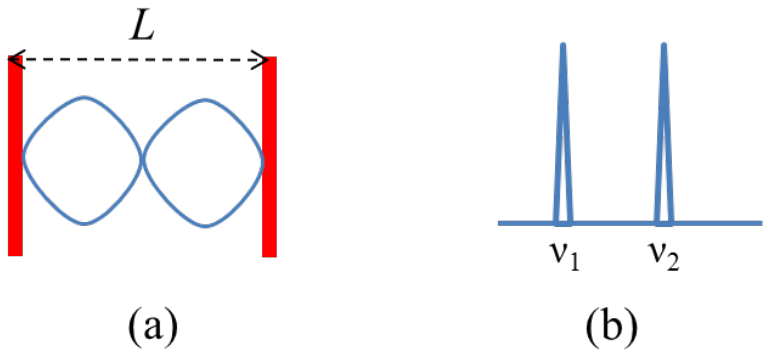

Figure 2.2.2 Second resonant mode (a) Sketch of the field distribution inside the cavity (b) Corresponding spectral distribution of the mode

Additionally, one and a half of the wavelength that fits into the cavity (Fig. 2.2.3) would be:

$$\lambda = \frac{2L}{3}, \tag{2.2.7}$$

$$\nu_3 = 3\frac{c}{2L}, \tag{2.2.8}$$

$$E_3(t) = E_3 e^{i(2\pi\nu_3 t + \phi_3(t))}. \tag{2.2.9}$$

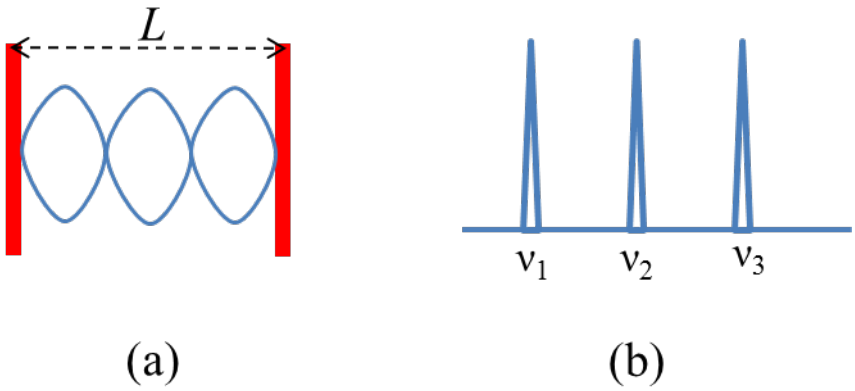

Figure 2.2.3 Third resonant mode (a) Sketch of the field distribution inside the cavity (b) Corresponding spectral distribution of the mode

If we generalize, for the q^{th} mode (Fig. 2.2.4):

$$\lambda = \frac{2L}{q}, \tag{2.2.10}$$

$$\nu_q = q\frac{c}{2L}, \tag{2.2.11}$$

$$E_q(t) = E_q e^{i(2\pi\nu_q t+\phi_q(t))}. \tag{2.2.12}$$

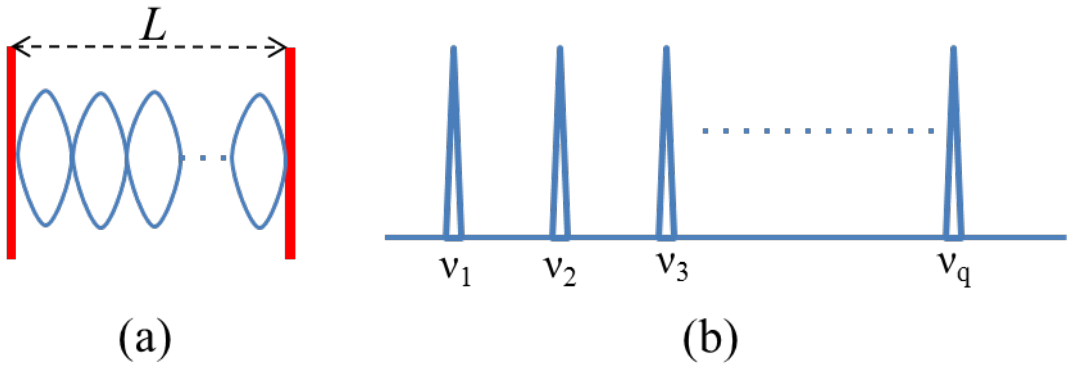

Figure 2.2.4 the qth resonant mode (a) Sketch of the field distribution inside the cavity (b) Corresponding spectral distribution of the mode

Sum of all the electric field until the q^{th} mode yields:

$$E(t) = \sum_{k=1}^{q} E_k e^{i2\pi(\nu_1+(k-1)\Delta\nu)t+i\phi_k(t)} \tag{2.2.13}$$

One can conclude that the difference between any two consecutive frequencies is constant and equal to

$$\Delta\nu = \frac{c}{2L} \tag{2.2.14}$$

This difference is called the free spectral range (FSR) of the resonator. These are the modes that this resonator can support. However, they cannot overcome the losses themselves and hence they cannot oscillate inside the cavity. To overcome the losses we include an optical amplifier in the cavity. The amplifier provides optical gain for the light with specific frequencies as mentioned in the previous section. If the amplified mode overcomes the losses, it starts to oscillate inside the cavity (Fig. 2.2.5). Some of the power that is carried in that mode can be extracted from the resonator by making one of the mirrors partially transmitting. This mirror is called the output coupler.

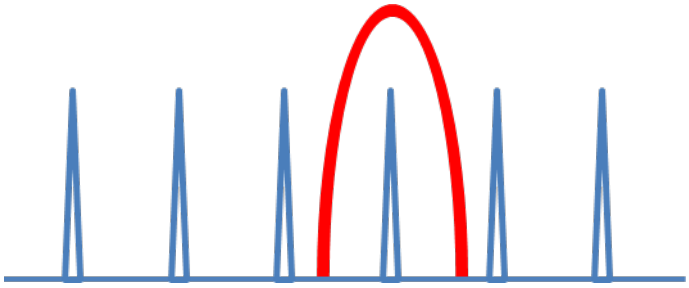

Figure 2.2.5 Resonant modes inside the cavity (blue triangles) and the gain band of the optical amplifier (red curve)

This section explained how a laser resonator works. In order to design a resonator for a stable laser operation, first we need to understand Gaussian beams and their behavior when they pass through the optical elements.

2.2.1 Gaussian Beams

From the solutions of Maxwell's equations and the spherical boundary conditions for a resonator, we know that the electric and magnetic fields of a confined laser beam have a Gaussian distribution in the transverse plane which is perpendicular to the direction of propagation. Such modes are known as Gaussian beams. These Gaussian beams are generally transverse electromagnetic (TEM) waves because the laser wavelength is much smaller than the spotsize of the beam, in which case, the axial components of the confined field are negligible. In the paraxial regime, the solution of the wave equation gives the amplitude variation of the electric field in the transverse direction as

$$u(r,z) = \exp\left[-i\left(P(z) + \frac{k}{2q(z)}r^2\right)\right]. \tag{2.2.15}$$

Above, r is the transverse radial coordinate, z is the longitudinal coordinate, and k is the wave vector. $P(z)$ describes the axial phase factor whereas $q(z)$ is known as the Gaussian q-parameter [32]. The q-parameter provides information about the radius of curvature of the equiphase surfaces $R(z)$ and the spotsize $\omega(z)$ describes the radial position where the field decays to $1/e$ of its maximum value. q(z) is given by,

$$\frac{1}{q(z)} = \frac{1}{R(z)} - i\frac{\lambda}{\pi n \omega^2(z)}, \tag{2.2.16}$$

where n is the refractive index of the medium [32]. In a homogeneous medium $R(z)$ and $\omega(z)$ can be calculated from

$$R(z) = (z - z_f)\left[1 + \left(\frac{z_0}{z - z_f}\right)^2\right] \tag{2.2.17}$$

$$\omega(z) = \omega_0\sqrt{1 + \left(\frac{z - z_f}{z_0}\right)^2} \tag{2.2.18}$$

In the above equations, z_f is the focus location; ω_0 is the beam waist (i.e. minimum spotsize) which occurs at z_f; and z_0 is the Rayleigh range which gives the distance from the focus to the position where the spotsize increases to $\sqrt{2}\omega_0$ (Fig 2.2.6) [32]. The Rayleigh range can be expressed in terms of the wavelength of the medium λ, refractive index of the medium n, and the beam waist ω_0 as

$$z_0 = \frac{n\pi\omega_0^2}{\lambda}. \tag{2.2.19}$$

This equation is valid only for a diffraction limited Gaussian beam. However, most of the laser beams are non-ideal. For this case, an M^2 factor is introduced to describe the deviation of the laser beam from the ideal diffraction-limited mode, so that:

$$z_0 = \frac{n\pi\omega_0^2}{M^2\lambda} \tag{2.2.20}$$

As it can be seen from this equation, if the M^2factor is close to or equal to unity, the laser has an ideal Gaussian beam variation. On the other hand, the laser has a larger divergence angle for the case when M^2>1 [32].

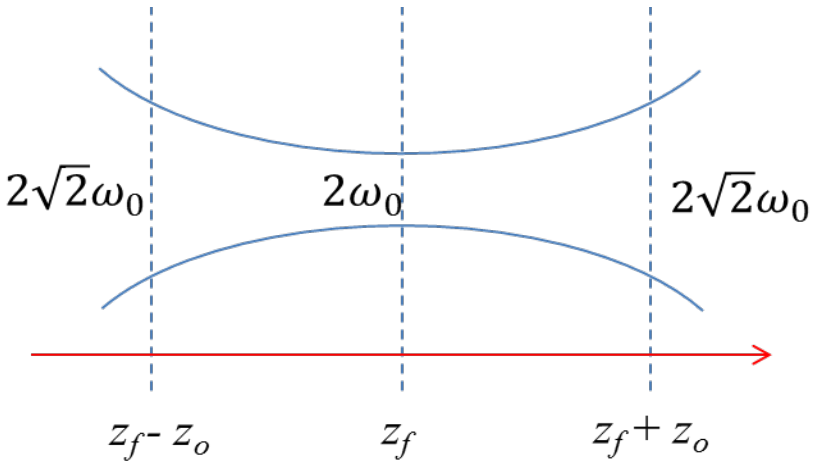

Figure 2.2.6 Sketch of a Gaussian beam near the location of the beam waist, showing the distances corresponding to one Rayleigh range.

For obtaining maximum efficiency from a laser system, the Gaussian beam inside the cavity should be arranged (i.e. the resonator should be designed) such that the beamwaist is located near the middle of the gain medium and the RMS volume of the beam should be minimized. This holds for both the pump and the laser beams. As a result, the highest power density can be obtained inside the gain medium and the maximum amount of population inversion and amplification will occur. For this condition, the calculation shows that the beamwaist inside the gain medium is equal to

$$\omega_0 = \sqrt{\frac{d\lambda}{2\sqrt{3}n\pi}} \tag{2.2.21}$$

Here d is the length of the gain medium. To see where Eq. 2.2.21 comes from, first assume the focus point z_f is located exactly in the middle of the gain medium. Then RMS of the beam waist over the length of the gain medium can be written as

$$\omega_{RMS} = \sqrt{\frac{1}{d}\int_{-d/2}^{d/2}\omega^2(z)dz} = \sqrt{\frac{1}{d}\int_{-d/2}^{d/2}(\omega_0)^2\left(1+\frac{z^2\lambda^2}{n^2\pi^2(\omega_0)^4}\right)dz}$$

Solution of the above equation will give the RMS value of the spotsize inside the whole gain medium such that:

$$\omega_{RMS} = \omega_0\sqrt{1+\frac{d^2\lambda^2}{12n^2\pi^2(\omega_0)^4}}$$

Next, to obtain maximum intensity of the power inside the gain medium, the area of the spotsize inside the gain medium should be minimized, i.e. the derivative of the $(\omega_{RMS})^2$ with respect to beamwaist should equal to zero:

$$\frac{\partial(\omega_{RMS})^2}{\partial\omega_0} = \frac{\partial\left((\omega_0)^2+\frac{d^2\lambda^2}{12n^2\pi^2(\omega_0)^2}\right)}{\partial\omega_0} = 0$$

Solution of the above derivative will give us

$$2\omega_0 - \frac{d^2\lambda^2}{6n^2\pi^2(\omega_0)^3} = 0.$$

Arranging above equation will yields the best beamwaist that maximizes the efficiency which we have written as Eq. 2.2.21

$$\omega_0 = \sqrt{\frac{d\lambda}{2\sqrt{3}n\pi}}. \tag{2.2.21}$$

In an actual operating laser, the exact locations of the pump and laser beam waists will depend on many parameters such as pump power, intracavity laser power, thermal lensing, absorption coefficient of the crystal and so on. However, Eq. 2.2.21 is a good starting point in the design of an efficient laser resonator.

When a Gaussian beam passes through an optical element, the *q*-parameter of the beam is modified. To formulate this modification we need the ray transfer matrix coefficients of the optical element.The method used in performing these calculations is described next.

2.2.2 The Ray Transfer Matrix of Optical Elements

Since a ray, by definition, is normal to the optical wavefront, understanding the ray behavior helps to trace the evolution of the optical waves (i.e. light as it passes through various optical elements). Since the laser beams propagate at a very small divergence angle, it is possible to assume that the paraxial ray approximation holds and that the angles made with the optical axis remain small.

In this approach, each ray is represented by a 2-by-1 ray vector that consists of the ray height from the optic axis *r* and the ray angle θ made with the optical axis, at any position *z* on the axis:

$$\bar{r} = \begin{bmatrix} r \\ \theta \end{bmatrix} \tag{2.2.22}$$

If we consider the optical system as a black box (Fig. 2.2.7), the input ray and output ray vectors can be written as:

$$\bar{r}_i = \begin{bmatrix} r_i \\ \theta_i \end{bmatrix} \tag{2.2.23}$$

$$\bar{r}_o = \begin{bmatrix} r_o \\ \theta_o \end{bmatrix} \tag{2.2.24}$$

and the ray transfer matrix relates to these two vectors such that:

$$\bar{r}_o = M_T \bar{r}_i \tag{2.2.25}$$

The ray matrices of some of the optical elements are summarized in Table 2.2.1 1 and their derivation may be found in standard texts on Photonics and Lasers [32]

In an optical system consisting of a series of optical elements, the output ray vector can be obtained by multiplying the ray matrices in sequence with the input ray vector. For example, consider a cascaded optical system consisting of three elements M_{T1}, M_{T2}, M_{T3}, respectively. The relation between output ray and input ray is written in the form:

$$\bar{r}_o = M_{T3} M_{T2} M_{T1} \bar{r}_i \tag{2.2.26}$$

and in more general form:

$$\bar{r}_o = \prod_{k=1}^{N} M_{T(n-k)} \bar{r}_i \tag{2.2.27}$$

where N is the number of optical elements in the system.

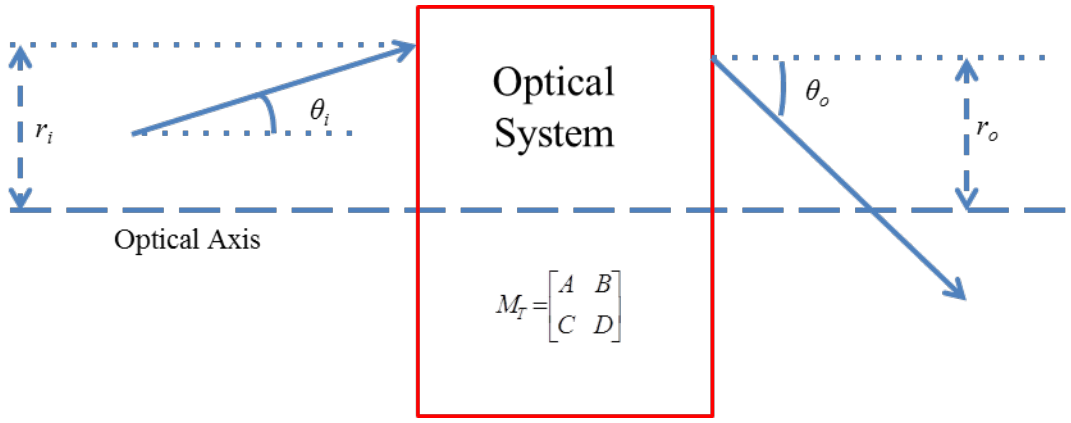

Figure 2.2.7 Representative sketch of an optical system with input and output rays

Table 2.2.1 Ray transfer matrices of some of the optical elements

Component	Ray transfer Matrix
Free Space	$M_T = \begin{bmatrix} 1 & d \\ 0 & 1 \end{bmatrix}$
Thin lens	$M_T = \begin{bmatrix} 1 & 0 \\ -\frac{1}{f} & 1 \end{bmatrix}$
Curved Mirror	$M_T = \begin{bmatrix} 1 & 0 \\ -\frac{2}{R} & 1 \end{bmatrix}$
Interface	$M_T = \begin{bmatrix} 1 & 0 \\ 0 & \frac{n_1}{n_2} \end{bmatrix}$

It can be shown that the ray transfer matrix elements can also be used to calculate the evolution of a Gaussian beam through an optical element. In particular, the q-parameter before the optical element (q_1) and after the optical element (q_2) can be related by the elements of the ray transfer matrix according to

$$q_2 = \frac{Aq_1 + B}{Cq_1 + D} \tag{2.2.28}$$

assuming

$$M_T = \begin{bmatrix} A & B \\ C & D \end{bmatrix} \tag{2.2.29}$$

2.2.3 Resonator Design

As mentioned earlier, a laser resonator has two end-mirrors. Between these two mirrors, the beam goes back and forth for an indefinite number of times. To have a stable resonator, after each round trip, the q-parameter should return back to its value during the previous roundtrip, at each point inside the cavity. This requires that

$$q_{n+1} = q_n = \frac{Aq_n + B}{Cq_n + D} \tag{2.2.30}$$

The solution of the above equation tells us that, for a stable resonator

$$Cq^2 - (A - D)q - B = 0 \tag{2.2.31}$$

which leads to:

$$\frac{1}{q} = \frac{D - A}{2B} - i\frac{\sqrt{1 - \left(\frac{A + D}{2}\right)^2}}{|B|} \tag{2.2.32}$$

Since only the negative imaginary part gives a confined Gaussian beam, the correction of absolute value and minus sign is added into Eq. 2.2.32. Hence, for a stable resonator, the inner part of the square root should be greater than zero i.e.

$$\left|\frac{A + D}{2}\right| \leq 1 \tag{2.2.33}$$

By comparing Eq. 2.2.16 and Eq. 2.2.32, one can see that the expressions for the radius of curvature R and the spotsize ω at that location are given by

$$\frac{1}{R} = \frac{D - A}{2B} \tag{2.2.34}$$

$$\frac{\lambda}{n_0 \pi \omega^2} = \frac{\sqrt{1 - \left(\frac{A + D}{2}\right)^2}}{|B|} \tag{2.2.35}$$

Once the laser resonator is designed and the losses are overcome, the system can be operated in different regimes. These regimes will be explained briefly in the next section.

2.3. Laser Operation Regimes

As mentioned in the beginning of this chapter, the lasers are generally operated in two different regimes: continuous wave regime, in which the output power is constant over time, and pulsed regime, in which the output of a laser is non-zero only over a finite duration of time. The pulsed regimes are also divided into two different regimes depending on their repetition rate and pulsewidths.

2.3.1 Continuous-Wave

In the continuous-wave regime, the output power of the laser is constant over time. Once the threshold for laser is reached for lasing operation, the maximum obtainable efficiency (η) can be determined by using the Caird's formula:

$$\eta = \eta_A \frac{\lambda_p}{\lambda_l} \frac{T}{T + L} \tag{2.3.1}$$

Here λ_p and λ_l are wavelengths of the pump and laser beam, respectively, and η_A is the pump beam absorption of the gain medium [33]. T is the transmission percentage of the

output coupler and L is the passive loss of the resonator. The value of L generally comes from the non-ideality of the optical elements used in the resonators, since they all have non-zero losses, and can be estimated from threshold pump power measurements obtained with different output couplers. According to the Findlay-Clay analysis, the threshold pump power value varies linearly with the cavity loss according to

$$P_{th} = A(T + L) \tag{2.3.2}$$

In the above equation, P_{th} is the threshold pump power, and A is the proportionality constant [34].

The comparison between the efficiencies obtained from a laser system and estimated from the Eq. 2.2.21 gives us a measure with which to evaluate the actual performance relative to the ideal performance. As the results approach each other, one may conclude that the design is approaching the ideal configuration.

If the gain medium of the laser has longer τ_f than 1/FSR ($1/\Delta\nu$) of the cavity, then small fluctuations in pump power also lead fluctuations in the output power. This phenomenon is called relaxation oscillation and the frequency of these oscillations can be estimated from:

$$w_R = \sqrt{\frac{r(T + L)\Delta\nu}{\tau_f}} \tag{2.3.3}$$

where w_R is the relaxation oscillation frequency in radian/sec, r is the ratio of the pump power to the threshold pump power and the other parameters are as defined earlier [35].

2.3.2 Q-Switching

Q-switching is one possible regime of pulsed operation for lasers. It is obtained by changing the quality factor (Q-factor) of the resonator, which determines the amount of loss present in the resonator. To obtain Q-switching operation, a variable loss is inserted into the cavity that lowers the Q-factor of the cavity. When this switch is closed, the

amount of loss in the cavity is increased and therefore the number of atoms in the upper state (state |2> in the Fig. 2.1.1) is increased because stimulated emission becomes harder. On the other hand, when this switch is opened, the loss of the cavity decreases, the transition from upper state to lower state becomes easier, and stimulated emission occurs. This on and off process occurs in a very short period of time, and creates short pulses coming from the laser. Moreover, these pulses result in very high peak powers because of the large number of atoms undergoing stimulated emission over a very short time, typically several round trips or less. The pulse durations are in the range of micro- to nano-seconds, depending on the length of the cavity. In repetitively Q-switched lasers based on a saturable absorber, the repetition rate of the pulses (f_{rep}) depends on the fluorescence lifetime of the medium (τ_f), the small-signal gain of the laser (G_o), and the modulation depth of the loss element (Q_o) according to [36, 37]:

$$f_{rep} = \frac{1}{\tau_f}\frac{G_o}{2Q_0}. \tag{2.3.4}$$

The small-signal gain varies almost linearly with the pump power and can be estimated from the efficiency equation given by:

$$P_{out} = T\frac{P_{sat}}{2}\left(\frac{G_o}{G_{th}} - 1\right). \tag{2.3.5}$$

Above, P_{out} is the output power of the laser system, and G_{th} is the fractional threshold gain needed to reach lasing which can be expressed as $G_{th} \approx 0.5$ (T+L). The saturation power P_{sat} is further given by:

$$P_{sat} = \frac{h\nu}{\sigma_e \tau_f} A \tag{2.3.6}$$

for a 4-level laser. Here, σ_e is the emission cross-section of the gain medium and A is the cross-sectional area of the laser beam inside the gain medium.

2.3.3 Mode-Locking

As mentioned previously, from a Q-switched laser, one can obtain pulsewidths in the micro- to nano-second range. Shorter pulse durations can be obtained via the mode-locking technique. Typical pulse durations in this method are in the pico- to femto-second range. In this technique, the resonator is designed such that the relative phase of all of the oscillating longitudinal electric fields ($\phi(t)$) are constant and equal to each other. If the gain of the amplifier is broad enough to support more than one mode and if these modes can overcome the loss of the resonator, then essentially all these modes oscillate inside the cavity. Since their phases are equal to each other, they will superimpose and generate ultrashort optical pulses. In this regime, spectrum broadening occurs in the laser output. This operation can be achieved by using an intracavity modulation element just like in the Q-switched case.

To see the effect of mode-coupling, one can set all the phase factors to zero in Eq. 2.2.13 and calculate the total electric field as

$$E(t) = E_0 e^{i\omega_0 t} \frac{\sin\left(\frac{M 2\pi\Delta\nu t}{2}\right)}{\sin\left(\frac{2\pi\Delta\nu t}{2}\right)} \tag{2.3.7}$$

This is assuming that the M modes are oscillating inside of the cavity and that all of them have the same amplitude E_0. Also, it is assumed that the resonant frequencies of all the modes are equally spaced. Eq. 2.3.7 tells us that the electric field has a local maximum at $t=0$. The following maxima occur at integer multiples of $t=1/\Delta\nu$, which yields that the repetition rate of the pulses is equal to the FSR of the cavity and is given by

$$f_{rep} = \Delta\nu = \frac{c}{2L}. \tag{2.3.8}$$

Furhermore, the pulsewidth (τ_p) can be roughly estimated as

$$\tau_p = \frac{1}{M\Delta\nu} \tag{2.3.9}$$

In a typical mode-locked laser, the number M is quite large. In such case, one can replace the summation in Eq. 2.2.13 with an integral

$$E(t) = \int_{-\infty}^{\infty} E_p(\omega) e^{i\omega t + i\phi(\omega)} d\omega \tag{2.3.10}$$

In the equation above $E_p(\omega)$ is the spectral amplitude distribution, ω is the angular frequency and $\phi(\omega)$ is the phase. As in the discrete case, for effective mode-locking the phase term should be constant. However, in a practical system, nonlinear and dispersive effects distort the phase over the bandwidth. This distortion can be minimized by different compensation tricks. If these unwanted effects are eliminated from the system, the laser can produce the shortest possible pulsewidth for the given spectral bandwidth. Such pulses are called transform-limited pulses. For a transform-limited pulse, the pulsewidth and the spectral bandwidth ($\Delta\lambda$) of the laser are inversely related and satisfy

$$\tau_p \Delta\lambda = K \tag{2.3.11}$$

where K is a constant, of the order of unit, known as the time-bandwidth product. The exact value of K depends on the functional shape of the generated pulses. For a sech^2 pulse profile, which is typically generated from solitary lasers, K=0.315.

Chapter 3

DEVELOPMENT of a CAVITY DESIGN SOFTWARE

The design rules for a stable laser resonator were described in the previous chapter. This condition has been well studied for some specific types of cavities. However, in a more complicated cavity, it will be very hard to find the exact combination of optical elements that produce a stable configuration. Moreover, to satisfy the conditions for efficient laser operation (given in Eq. 2.23),a more detailed calculation is necessary. To overcome these difficulties and to facilitate fast design of general stable resonators, a comprehensive software is required. In this chapter, we will first design a four mirror resonator and determine the necessary parameters by using analytic formulas. Next, a computer program will be introduced for solving the same problems. Finally, complicated non-trivial cavity design will be analyzed with the same computer program.

3.1 Four-Mirror Optical Resonators

Four-mirror cavities are often used in solid-state laser systems. This geometry consists of two flat end mirrors, two intra-cavity curved mirrors (typically with the same radius of curvature R) and, finally, a gain medium between the curved mirrors (Fig. 3.1.1).

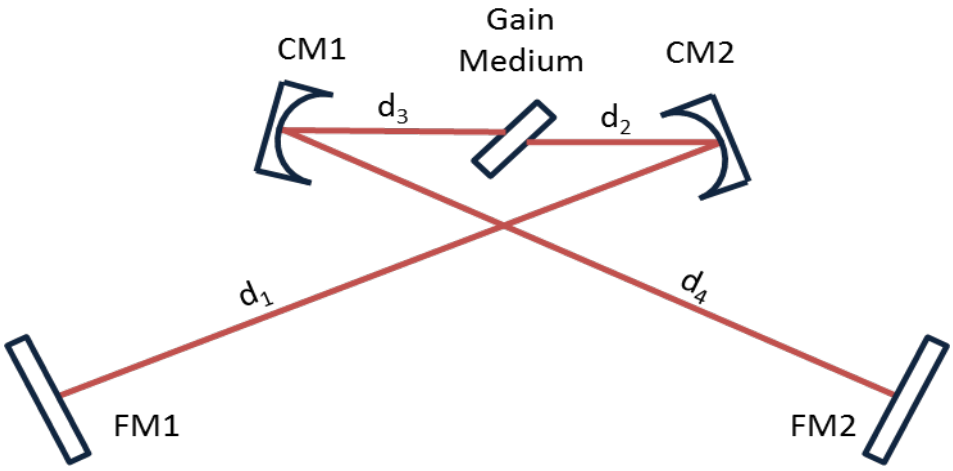

Figure 3.1.1 Typical four-mirror resonator FMx:flat end mirrors, CMx:intracavity curved mirrors dx:distance between the optical elements

Starting from the location of the first flat end mirror FM1, the round-trip ray transfer matrix for this cavity becomes

$$M_T = \begin{bmatrix} A & B \\ C & D \end{bmatrix} = \begin{bmatrix} 1 & d_1 \\ 0 & 1 \end{bmatrix} \begin{bmatrix} 1 & 0 \\ -\frac{2}{R} & 1 \end{bmatrix} \begin{bmatrix} 1 & d_2 \\ 0 & 1 \end{bmatrix} \begin{bmatrix} 1 & 0 \\ 0 & \frac{1}{n} \end{bmatrix} \begin{bmatrix} 1 & d \\ 0 & 1 \end{bmatrix} \begin{bmatrix} 1 & 0 \\ 0 & n \end{bmatrix} \begin{bmatrix} 1 & d_3 \\ 0 & 1 \end{bmatrix} \begin{bmatrix} 1 & 0 \\ -\frac{2}{R} & 1 \end{bmatrix}$$

$$\times \begin{bmatrix} 1 & 2d_4 \\ 0 & 1 \end{bmatrix} \begin{bmatrix} 1 & 0 \\ -\frac{2}{R} & 1 \end{bmatrix} \begin{bmatrix} 1 & d_3 \\ 0 & 1 \end{bmatrix} \begin{bmatrix} 1 & 0 \\ 0 & \frac{1}{n} \end{bmatrix} \begin{bmatrix} 1 & d \\ 0 & 1 \end{bmatrix} \begin{bmatrix} 1 & 0 \\ 0 & n \end{bmatrix} \begin{bmatrix} 1 & d_2 \\ 0 & 1 \end{bmatrix} \begin{bmatrix} 1 & 0 \\ -\frac{2}{R} & 1 \end{bmatrix} \begin{bmatrix} 1 & d_1 \\ 0 & 1 \end{bmatrix} \quad (3.1.1)$$

where d is the length of the gain medium and n is its refractive index. The cavity will be stable when Eq. 2.2.33 satisfies. If the cavity is stable then, the Rayleigh range on the mirror FM1 is given by

$$z_0 = \frac{|B|}{\sqrt{1-\left(\frac{A+D}{2}\right)^2}} \quad (3.1.2)$$

Then, the beamwaist inside the gain medium can be computed by tracing the Gaussian beam passing through the optical elements.

Since the optical elements are symmetrically positioned with respect to the gain medium, one can conclude that the symmetric distances should be equal to obtain a focus in the middle of the gain medium i.e. $d_1 = d_4$ and $d_2 = d_3$. Next, these distances should be arranged such that the beamwaist inside the gain medium is almost equal to the assumption in Eq. 2.2.21.

As an illustration, consider a Tm:YAG laser resonator operating at 2 μm . The crystal is 2 mm long with a refractive index of 1.8. Assume that the radius of curvature of each curved mirror is 5 cm. According to the assumption given by (Eq. 2.2.21), the optimum beamwaist inside the crystal is 14.3 μm. After some iterations, the distances $d_1 = d_4$=37 cm and $d_2 = d_3$=2.62 cm give this result for the beamwaist inside the gain medium.

3.2 Cavity Design Program

Analysis of the 4-mirror resonator is simple and well-studied so far, because these types of cavities are often used in solid-state laser systems. Moreover, symmetrical positioning simplifies the computation. However, for more complicated cases, such as curved mirrors which are not identical or more than four elements (not necessarily symmetric) used in the system, the ray transfer matrix will become more complex and the determination of the distances for the optimum beamwaist will become extremely difficult. Hence, a computer program is required to solve such problems in an easier fashion. Based on this need, we have developed a software by the name of “ersen’s abcd”.

This program essentially takes the elements and plots the spotsize inside the entire cavity. Moreover it can provide the slider bars to adjust the distances between elements. The Matlab code for this program and its simple application is described in Appendix A.

Using this program, the result for the example in Fig. 3.1.1.can be seen in Fig. 3.2.1.

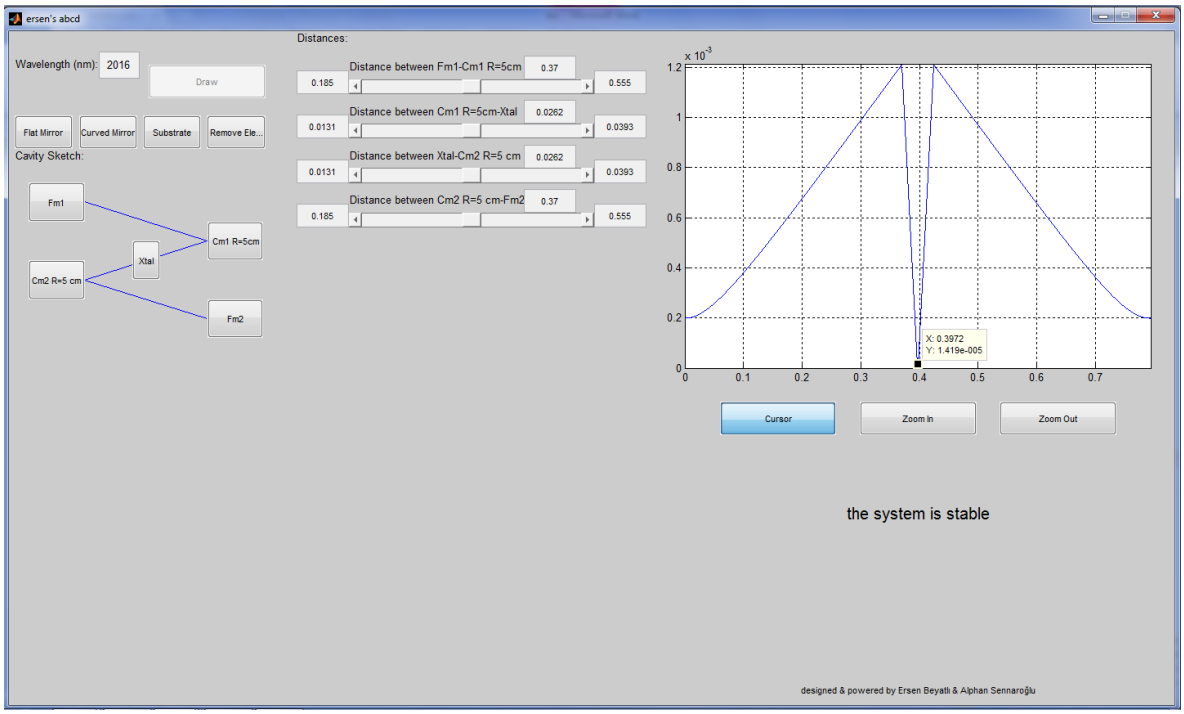

Figure 3.2.1 Solution of a typical four-mirror Tm:YAG cavity in the ersen's abcd program.

The results show that for the optimum cavity, the distances should be 37 and 2.62 cm as found from the matrix calculation. For these distances, the beamwaist inside the crystal is 14.2 µm.

3.3 A Non-Ordinary Cavity Design

A resonator could have more than one curved mirror pair for different purposes. For this case, the ray transfer matrix will be more complex. Hence, designing such cavities in an optimum way, in other words, determining the distances that give a desired spotsize, becomes harder.

As an example, consider a Tm:YAG (refractive index=1.8 and length= 2 mm) laser resonator that can provide 2 µm output. The laser will operate in the pulsed regime with the

help of a transparent saturable absorber (SESAM/SBR). Inserting a BBO crystal (refractive index=1.55 and length=3 mm) into the cavity, 1 μm laser output can be obtained by second harmonic generation. So, for this configuration, three focus locations are needed inside the cavity; i.e., the first location inside the crystal, the second location inside the saturable absorber and the last one inside the BBO crystal. Optimum beamwaists for the Tm:YAG and BBO crystal are 14.3 and 18.9 μm respectively. Fig. 3.3.1 illustrates a simple scheme of the cavity.

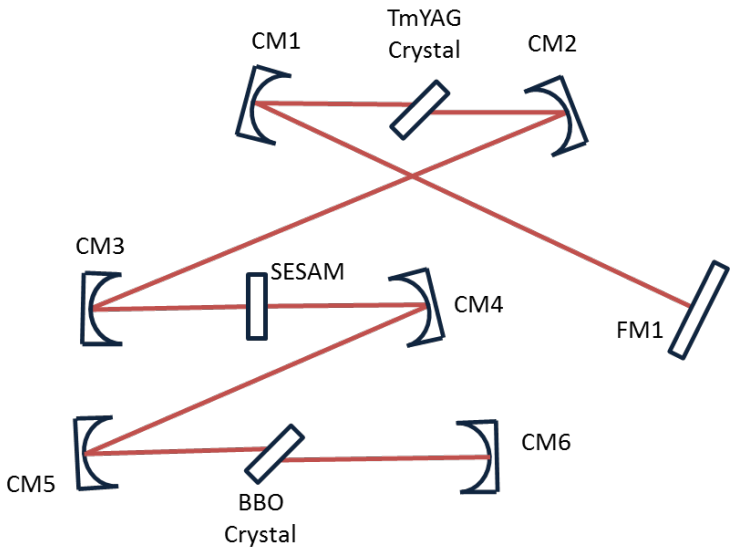

Figure 3.3.1 Sketch of the pulsed TmYAG laser cavity with an intracavity BBO crystal

In this system, the curved mirrors are not identical as before. The radius of curvature of CM1, CM2, CM5, and CM6's are 5 cm, whereas those of CM3, CM4 are 10 cm. One can assume that, since we are using SESAM in the system, it can be considered as an empty focus point because of having a very small length.

After drawing the cavity inside the program, the system is unstable with the initial distances (as expected). However, just by changing the distances with the slider-bars, the cavity becomes stable. Moreover, an optimum configuration of the system can be achieved

by carefully changing the slider-bars. As a result, the distances for the optimum design configuration become as follows (Fig. 3.3.2):

FM1-CM1	=37 cm
CM1- TmYAG Crystal	=2.62 cm
TmYAG Crystal - CM2	=2.62 cm
CM2-CM3	=19.2 cm
CM3-CM4	=10.15 cm
CM4-CM5	=5.1 cm
CM5-BBO Crystal	=2.57 cm
BBO Crystal-CM6	=4.98 cm

These distances yield the beamwaists of 15.7 μm for the TmYAG crystal and 19.2 μm for the BBO crystal. Moreover, the spotsize on the saturable absorber is 47 μm, which is small enough to cause saturation and enable pulsed operation.

In conclusion, with the help of this program, a sophisticated laser resonator can be designed and optimized to determine the component distances that produce a desired set of spot sizes.

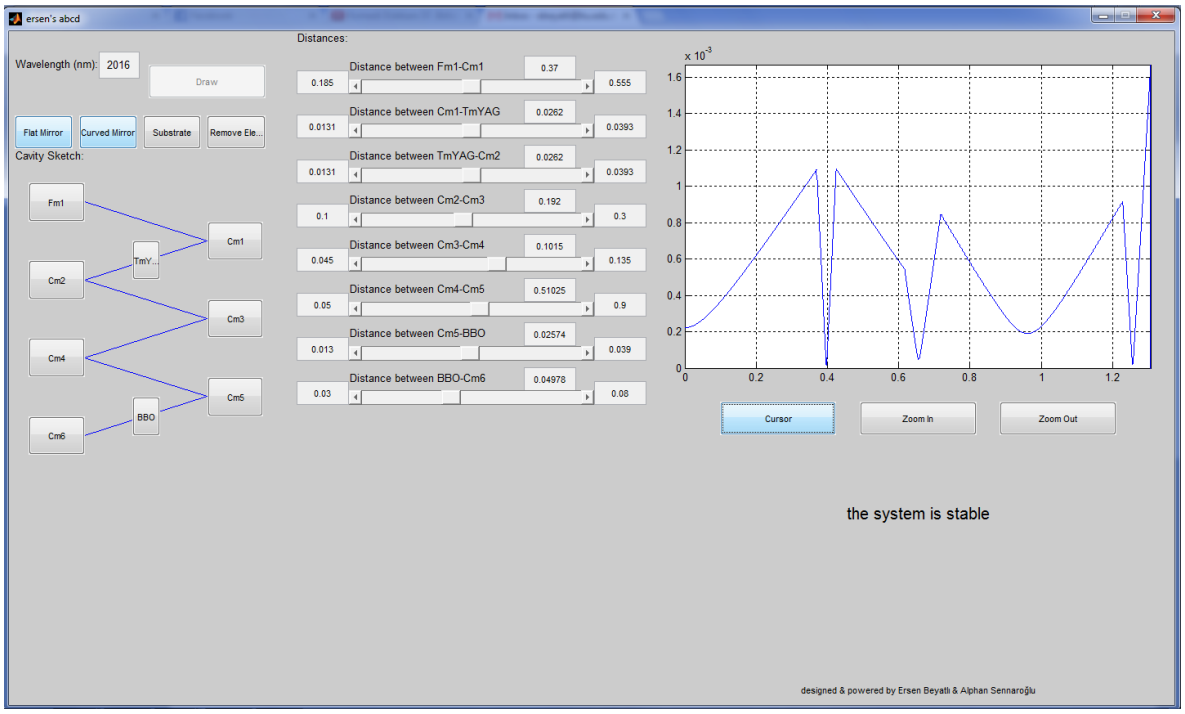

Figure 3.3.2 Solution of the pulsed TmYAG laser system with an intracavity BBO crystal by using "ersen's abcd" program.

Chapter 4

LOW-THRESHOLD CONTINUOUS WAVE OPERATION of Tm:YAG and Tm:LuAG LASERS

In this chapter, we report a low-threshold continuous-wave Tm:YAG and Tm:LuAG laser that can be excited near 785 nm with low-cost, single-mode AlGaAs laser diodes. Low-threshold operation was achieved by using a tightly focused, astigmatically compensated x-cavity containing a 2-mm-thick Tm:YAG and 3-mm-thick Tm:LuAG crystals with 5% Tm^{3+} concentration. Two linearly polarized single-mode diodes were polarization coupled to end pump the resonators. With a 6% output coupler, as high as 32 mW of output power can be obtained at 2016 nm with 184 mW of incident pump power from the Tm:YAG laser. The outputs could be further tuned by 100 nm in the 2-μm band. Slope efficiency measurements indicated that cross-relaxation was very effective at this doping level. With a 2% output coupler, laser operation can be obtained with as low as 30 mW of pump power. In the first section of the chapter, we will briefly introduce the Tm^{3+} lasers. Then, we will give the experimental details. In the third section, we will present the results and compare with the theoretical predictions.

4.1 Introduction to Tm^{3+} Lasers

Lasers operating near the wavelength of 2 microns are useful for medical applications because of the strong absorption by water in this wavelength range [7, 38-40]. Also, since the 2 μm wavelength is eyesafe (no transmission is possible up to the retina), lasers operating at this wavelength are of interest for remote sensing and laser radar[41, 42].

Moreover, for pumping other laser systems and Raman applications, the 2 μm band is also one of the desirable wavelength regimes [43-45].

Some of the most commonly used 2 μm laser sources are based on the Tm^{3+} ion-doped lasers. Depending on the host crystal used, one of the excitation wavelengths is around 800 nm and the emission wavelength varies between 1.8 and 2.2 μm (Fig. 4.1.1) [10-20].

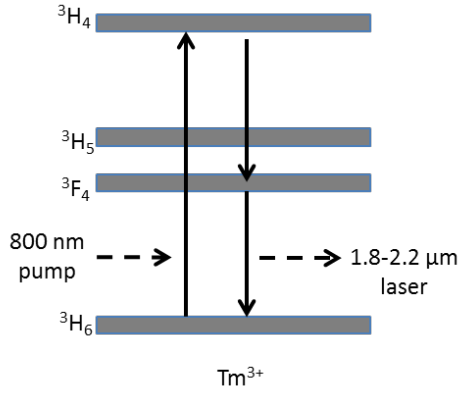

Figure 4.1.1 Energy Band Diagram of Tm3+ ions

In the 2-μm operation of Tm lasers, the ions behave as a 3-level system (see Fig. 4.1.1). Hence the gain of these systems is relatively low. On the other hand, the photons produced in the fast decay from state |3> to state |2> can excite the ions in the |g> state to the state |2>. So, effectively two photons emitting at 2 μm are generated from one absorbed photon. This process is called cross-relaxation (Fig. 4.1.2.). As a result of cross-relaxation, the efficiency of the Tm^{3+} laser systems will become twice the quantum-limit. The effect of cross-relaxation improves if the ions are close to each other inside the crystal. This advantage makes the Tm^{3+} laser systems more desirable for 2 μm operation [46].

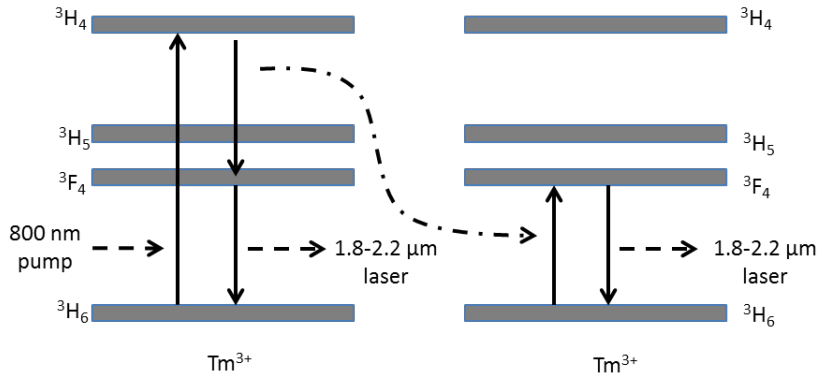

Figure 4.1.2 Cross-relaxation process in Tm3+ lasers

At first, these systems were pumped by the flashlamps. However, since the flashlamps provide light in a very broad spectral region, the gain of the system is extremely low [47-49]. Later, Ti:Sapphire laser systems were used for excitation of these systems [10, 15, 16]. Their tunability range of 800 nm makes them one of the best choices for Tm^{3+} lasers. But, pumping with another laser system increases the cost and complexity of the laser system. These disadvantages limit the use of Ti:Sapphire option except in places such as research centers and laboratories. AlGaAs laser diodes developed in the last two decades have become one of the best alternatives to Ti:Sapphire lasers. Their bandgap can be arranged for the desired wavelength around 800 nm so that the best overlap is obtained between the Tm^{3+} absorption band and the diode wavelength [22-26]. The only disadvantage of these systems is that their beam quality is very low i.e. M^2 values are much greater than 1 [26]. Hence, the gain of the systems is reduced. One of the best pumping alternatives for these systems is pumping with low-cost, single-mode laser diodes by utilizing low-threshold resonator designs. In this method, superior electrical-to-optical conversion efficiency can be obtained and the overall cost of the system can be considerably reduced.

In this study, we report low-threshold, continuous-wave (cw) operation of Tm:YAG and Tm:LuAG lasers excited with low-cost, single-mode 100-mWAlGaAs diode lasers

operating near 785 nm. In principle, other thulium-doped media could also be used to demonstrate such low-threshold operations. In this study, the Tm:YAG and Tm:LuAG gain media were chosen since their absorption bands were close to the room-temperature operating wavelength of our diode pump lasers.

4.2 Experimental Setup

In order to attain low-threshold laser operation, we used a 4-mirror x-cavity with a tight focusing geometry as shown in Figure 4.2.1. Two linearly polarized, single-mode diode pump lasers (D1 and D2, Blue Sky Research), each capable of producing up to 100 mW at the driving current of 125 mA, were used to end pump the crystals through the input curved mirror (M1). The output wavelength of the diode lasers could be tuned from 775 nm to 795 nm with a thermoelectric cooler and temperature controller which matches with Tm:YAG and Tm:LuAG absorption bands (Fig. 4.2.2). A cylindrical micro lens was used to obtain a circular beam profile from each diode laser. Each pump beam was further collimated with an anti-reflection coated aspheric lens that had a focal length of 4.5 mm. The direction of polarization of one diode was rotated by 90^{o} and a polarizing beam splitter (PBS) was used to combine the two pump beams. An AR-coated input lens (L3) with a focal length of 5 cm was used to focus the pump beams inside the gain crystal.

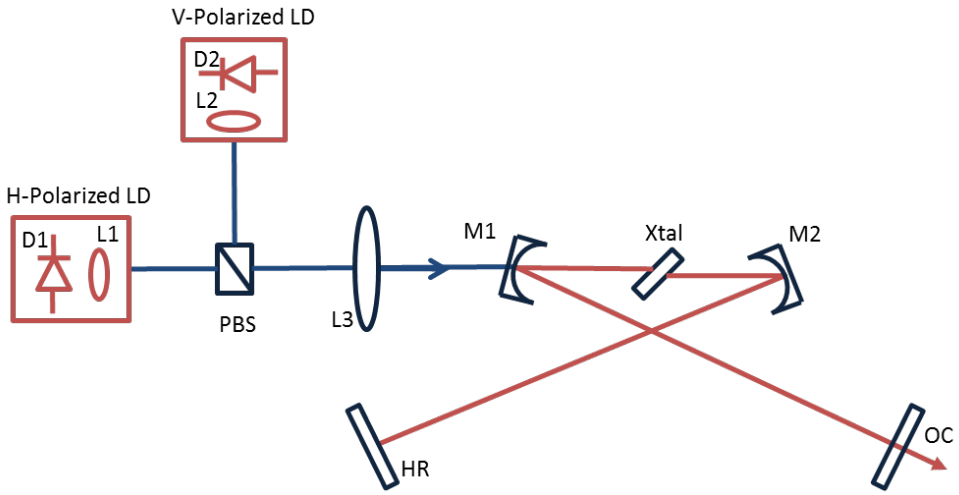

Figure 4.2.1 Experimental setup of the low-threshold Tm:YAG laser pumped with two polarization coupled single-mode AlGaAs laser diodes.

In the initial stage of the experiments, the gain medium was removed and the knife-edge method was employed to determine the parameters of the pump beams. Figure 4.2.3 shows the measured variation of the spotsize function from each diode as a function of position around the focal point. As can be seen from Fig. 4.2.3, the collimating lens of each diode was carefully adjusted to bring the waist locations of the two beams to approximately the same position. Least square fitting was further performed between the measured data and the theoretically expected spotsize function $w(z)$ which varies with axial position z

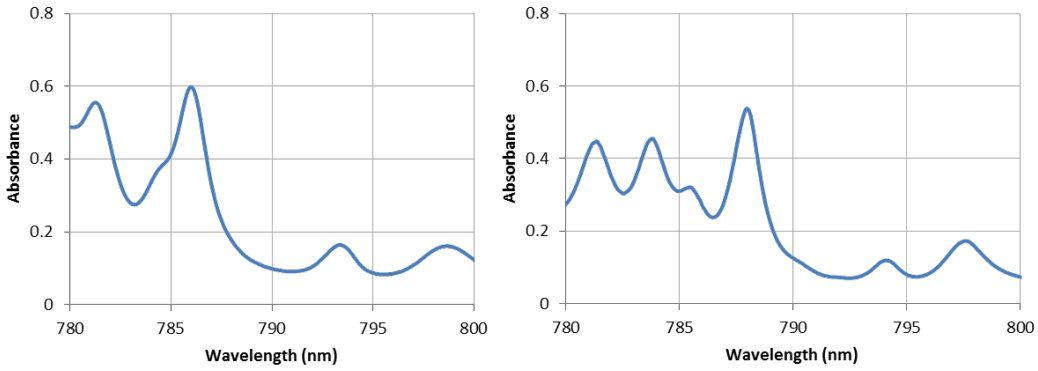

Figure 4.2.2 Absorption bands of the (a) Tm:YAG (b) Tm.LuAG crystals

according to Eq. 2.2.20. By taking λ as 785nm, M^2 and w_0 were determined to be 1.05 and 11.55μm for the horizontally-polarized beam and 1.38 and 15.85μm for the vertically-polarized beam. This further shows that the pump beams from the two diodes were nearly diffraction limited. The theoretical value of the pump beam waist that gives confocal focusing (Eq. 2.2.21) comes to about 13 μm in the crystals, suggesting that the obtained beam waists are close to the desired optimum value.

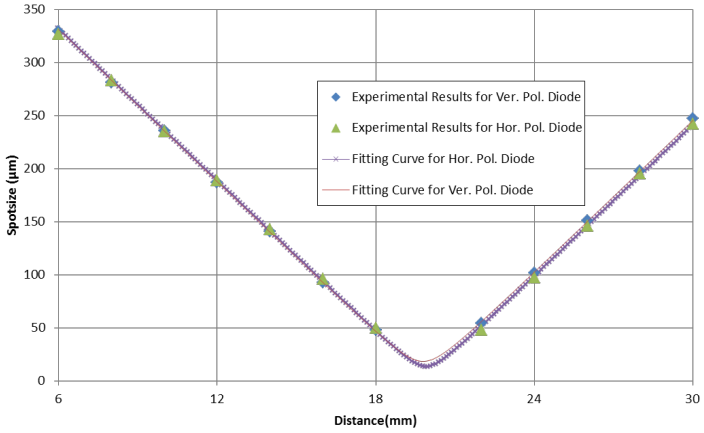

Figure 4.2.3 Measured and best-fit variation of the spotsize function as a function of the axial position around the focus location for each pump diode.

The laser resonator consisted of two identical intra-cavity input curved mirrors (M1,M2, with R=50 mm), a highly reflecting end mirror (HR), and a flat output coupler (OC). The lengths of the high reflector and output coupler arms were both set to 37 cm. The gain media, which was a 2-mm-long uncoated Tm:YAG and 3-mm-long uncoated Tm:LuAG crystal with 5% Tm^{3+} concentration, was positioned at Brewster incidence between M3 and M4. The calculated total pump absorption at 785.8 nm was 79.5 % for the Tm:YAG crystal and was 75% for the Tm:LuAG crystal (at 787.5 nm). The Fresnel reflection loss of the horizontally polarized pump beam was negligible. On the other hand, the estimated reflection loss of the vertically polarized pump beam was around 28%. By using the software we developed, the laser beam waists inside the gain media were estimated to be about 14 μm. In the experiments, power efficiency curves were measured with a 2% and a 6% output coupler (6% one was used only in the Tm:YAG system because the gain was not enough for laser operation in Tm:LuAG for output coupling above 2%). In order to tune the output wavelength of the laser, a 2.5-mm-thick quartz birefringent tuning plate (BTP) was added to the cavity on the high reflector arm and a 2% output coupler was used.

4.3 Results and Discussions

Horizontally polarized diode laser (H-polarized LD) was used to obtain lasing and the vertically polarized diode laser (V-polarized LD) was later added for power scaling. By using the tightly focused pump and resonator geometries described in the previous section, lasing could be obtained with as low as 32 mW of incident pump power at 785.8 nm for the Tm:YAG laser, when the transmission of the output coupler was 2%. Figure 4.3.1(a) shows the power efficiency curve taken with the 2% output coupler. Note that the slope efficiency of the laser was 22% when pumped with the horizontally polarized laser diode and decreased to 17% at higher pumping powers when the vertically polarized laser diode

was turned on. As noted earlier, the decrease in the slope efficiency arises because of the additional 28% reflection loss of the vertically polarized diode from the first Brewster surface of the Tm:YAG crystal. With a total input power of 187 mW, as high as 30 mW of output power was obtained from the Tm:YAG laser with the 2% output coupler. The output wavelength of the free-running resonator was at 2016 nm. Figure 4.3.1(b) further shows the power efficiency curves taken with the 6% output coupler. In this case, the slope efficiency decreased from 36% (for pumping with the horizontally polarized laser diode) to 25% (pumping with the vertically polarized laser diode). The threshold incident power for lasing was 63.7 mW in the case of the 6% output coupler and a total of 32 mW was obtained with 184 mW of incident pump power. Next, we replaced the gain medium with the Tm:LuAG crystal. In this case, we tune the wavelength of the diodes to 787.5 nm with the temperature controller to get maximum absorption. Figure 4.3.1 (c) shows the power efficiency curves for the Tm:LuAG laser taken with 2% output coupler. In this system, with 179 mW input power, as high as 22 mW of output power was obtained at 2026 nm. Moreover, the slope efficiencies decreased from 19% (for pumping with the horizontally polarized laser diode) to 13% (pumping with the vertically polarized laser diode). The gain for this situation is relatively low with respect to Tm:YAG systems possibly due to the lower pump absorption of our Tm:LuAG crystal. The estimated threshold value in Tm:LuAG is 30 mW. The reason for lower threshold value is that the ratio of the Tm^{3+} ions in the $^3F_4$ level at the lasing threshold to the total number of Tm^{3+} ions was estimated to be around 0.06 for Tm:LuAG crystal and 0.08 for Tm:YAG crystal [50]. It is important to note that, the threshold data were obtained via slope efficiency curve fitting, not directly from the threshold measurement, because, the diode wavelengths cannot be controlled by temperature controllers at low power levels.

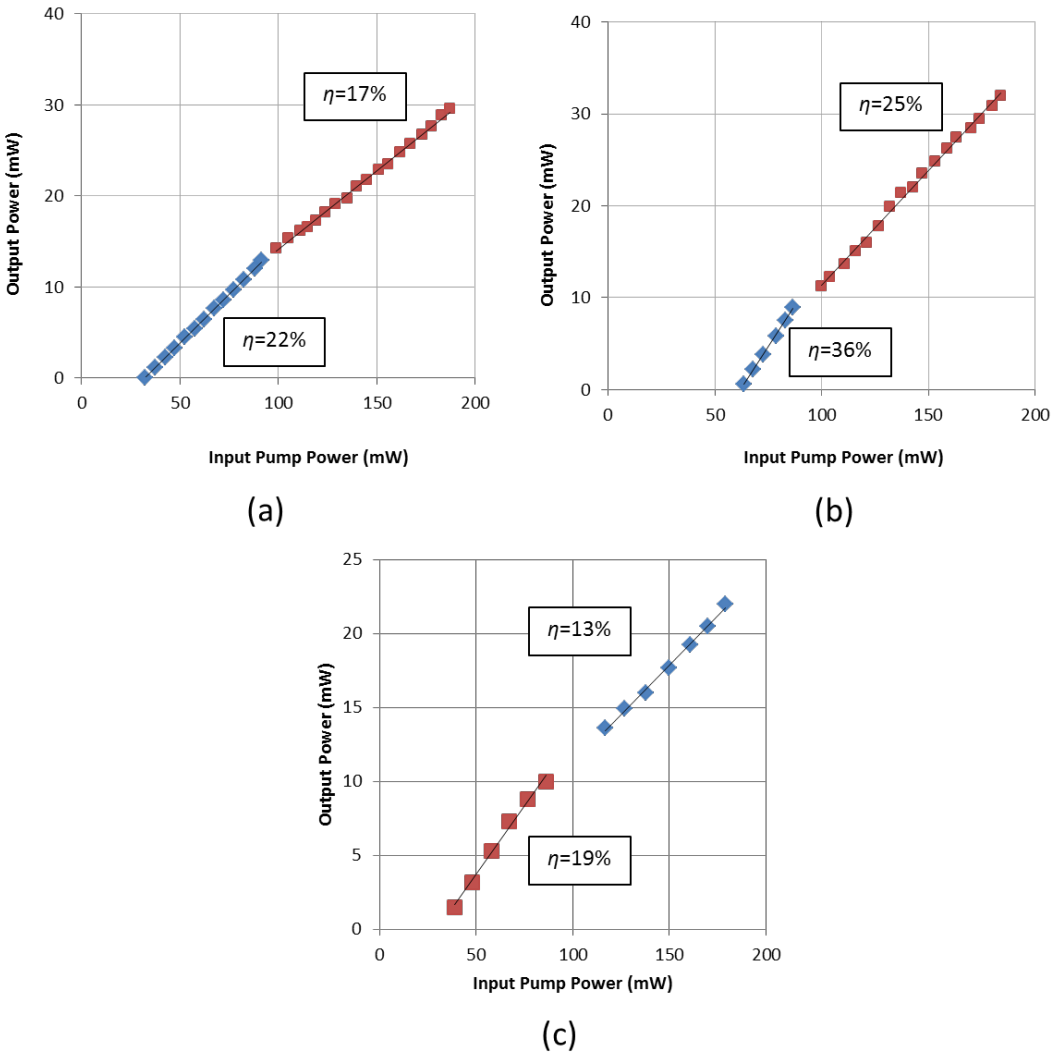

Figure 4.3.1 Measured variation of the output power as a function of the incident power for the (a) 2% output coupler for the Tm:YAG laser and (b) 6% output coupler for the Tm:YAG laser (c) 2% output coupler for the Tm:LuAG laser.

Figure 4.3.2 shows the measured variation of the incident threshold pump power as a function of the output coupler transmission for the Tm:YAG laser system. Here, in addition to the 2% and 6% output couplers, the threshold pump power was also measured with a highly reflecting output coupler that had a reflection of 99.9%. The measured threshold

pump power was 25 mW in the limit of vanishing output coupling. From Findlay-Clay analysis (Eq. 2.3.2), the round-trip cavity loss was estimated to be 3.3 %. The estimated total absorption (η_a) of the Tm:YAG crystal (the effective length at Brewster incidence was 2.3 mm) at the pump wavelength of 785.8 nm was 79.5%. Hence, from Caird-analysis (Eq. 2.3.1), the expected value for η was estimated to be 12% in the case of the 2% output coupler. The fact that the measured slope efficiency (22%) far exceeds the estimated value, is a clear indication that cross-relaxation which facilitates the 2-for-1 process is very effective at this doping level in the Tm:YAG crystal. Since the cavity-loss was possibly due to the optical elements we used, we can assume that the Tm:LuAG system has the same loss level. Therefore, the estimated maximum efficiency (η) was 11% ($\eta_{a=}$ 75% at 787.5 nm for Brewster distance), where we measure 19%. This also indicates high cross-relaxation effect in Tm:LuAG.

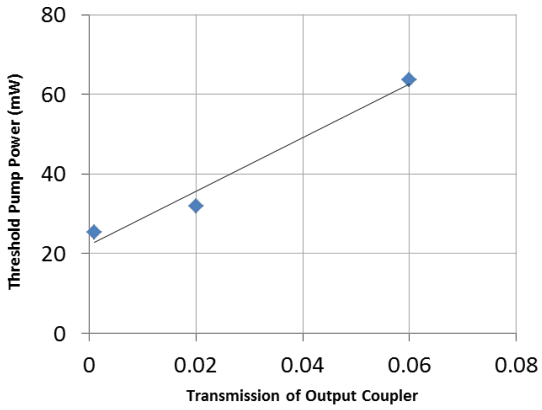

Figure 4.3.2 Measured and best-fit variation of the incident threshold pump power as a function of the output coupler transmission for the Tm:YAG laser.

Our measurements also indicate that the slope efficiencies of the lasers would be even higher if the spectral overlap of the pump diodes and the absorption band could be further improved. Figure 4.3.3 shows the measured spectra of the pump diodes at the diode temperature that gives the highest measured slope efficiencies and the absorption band of

the crystals at normal incidence. The maximum background-corrected absorbance A_{max} ($A=Log(T)$ where T=crystal transmission) was measured to be 0.598 and 0.529, corresponding to a pump absorption of 74.8% and 70% for Tm:YAG and Tm:LuAG crystals, respectively, at normal incidence. Note that the pump spectrum has a shoulder on one side, leading to a reduction in the overall absorption. We can estimate the effective absorbance A_{eff} of the crystal from the equation

$$A_{eff} = \frac{\int_{\lambda_1}^{\lambda_2} A(\lambda) g_D(\lambda) d\lambda}{\int_{\lambda_1}^{\lambda_2} g_D(\lambda) d\lambda} \tag{4.3.1}$$

where $g_D(\lambda)$ is the measured spectral intensity distribution of the pump diode. Here, the limits λ_1 and λ_2 of integration were taken to be 783 and 789 nm for Tm:YAG and 785 and 791 for Tm:LuAG, respectively. From Eq. 4.3.1, the effective absorbance for Tm:YAG came to 0.539, (corresponding to a total absorption of 71.1%). On the other hand this value increases to 0.456, (65% of total absorption). These results suggest that by using a diode which has a sharper spectrum that coincides better with the maximum of the absorption bands, the slope efficiencies can be further improved to approximately 22%x(74.8/71.1)=23% and 19%x(70/65)=20.5%. For the 2% output coupler, the theoretical limit of the slope efficiencies would be 24% and 22% if the cross-relaxation efficiencies were 100%.

Finally, by using a quartz birefringent tuning plate in the high reflector arm of the resonator, the cavities could be tuned continuously from 1935 to 2035 nm for the Tm:YAG system and from 1945 to 2045 nm for the Tm:LuAG system. Figure 4.3.4 shows the measured variation of the power as a function of the output wavelength at the incident pump power of 187 mW for the 2% output coupler. The tuning data obtained in our experiments are in agreement with what was previously reported in the literature [10].

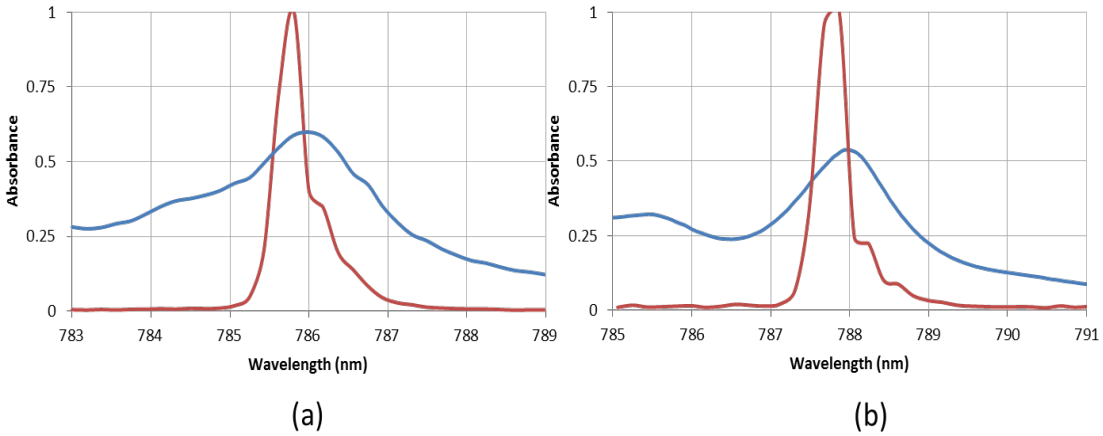

Figure 4.3.3 Measured variation of the pump diode spectrum in arbitrary units (red line) and the absorbance of the 5% (a) Tm:YAG (b) Tm:LuAG crystals (blue lines).

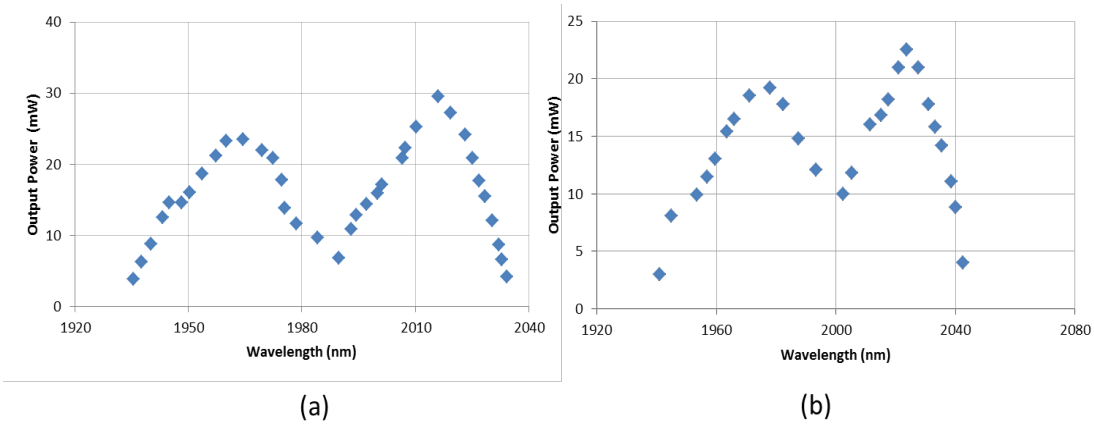

Figure 4.3.4 The tuning curve of the (a) Tm:YAG (b) Tm:LuAG laser measured with the 2% output coupler.

4.4 Conclusions

In conclusion, we have demonstrated low-threshold continuous-wave Tm:YAG and Tm:LuAG lasers that can be excited near 785 nm by using low-cost, single-mode AlGaAs

laser diodes. Low-threshold operation was achieved with a tightly focused, astigmatically compensated x-cavity. The incident threshold pump powers were around 30 mW in the case of the 2% output coupler. To our knowledge, these are among the lowest lasing thresholds reported to date for continuous-wave thulium-doped lasers operated at room temperature [11, 51]. By using the 6% output coupler, as high as 32 mW of output power could be obtained from the Tm:YAG laser at 2016 nm with 184 mW of incident pump power. The laser outputs could be further tuned by 100 nm around 2 μm. In the case of the 2% output couplers, the measured slope efficiencies (22% and 19%) were far higher than the expected slope efficiencies (12% and 11%), clearly indicating that cross-relaxation efficiency was quite high. We further estimated that by using diode pumps with sharper output spectrum, the slope efficiency could be further increased to about 23% and 20%. Low-threshold, low-cost 2 μm lasers of the type described in this work should find important applications in medicine, atmospheric communication, and spectroscopy.

Chapter 5

PULSED OPERATION of Tm:YAG & Tm:LuAG LASERS

In the near future, we believe that low-threshold continuous-wave Tm:YAG and Tm:LuAG lasers will become one of the indispensable sources for 2 μm applications such as urological cancer treatment, coherent LIDAR, remote sensing and so on. Their compact design, efficient cross-relaxation process and low-cost properties make them attractive for these applications. However, the output power they could provide (>100 mW) will possibly limit the integration of these lasers into some of the systems, because the desired powers for these systems are in the Watt levels [7, 41, 42, 52]. On the other hand, there is a possibility that these systems can be operated in the pulsed regime by inserting a saturable absorber into the resonator. With this technique, although the average powers will be low with respect to the continuous wave regime, the peak powers will reach the Watt levels over the duration of the pulse.

Q-switched mode-locking is one possible regime of pulsed operation of lasers. In this regime, the mode-locked pulse train appears under the envelope of a Q-switched pulse. Typically, the temporal separation between the mode-locked pulses is equal to the cavity round trip time, which is of the order of nanoseconds, whereas the duration of the Q-switched pulse is in the range of tens of nanoseconds to microseconds.Hence, the amplitude of each mode-locked pulse is not constant. Unlike the mode-locking case, a little broadening can be observed in the carrier frequency of the output while monitoring with a radio frequency spectrum analyzer. This represents the Q-switching tendency of the laser. Intuitively speaking, this mode of operation can be considered as a transition regime from pure Q-switching to pure continuous-wave mode-locking. This is because, in the Q-switched mode-locking configuration, if we decrease the pump power there is a chance to

observe pure Q-switched operation of the laser, whereas we can obtain pure mode-locked pulses by increasing pump powers.

In this study, we incorporate a transmissive saturable absorber into the Tm^{3+} laser resonator and obtain Q-switched mode-locked pulses near 2 μm. The obtained laser pulses have Watt-level peak powers which are more advantageous for 2 μm applications based on nonlinear interactions such as pumping of optical parametric oscillators.

In this chapter, we first describe the experimental setup of the Q-switched mode-locked lasers. Next, we present the results. We end the chapter with a general discussion of the results.

5.1 Experimental Setup

Figure 5.1.1 shows of a schematic of the Tm^{3+} doped laser cavities. Two linearly polarized ~785 nm AlGaAs single-mode diodes (D1-D2) with diffraction limited beam profiles were used as the pump source (VPSL-785-90-5-A, Blue Sky Research, the same diodes we used in the low-threshold Tm:YAG and Tm:LuAG experiments). Although these diodes were designed for 100 mW of output power at a driving current 125 mA, they can provide up to 140 mW at a driving current 160 mA. It should be noted here that, using these diodes at this power level reduces the operational lifetime of the diodes. In front of the diodes, cylindrical microlenses were used to obtain a circular beam profile. The diodes are mounted on the diode holders with thermoelectric cooler and temperature controller to adjust the output of the diode wavelengths. 4.5 mm focal length lenses (L1-L2) were used to collimate the output beams. A polarizing beam splitter (PBS) cube was used to combine the diodes and a 5 cm lens (L3) focused the pump beams into the crystals.

An astigmatically compensated, x-folded laser cavity was used in the continuous wave experiments (solid lines in Fig. 5.1.1). The resonator had two curved pump mirrors (M1

and M2, R=5 cm) and a highly reflecting mirror (HR), each with high reflectivity extending from 1.8 to 2.2 μm and >99.9% transmission at the pump wavelength (~785 nm). Different from the previous work described in Chapter 4, the high reflector was replaced with a better quality one to reduce the loss of the cavity (3.3%). Moreover, we used a 2% output coupler (OC) to increase the intracavity intensity. The symmetric arm lengths, each of 37 cm gave a laser mode size of ~15 μm inside the crystal. The gain media were 2-mm-long Tm:YAG and 3-mm-long Tm:LuAG crystals, each having 5% Tm^{3+} ion concentration. At the maximum driving current, 260 mW of pump power was incident on the crystals. For the vertically polarized pump light, an estimated 28% of the pump light was lost by Fresnel reflection from the crystal surface.

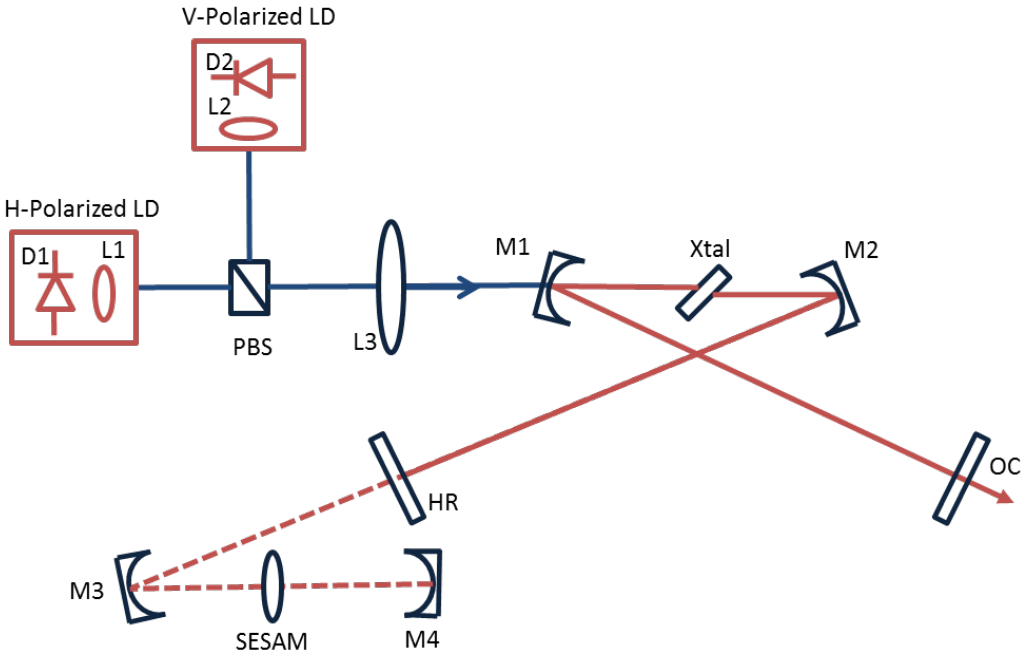

Figure 5.1.1 Schematic of the single-mode diode-pumped Tm:YAG and Tm:LuAG lasers. Dashed lines show the addition to the cavity containing the SESAM saturable absorber to initiate Q-switched mode-locked operation.

For Q-switched mode-locking operation of the lasers, we replace the HR mirror with two extra curved mirrors (M3 and M4, R=5 cm), to obtain an additional focus point (dashed line in Fig. 5.1.1). The distance between the curved mirrors was arranged to be 7.6 cm to preserve the beam waist inside the crystals by using the software we developed (see Chapter 3 for a detailed discussion). A transmitting saturable absorber (SESAM) was placed at that focus point, which could initiate the pulsed operation of the lasers. The SESAM had 0.6% modulation depth with 0.4% non-saturable loss per pass for the 2 μm beams. The pulses are monitored with a 12.5 GHz biased InGaAs detector connected to a 500 MHz oscilloscope and a 3.6 GHz RF spectrum analyzer.

5.2 Results and Discussion

We first measured the power efficiency of the four mirror resonator. We expect more output power than what was was obtained in the previous low-threshold experiments, because of replacing HR with a better quality one and driving the diodes at 140 mA current (this is higher than therated driving current). Figure 5.2.1 shows the graphs obtained from these measurements. For the Tm:YAG case, the output power increased up to 77 mW with a slope efficiency of 39% (31% for the vertically polarized diode). These results become 58 mW and 34% (24%) when we replaced the gain medium with Tm:LuAG crystal. From the slope efficiencies, we can easily observe the effect of the new HR mirror. Because, the values are increased from 22% to 39% for Tm:YAG case (from 19% to 34% for the Tm:LuAG laser), which suggests that the passive loss of the resonator was dramatically decreased as a result of this replacement. The threshold values obtained from these configurations remain in the same level (~30 mW) and also, we observe the same phenomena that the threshold value for the Tm:LuAG laser (32 mW) is less than that for the Tm:YAG laser (35 mW)[53]. Again, it should be noted that the threshold data were obtained from the Tm:LuAG laser system by slope efficiency curve fitting, not directly

from the threshold measurement, because, the diode wavelengths could not be controlled by temperature controllers at low power levels.

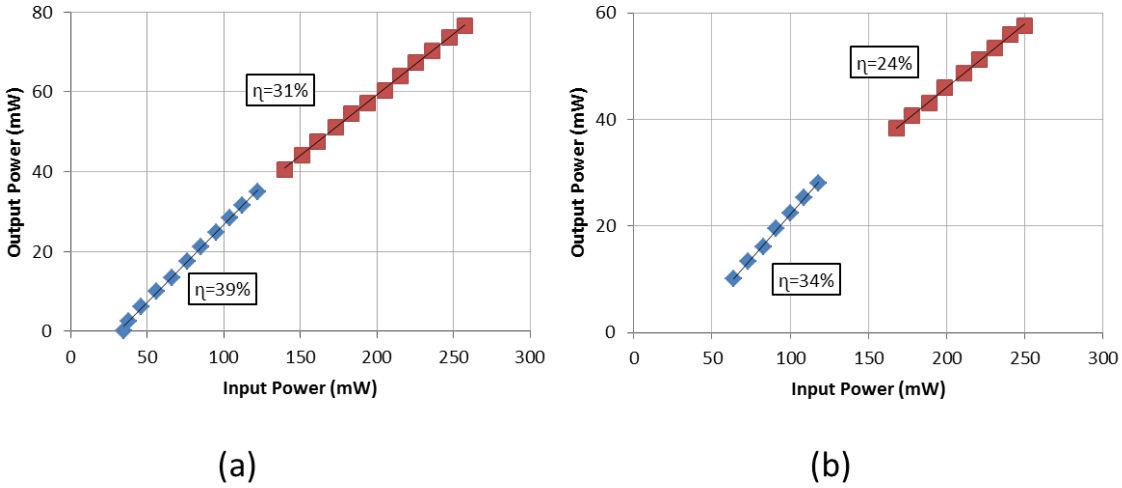

Figure 5.2.1 Measured variation of the output power as a function of the incident power for the (a) Tm:YAG (b) Tm:LuAG laser.

Figure 5.2.2 represents the power efficiency graphs and Figure 5.2.3 shows the Q-switched envelope repetition rate variation with respect to the pump power for the Q-switched mode-locked cases. Q-switched mode-locking could be obtained by driving both diodes together. When vertically polarized diode was turned off, the Q-switched mode-locking regime disappeared. Hence, the threshold values for pulsed regimes could not be determined. In the Tm:YAG laser system, Q-switched mode-locked pulses with 20 mW average output power could be obtained with a 22.5 kHz repetition rate. For the Tm:LuAG case, the average output power remained near 20 mW whereas the repetition rate decreased to 17 kHz. The power slope efficiency for the Tm:YAG laser system (14%) was higher than the value obtained from Tm:LuAG laser system (10%). Although the slope efficiency of Tm:YAG laser was higher than the Tm:LuAG laser, the output power remains in the

same level (A possible reason will be explained later in this section). The minimum repetition rates we could observe from these systems were around 13 kHz.

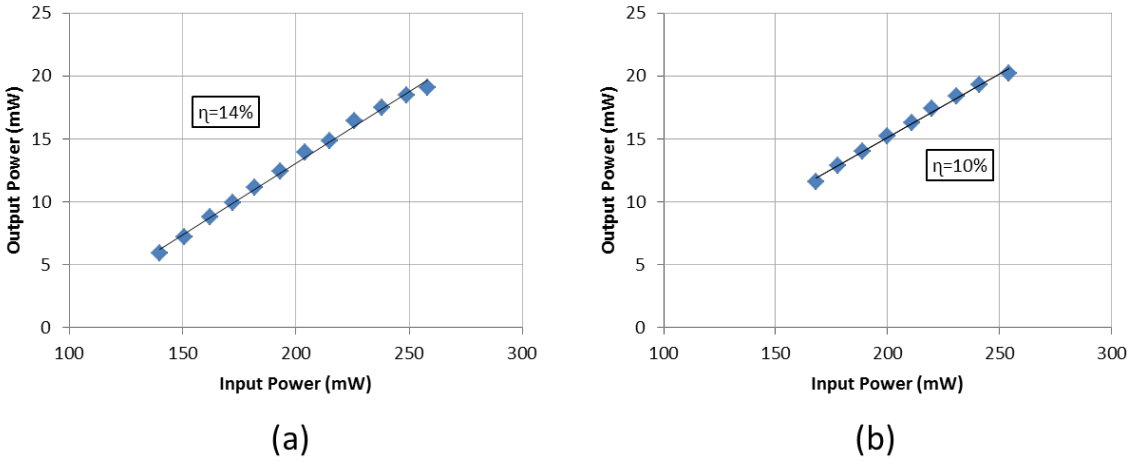

Figure 5.2.2 Measured variation of the output power as a function of the incident power for the (a) Tm:YAG (b) Tm:LuAG laser in Q-switched mode-locked regime.

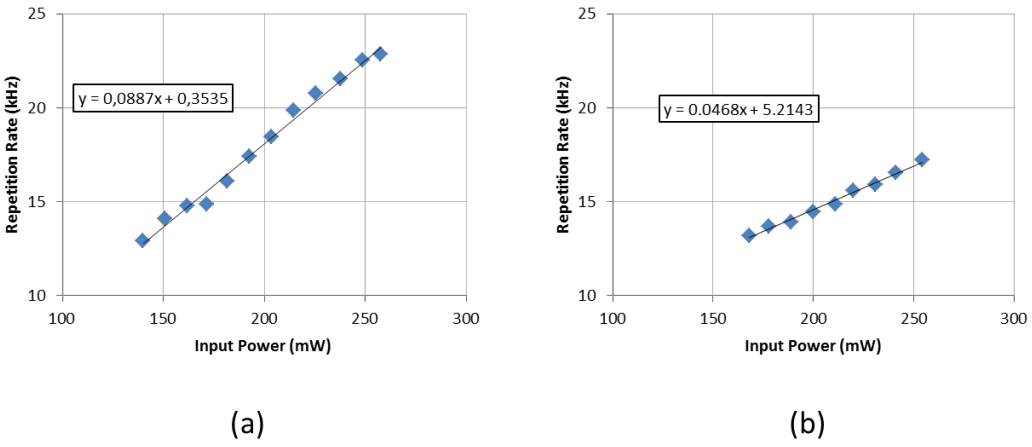

Figure 5.2.3 Measured variation of the repetition frequency of the Q-switched pulse train as a function of the input pump power for the (a) Tm:YAG (b) Tm:LuAG laser.

Figure 5.2.4 shows the pulse trains in different time scales. In the nano-second scale we can observe the separate mode locked pulses at the mode-locked repetition rates (around

170 MHz). In the millisecond range, we observe the Q-switched envelopes of the systems. In the microsecond range, we can easily distinguish the Q-switched pulses and measure the peak to peak time difference to obtain the periods (44 μs for Tm:YAG and 58 μs for Tm:LuAG).

The pulsewidths of the Q-switched pulses are 10 μs and 15 μs long for the Tm:YAG and Tm:LuAG lasers, respectively. Since our average output powers are 20 mW, the Q-switched envelopes carry 88 mW and 77 mW averaged mode-locked pulse powers in the Tm:YAG and Tm.LuAG lasers, respectively. These powers correspond to pulse energies of 880 nJ for the Tm:YAG and 1.2 mJ for the Tm:LuAG lasers.

We can do a very crude estimation of the averaged peak power within the pulse envelope. Since the actual temporal extend of the Q-switched pulse is approximately twice the pulsewidth, and since the repetition rates of these lasers are around 170 MHz, approximately 3400 and 5100 mode-locked pulses are present within one Q-switched burst of the Tm:YAG and Tm:LuAG lasers, respectively. Hence, the mode-locked pulses in Tm:YAG laser system carry 0.26 nJ of energy in average. This value decreases to 0.23 nJ energy in the Tm:LuAG system. To estimate the peak power of our mode-locked pulses, we need to know their durations. However, since our 500 MHz oscilloscope can resolve down to a minimum temporal resolution of 300 picosecond, we cannot directly obtain the mode-locked pulse durations. For the worst scenario, we can assume that our mode-locked pulses are 300 picoseconds long. From this assumption, we can roughly say that the averaged peak powers of the mode-locked pulses are more than 850 mW for the Tm:YAG laser and 750 mW for the Tm:LuAG laser. We expect the actual mode-locked pulsewidth to be significantly smaller than 300 ps, in which case, the actual peak powers are higher.

Finally, we recorded the radio frequency spectra of the lasers (Figure 5.2.5). The measurements were taken at 1 kHz bandwidth. For the Tm:YAG laser, the carrier signal was located around 170 MHz with a 0.15 MHz full width at half maximum (FWHM). On

the other hand, the same signal was located again around 170 MHz but with a 0.5 MHz FWHM for the Tm:LuAG laser. We also observed in the Tm:LuAG system that, the carrier signal sharpens in the middle of the spectrum. This behavior suggests that the laser could be closer to the Q-switching regime rather than the mode-locked regime in the Tm:LuAG laser since the overall bandwidth of the carrier signal was broader, possibly due to additional modulation brought about by Q switching.

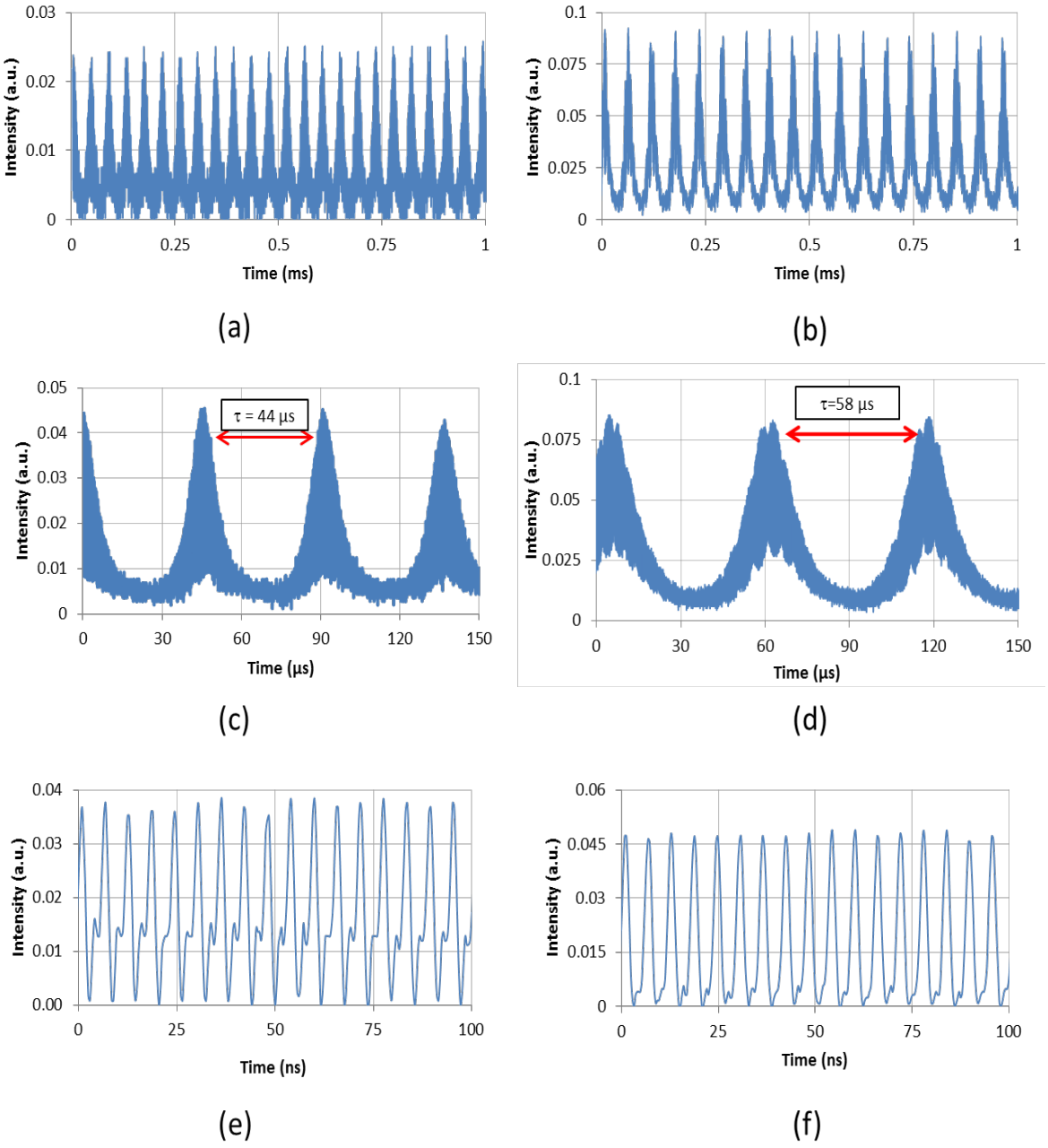

Figure 5.2.4 Pulse trains for (a,c,e) the Tm:YAG and (b,d,f) Tm:LuAG in different time scales.

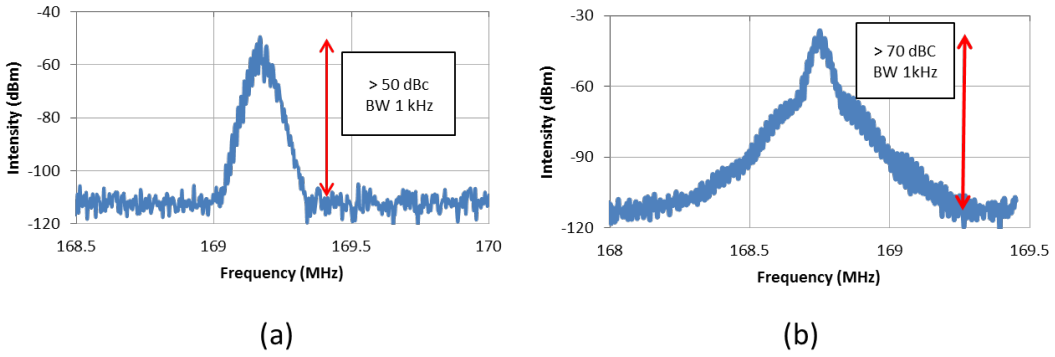

Figure 5.2.5 Radio frequency spectra of the Q-switched mode-locked (a) Tm:YAG (b) Tm:LuAG lasers.

5.3 Conclusions

In conclusion, by inserting a saturable absorber into the Tm:YAG and Tm: LuAG lasers, we obtained low-threshold, low-cost Q-switched mode-locked laser operation in the 2 µm regime. In this regime, up to 22.5 kHz Q-switched repetition rates were obtained. Moreover, the mode-locked pulses had more than 1.5 W of peak power and 250 pJ pulse energies. We believe that, these powers and energies in the 2 µm regime will be more attractive for biomedical, coherent LIDAR and remote sensing applications.

Chapter 6

SELF-Q-SWITCHED OPERATION of Cr:LiCAF LASERS

In this chapter we introduce a different technique to obtain Q-switching operation from solid-state lasers: self-Q-switching. Different from other techniques, no extra modulation element is used to initiate Q-switching mechanism. In the first section of this chapter, we introduce the mechanism and provide a discussion on the historical development of this method. Section 2 describes the experimental setup of the self Q-switched Cr:LiCAF laser. In Section 3, we present the experimental results on the observed self-Q-switching phenomena in detail. Finally, in Section 4, we summarize the results, provide a general review of the SQS process and propose some possible causes of the effect.

6.1 Self-Q-Switching

Another mechanism for the generation of nanosecond-to-microsecond pulses is self-Q-switching (SQS), first named by I. Freund in 1968 [54]. In this technique, no special modulation elements are required inside the laser cavity to initiate and sustain the pulsing mechanism. The laser cavity simply consists of an optical resonator, a suitable gain medium, and a pump source. SQS was first observed in flashlamp-pumped ruby lasers in 1968 [54-57]. In these studies, to initiate SQS, either the laser crystal was operated at liquid-nitrogen-temperatures [56, 57], or one of the laser cavity end-mirrors was misaligned in systems operated at room temperature [54, 55]. We note here that in these initial studies, the pump sources were also pulsed [54-57]. Hence, SQS was used to switch the laser operation so that, it produces a giant single high-energy laser pulse rather than several lower energy pulses with unequal energy and period (transition from random spiking to

SQS operation) [54-57]. In the same year, the SQS effect was also observed in Nd:$SeOCl_2$ liquid lasers under low feedback conditions (using high output coupling) [58]. A year later, SQS was reported in Nd:YAG laser media at 77 °K [59]. In 1970, Mikaelyan *et al*. showed that SQS could also be initiated by adjusting the cavity length [60]. In 1976, SQS was demonstrated in a quasi cw pumped room-temperature Nd:YVO_4 laser at 1.06 μm and 1.34 μm by using cavity misalignment [61]. In 1978, for the first time, A. Szabo obtained SQS operation in a cw argon ion laser pumped ruby laser operated at 80 °K (earlier studies were all with pulsed pump sources [62]). Since then, SQS operation has been reported in flashlamp pumped Cr:LiSAF lasers [5, 63], Nd:YVO_4 microchip lasers [64], Erbium fiber lasers [65], broad area semiconductor lasers [66], Nd:YVO_4/KTP lasers [61], ytterbium fiber lasers [67], and thulium-fiber lasers [68]. The underlying mechanism for SQS is not very well understood and it might differ depending on the physical characteristics of the gain medium and the operating regime of the laser. In the case of Cr^{3+}-doped gain media such as ruby and Cr:LiSAF, the SQS effect is attributed to a nonlinear loss mechanism created by a time-dependent lens occurring inside the gain medium and originating from refractive index changes induced by the population inversion [5, 63, 69-72]. However, as a recent study by Godin *et al*. demonstrates, the origin of the nonresonant contribution to refractive index change in Cr^{3+}-doped gain media (as well as the underlying physics behind SQS effect) is not yet clear and requires further investigation [73].

In this chapter, we report on the observation of the SQS effect in Cr:LiCAF gain media for the first time to our knowledge. In our experiments, SQS could be initiated in a standard 4-mirror, x-folded Cr:LiCAF laser that was pumped with a continuous-wave (cw) single-spatial-mode diode at 660 nm. No special modulation elements such as saturable absorbers or acousto-optic switches were present in the cavity. In the regular cw regime, at an incident pump power of 140 mW, the Cr:LiCAF laser produced a diffraction limited output beam with greater than 50 mW of output power. The free running laser spectrum was

centered around 795 nm and had a full width at half maximum (FWHM) of about 0.5 nm. However, by fine adjusting the separation of the cavity curved mirrors, we could initiate SQS in the Cr:LiCAF laser. At several values of curved mirror separation (not necessarily near the edge of the stability region), the laser switched from cw operation to SQS operation with an accompanying decrease in the output power. In the SQS regime, the laser generated pulses with around 5 microsecond duration at repetition rates between 10 and 30 kHz, and with average powers ranging from 30 to 45 mW. The corresponding pulse energies and peak powers were as high as 3.75 microjoule and 590 mW, respectively. In the SQS regime, the laser transverse mode switched from being single-mode to a structured beam containing higher-order spatial modes, and spectral widening up to 10 nm (FWHM) was also observed. When the laser was forced to operate in single transverse mode with the insertion of an intracavity slit, the effect disappeared and the laser returned back to normal cw operation.

As mentioned above, similar self-pulsing phenomena have been reported earlier in several other gain media. However, to our knowledge, these systems were mostly flashlamp-pumped, and sometimes required cooling of the crystal [57] or misalignment of the laser cavity end-mirrors [55] to initiate the SQS effect. Moreover, for the first time, we present data that delineate the interesting role of the cavity geometry, in particular, the cavity curved mirror separation, on self-pulsing phenomena. We believe that detailed investigation of the SQS effect is important for several reasons. First, as earlier studies have shown, this effect can be used in a favorable way to obtain high-energy microsecond pulses. Second, because this effect can be deleterious in building lasers operated in the pure cw or cw mode-locked regime, it is of paramount importance to be aware of the conditions under which it is initiated or it can be prevented. We believe that the experimental data presented here will help in better understanding of the underlying physical mechanisms behind the self-pulsing phenomena.

6.2 Experimental Setup

Figure 6.2.1 shows a schematic of the Cr:LiCAF laser cavity that was used in the experiments. A linearly-polarized, 660-nm, 140 mW, AlGaInP multi-quantum well single-spatial-mode diode laser (SMD, HL6545MG, Hitachi) with a diffraction-limited beam profile was used as the pump source. An aspheric lens with a focal length of 4.5 mm (NA = 0.55) collimated the diode output beam. A converging lens with a focal length of 60 mm focused the collimated pump beam into the Cr:LiCAF crystal. The Cr:LiCAF laser resonator was a standard x-folded, astigmatically compensated cavity, consisting of two curved pump mirrors, each with a radius of curvature (roc) of 75 mm (M1 and M2), a flat end high reflector (HR), and a flat output coupler (OC). Mirrors M1-M2-HR had a reflectivity of greater than 99.9% in the 730-910 nm wavelength range and had >98% transmission in the pumping window. The cavity arm lengths were 25 cm (OC arm) and 35 cm (HR arm), giving a laser mode size of ~15-20 μm inside the Cr:LiCAF crystal. The gain material was a 4 mm long, 2.6 mm wide, and 1 mm thick piece of Cr:LiCAF crystal with 5 mole % chromium (corresponding chromium concentration ~4.75×10^{20} ions/cm^3 [74]) and was grown at the Leibniz Institute for Crystal Growth by using the Czochralski method [75-77]. The crystal absorbed 95% of the TM polarized pump light at 660 nm. The estimated passive losses of the Cr:LiCAF crystal were below 0.15 % per cm, which corresponds to a figure of merit (FOM) of above 2000 [78]. Neither the pump diode nor the Cr:LiCAF laser crystal required active cooling. Temporal characterization of the laser was performed using a 1 GHz Si photodetector and a 500 MHz digital sampling oscilloscope using a 10 kΩ termination. The laser spectrum was measured with a scanning, fiber coupled spectrometer (Ocean Optics USB2000) and the laser transverse mode was monitored with the Coherent Lasercam HR beam profiler.

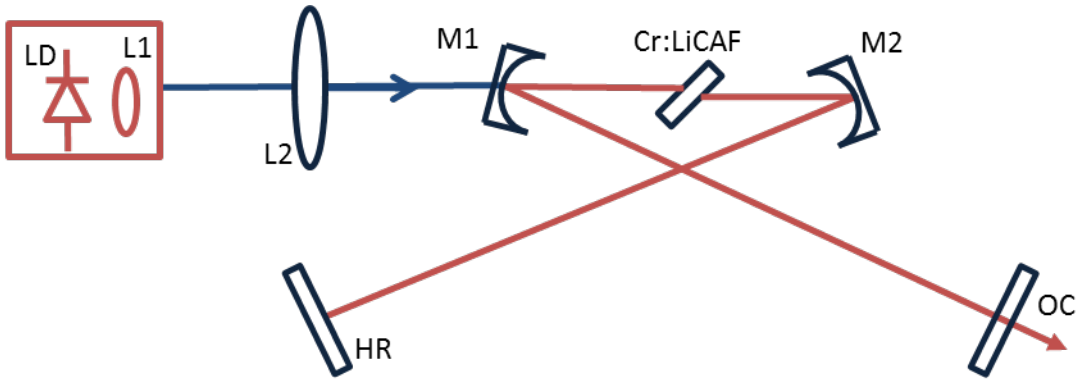

Figure 6.2.1 Schematic of the Cr:LiCAF laser pumped with one single-spatial-mode diode (SMD) laser. The laser operates in self-Q-switched (SQS) mode at some discrete values of the curved mirror (M1-M2) separation.

6.3 Experimental Results

In our experiments, we observed the SQS operation of the Cr:LiCAF laser in a reproducible manner at several positions within the cavity stability range. To elucidate this regime of operation, the power efficiency data shown in Fig. 6.3.1 were taken. The graph shows the measured variation of the laser output power within the outer stability range as a function of the curved mirror separation (M1-M2 separation in Fig. 6.2.1). The data were taken at an incident pump power of about 140 mW, by using a 0.75% transmitting output coupler and without any active cooling of the gain medium. Also, while taking the data, the position of the laser crystal, pump focusing lens and the cavity alignment were first optimized at the center of the stability range. Then, during the measurements, only the curved mirror separation was varied without adjusting any other cavity component.

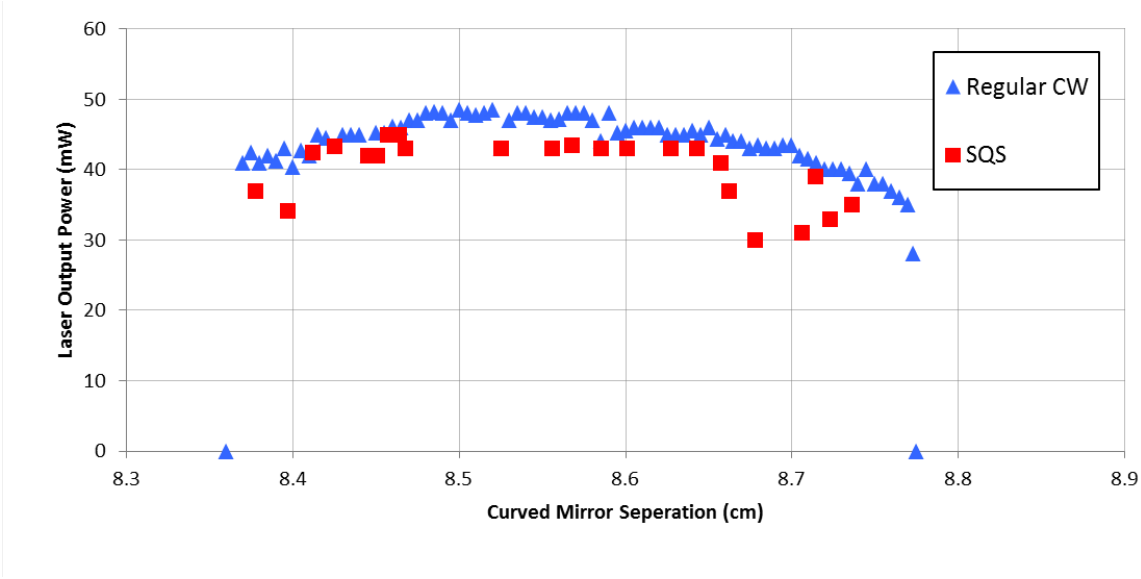

Figure 6.3.1 Experimentally measured variation of the laser output power as a function of the curved mirror separation within the outer stability range. (Triangles: pure cw operation, Squares: self Q-switched operation)

At most values of the curved mirror separation, the Cr:LiCAF laser operated in regular cw regime (shown with solid triangles in Fig. 6.3.1). At these positions, the laser was quite stable with a TEM_{00} output (M^2 was below 1.05) and average powers of 40 to 50 mW could be obtained. Furthermore, the laser output was quite stable with no noticeable tendency toward Q-switching and typical free running laser line widths were about 0.5 nm near the center wavelength of 795 nm. However, at several distinct positions within the stability range (marked by solid squares in Fig. 6.3.1), the laser switched to SQS operation. Once initiated, SQS operation was quite stable and could be reproduced at these points in a repeatable fashion. We note here that obtaining SQS operation required fine adjustment of the curved mirror separation within about 10 micrometers. At these specific curved mirror distances, the laser output power was in general lower compared to the cw case. Moreover, during SQS operation, the laser transverse mode also switched from being single-mode to a

structured multimode, and spectral widening was also observed. However, during SQS operation, when we inserted a mechanical slit inside the laser resonator to force the laser to operate in pure TEM_{00} mode, the laser switched back to pure cw operation. This was accompanied with an increase in the output power and a decrease in the spectral bandwidth.

In summary, with our setup, transition to SQS regime of operation was signaled by several factors including (i) an abrupt decrease in the output power, (ii) a sudden widening of the output optical spectrum, (iii) pulsing of the laser output in the time domain, and (iv) a change in the transverse mode structure. We also note here that the SQS positions indicated in Fig. 6.3.1 with solid squares do not represent the complete list as there were other positions, not marked in Fig. 6.3.1, where weak SQS tendency was observed. Moreover, even though SQS operation could be initiated at several different positions within the stability range, the temporal characteristics of the laser output such as pulse shape, pulse modulation depth, and repetition frequency varied at different positions. We have also checked the SQS operation tendency within the inner stability range. The inner stability range showed similar SQS operation parameters. However, compared to the outer stability range, we observed SQS operation at fewer discrete positions. In the remaining parts of this section, we will provide representative data (Figs. 6.3.2-6) to describe the rich behavior of the SQS operation that was obtained at different curved mirror separation distances.

Figure 6.3.2 shows the output characteristics at the curved mirror separation of 8.45 cm taken at an incident pump power of 140 mW. For this case and similar others, we have observed relatively weak widening of the optical spectrum (widening from about 0.5 nm to 1.2 nm). When SQS operation was initiated by fine adjustment of the curved mirror separation, the average output power of the Cr:LiCAF laser decreased from 45 mW to 42 mW. The laser produced 6.5 microseconds long pulses at a repetition rate around 17 kHz with 11% duty cycle. The corresponding pulse energy and peak power were 2.5 microjoule

and 360 mW respectively. The SQS operation also transferred the TEM_{00} laser output to a structured beam, consisting of higher-order modes (Fig. 6.3.2(d)). In general, during SQS operation, the laser transverse mode had rectangular transverse mode patterns. For most of the cases, the mode became multimode only along one axis and stayed as a fundamental mode along the other axis (modes such as TEM_{10}, TEM_{20}, TEM_{30}, TEM_{01}, TEM_{02}, and TEM_{03} were observed). As an example, at the mirror separation of 8.45 cm, the M^2 parameter of the beam was measured to be around 5 along the fast axis. One should not forget that, as indicated by earlier studies, the observed transverse beam profile as well as the divergence and, hence, the M^2 of the beam are time dependent during SQS operation [71]. Hence, the beam profile shown in Figs. 6.3.2 and 6.3.3 are time-averaged acquisitions. In our experiments, once the desired curved mirror separation was obtained, the SQS operation was in general quite robust, meaning that the laser stayed in the SQS regime and did not jump between SQS and regular cw operation. The pulsewidths were also quite stable and the pulse-to-pulse energy variation was below 20 %. For the SQS configuration summarized in Fig. 6.3.2, the repetition frequency of the laser varied by about 20% around 17 kHz due to fluctuations in laser dynamics (see Fig. 6.3.2 (b)). It may be possible to further reduce the jitter by active modulation of the pump power or by quasi cw pumping.

Even more stable SQS operation with lower amount of variation in the laser parameters (10%) was obtained at several other curved mirror separations. For this case, the widening of the optical spectrum was also more pronounced. As a typical example, Fig. 6.3.3 shows the measured SQS laser parameters at a curved mirror separation of 8.46 cm. The laser output spectrum was significantly broader with a width (FWHM) of 10 nm. The coherence length of such a broad–bandwidth source around these wavelengths is about 30 micrometers in air; which could be useful for applications such as high axial resolution optical coherence tomography [79].

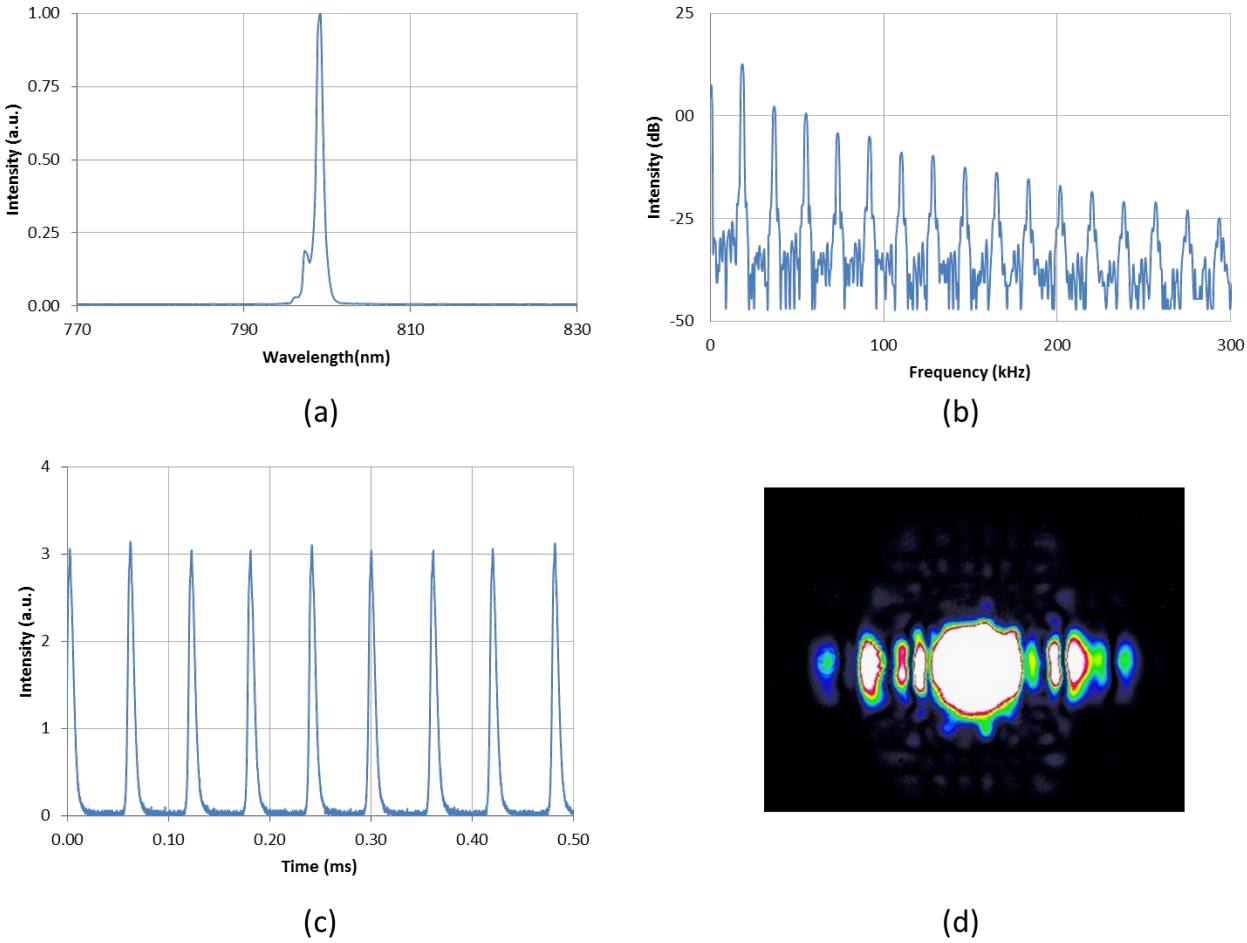

Figure 6.3.2 (a) The measured optical spectrum, (b) fast Fourier transform of the output and (c) the measured temporal output profile and (d) the output transverse mode for the self-Q-switched Cr:LiCAF laser at the curved mirror separation of 8.45 cm.

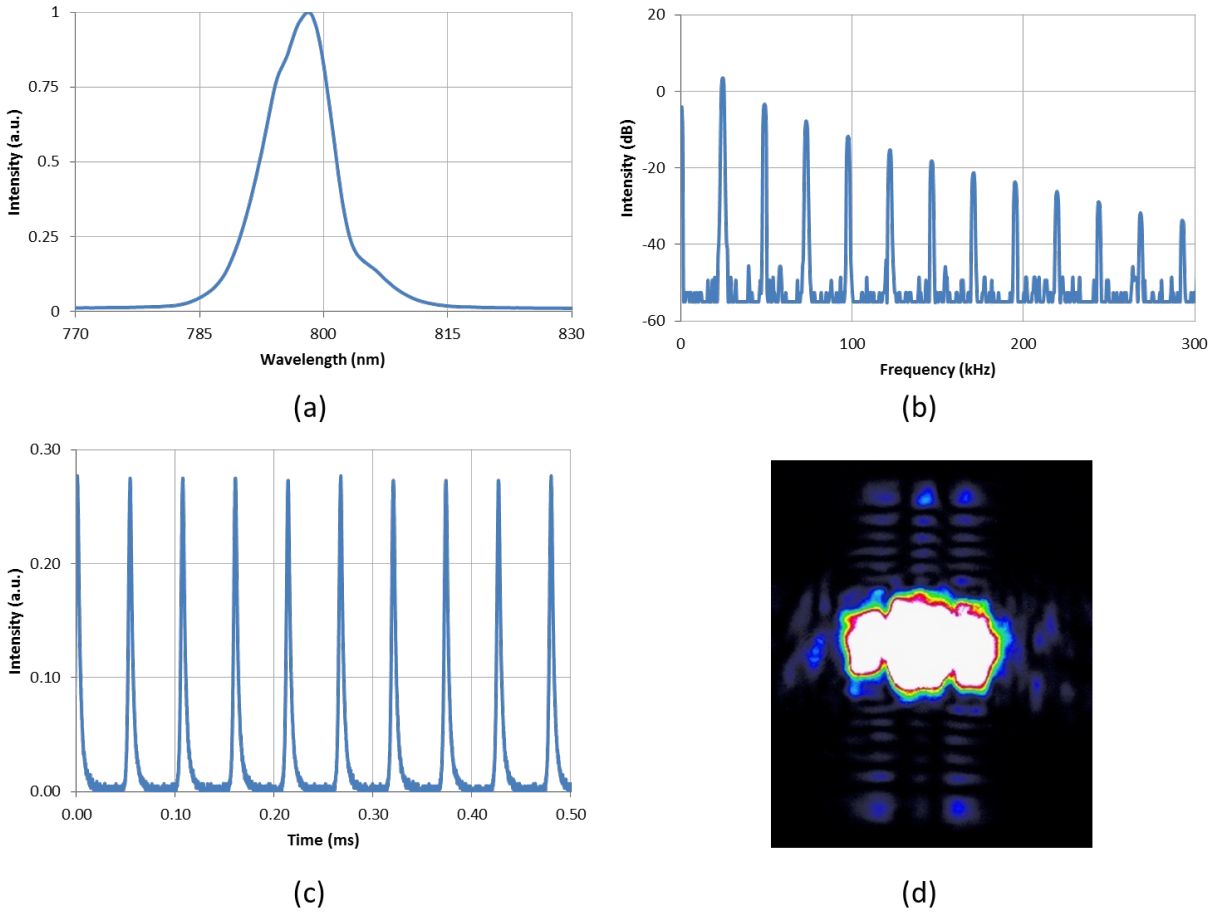

Figure 6.3.3 (a) The measured optical spectrum, (b) fast Fourier transform of the output and (c) the measured temporal output profile and (d) the output transverse mode for the self-Q-switched Cr:LiCAF laser at the curved mirror separation of 8.46 cm.

Using the 0.75 % output coupler, we also observed SQS operation at repetition rates as low as 12 kHz. The pulses were 6 microseconds long and the laser average power was around 45 mW (7 % duty cycle). The optical spectrum width was centered near 790 nm with a FWHM of 7 nm. The corresponding pulse energy and peak power were 3.75 microjoule and 587 mW, respectively. These results show that, using SQS, the peak power of the laser can be scaled by about 10 times. Such a scaling can be useful for performing

nonlinear experiments such as intracavity second harmonic generation [78]. We note here that, SQS has also been observed in earlier experiments with higher power multimode or tapered diode pumped Cr:LiCAF laser systems [80, 81]. Hence, using high power diodes, it is feasible to scale the pulse energies and peak powers reported in this study to at least 200 microjoule and 20 W levels, respectively. On the other hand, the current system with reasonable average and peak powers is still attractive for many applications due to its simplicity, compactness, and low cost.

By using standard passive Q switching theory (Eq. 2.3.4-6), we can model the SQS action as a simple saturable absorber and use the experimental pump-dependent repetition rate data to determine the small-signal saturable loss. The SQS data that were used for the determination of Q_0 were taken at the curved mirror separation of 8.46 cm. By using the cavity design software we developed, the laser beam waist inside the gain medium was estimated to be 25 μm, giving A=2.75x10^{-5} cm^2. Hence, from Eq. 2.3.6, the corresponding saturation power was determined to be about 3W.

To determine the small-signal round-trip gain G_0, the power efficiency data of the cw and SQS Cr:LiCAF laser were recorded as shown in Fig. 6.3.4. At each pump power level, the cw output power was used together with equations (Eq. 2.3.4) and (Eq. 2.3.5) above to determine the corresponding value of G_0. Figure 6.3.5 shows the measured variation of the repetition rate of the pulse train as a function of the incident pump power. By using Eqs. 2.3.4 and 2.3.5, the variation of the repetition frequency f_{rep} as a function of G_0 was determined (taking τ_f as 175 μs for Cr:LiCAF [74]). Linear list-squares fit to the data gives a best-fit value of 0.5% for Q_0. Also note that when the laser makes a transition to SQS regime, the threshold pump power increased from 24 mW to 44 mW due to the additional 0.5% small-signal loss represented by Q_0. Moreover, the slope efficiency also decreased from 47% to 33%. For both cases, the transmission of the output coupler was 0.75%.

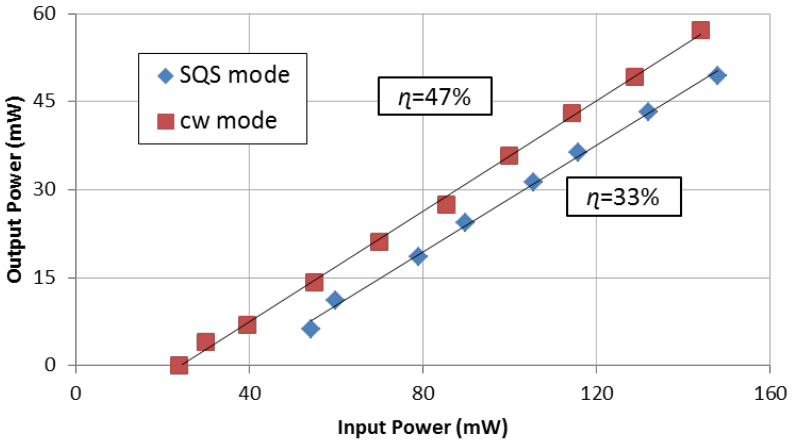

Figure 6.3.4 Power efficiency data of the cw and SQS Cr:LiCAF laser operated with a 0.75% output coupler

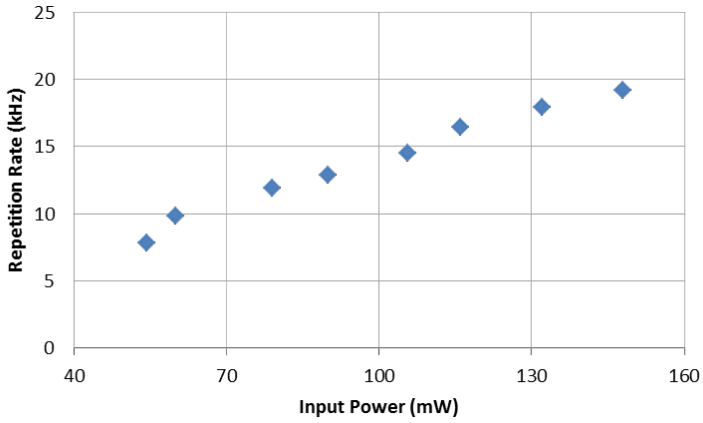

Figure 6.3.5 Measured variation of the frequency of the repetitive pulse train as a function of the input pump power.

Similar to the 0.75% output coupler, the output couplers with 0.1 %, 0.25%, 2% and 3% transmission also required fine adjustment of the curved mirror separation to initiate SQS operation. Similarly, SQS could be observed at several discrete curved mirror separations as in Fig. 6.3.1. Roughly speaking, with lower output coupling, SQS operation could be

initiated at larger number of discrete mirror separation values. This might be due to the presence of higher intracavity powers at lower output coupling.

Since SQS parameters strongly depend on the exact mirror separation value that is used, it is not possible to make a very precise comment on the effects of output coupling on SQS parameters. However, comparing the SQS operation results taken with different output couplers, we can qualitatively conclude that with increasing output coupling, (i) self-Q-switched pulsewidth decreases, (ii) pulse repetition frequency increases, and (iii) the output optical spectral width decreases. For example, 2.8 microsecond long pulses at 27 kHz repetition rate were obtained with an average power of 33 mW by using a 3% output coupler (1.2 microjoule pulse energy, 410 mW peak power, 7.6% duty cycle, and 37 microsecond period). The spectral width was 5.8 nm wide and was centered around 780 nm. On the other hand, 4.8 microsecond long pulses at 15 kHz repetition rate were generated at an average power of 19 mW using the 0.1% transmitting output coupler (1.3 microjule pulse energy, 250 mW peak power, 7.2% duty cycle, 67 microsecond period). For this case, the spectral width was centered around 794 nm with a FWHM of about 10 nm.

In our experiments, the repetition rate during the SQS operation varied between 10.35 kHz and 31 kHz at different curved mirror separation distances (at the full pump power level). Here, we would like to first compare this frequency range with the relaxation oscillation frequency of the Cr:LiCAF laser. Taking Δv as 200 MHz, r as 10, T as 0.0075, L_c as 0.002, the estimated relaxation oscillation frequency of our laser comes to 330 kHz (Eq. 2.3.3), which is significantly above the observed range of SQS repetition frequencies. However, in some configurations, in which the pulsewidth is relatively long, we have observed a higher-frequency oscillation in the pulse intensity. For example, Fig. 6.3.6 shows the measured temporal profile of the laser output taken with the 0.1 % transmitting output coupler. The pulse train intensity had a weak oscillation around 250 kHz. We

believe that the observed intensity oscillation within the pulse envelope was due to relaxation oscillations

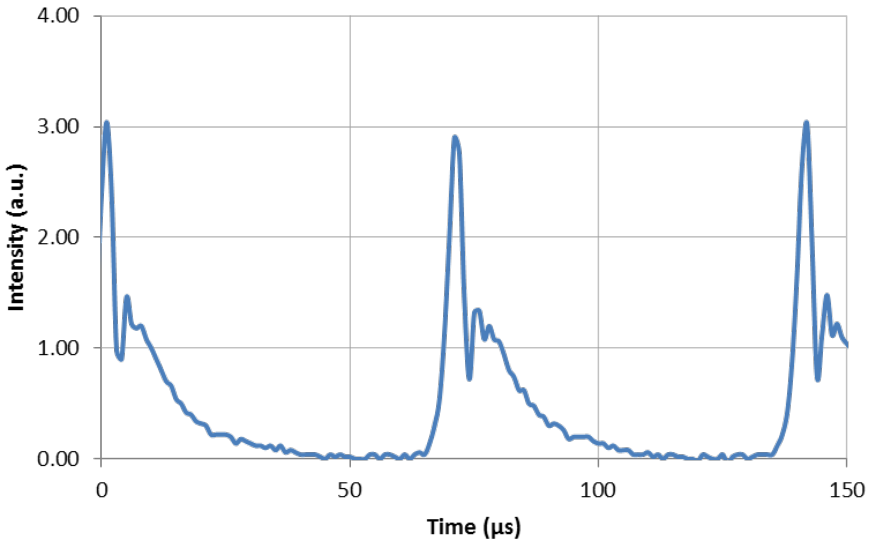

Figure 6.3.6 Measured temporal output profile for the self-Q-switched Cr:LiCAF laser taken with a 0.1 % output coupler. One can notice oscillations in the pulse intensity at higher frequencies (around 250 kHz), which might be caused by relaxation oscillations

As was mentioned in the introduction, most of the earlier studies report SQS operation in pulsed pumped systems. Hence, in these systems, the SQS frequency was the same as the pumping frequency. As an example, Weber et al., obtained 200 to 500 ns pulses from a Cr:LiSAF laser pumped by rectangular 60 microsecond flashlamp pulses at a repetition rate of 100 Hz [5]. There are only a few reports of SQS operation in cw pumped systems. In [82], SQS has been reported in cw pumped Nd:YVO_4 laser, and pulsewidths of 40 ns were obtained by misalignment of cavity end-mirrors. However, the SQS repetition frequency was not mentioned in this study. In another study, SQS was obtained in a cw pumped ruby laser, and pulses with 2 nanosecond duration at 3-kHz repetition rate were obtained [62]. In comparison, the SQS frequency we observed in Cr:LiCAF is about 5 times larger than that reported in ruby. The laser systems are quite different and the difference in the SQS

frequencies may be due to numerous factors including the fluorescence lifetime, small-signal gain, and the effective small-signal loss parameter of the effective SQS action as can be seen from Eq. 2.3.4. In particular, the fluorescence lifetime in ruby (3 ms) is about 17 times higher than that in Cr:LiCAF.

6.4 Summary and Discussions

In summary, to the best of our knowledge, this study reports the SQS operation of a Cr:LiCAF laser for the first time. Furthermore, this is also the first demonstration of SQS in a cw pumped room-temperature solid-state laser. Different from most of the earlier studies, initiation of SQS action in the present study did not require the misalignment of the cavity optics. SQS could be initiated just by fine adjustment of the curved mirror separation within the cavity stability range. Moreover, SQS was observed at several different values of curved mirror separation and these points were not necessarily at the edge of the stability range. Finally, the pump power levels we have used here are also relatively low. Hence, compared to the earlier reports in the literature, this study shows unique characteristics of the mechanism responsible for obtaining SQS. We hope that, the data presented in this work will help in better understanding of SQS and the physics behind it.

For our case, there does not exist any earlier reports of SQS in Cr:LiCAF. Hence, the physical mechanism behind SQS effect is not yet studied. However, both Cr:LiCAF and Cr:LiSAF belong to the Cr:Colquiriite family, and roughly speaking, they possess similar optical, physical and spectroscopic properties [3]. Actually, when we repeat our SQS experiments with a Cr:LiSAF laser (just replacing the Cr:LiCAF crystal with a 5 mm long, 1.5% chromium doped Cr:LiSAF), we have also observed SQS by fine adjustment of the curved mirror separation. However, SQS operation was less stable and could be obtained only at fewer locations. Hence, both media also show similarities in terms of SQS operation. Earlier studies with Cr:LiSAF gain media suggest that SQS in Cr:LiCAF is

probably due to the time dependent population lens created by population inversion [5, 63, 69-72]. However, it is hard to make concluding remarks and further studies are required for better understanding of a general theory of SQS action.

Chapter 7

TAPERED DIODE PUMPED CONTINUOUS WAVE ALEXANDRITE LASERS

In this chapter, we describe a low-cost and efficient Alexandrite ($Cr:BeAl_2O_4$) laser that is pumped by a high-brightness tapered diode laser. The tapered diode provides up to 1.1 W of output power and its wavelength can be fine-tuned to either 680.4 nm (R1 line) or 678.5 nm (R2 line) for efficient in-line pumping. Continuous wave (cw) output powers of 200 mW, slope efficiencies as high as 38% and a cw tuning range extending from 724 nm to 816 nm have been achieved. The cw power levels and slope efficiencies are the highest demonstrated so far from such a minimal complexity and low-cost system based on the Alexandrite gain medium. Consequently, tapered diodes operating in the red spectral region have the potential to become the standard pump sources for cw Alexandrite lasers in the near future. The chapter is organized as follows: Section 7.1 describes the spectral properties and previous laser performances of alexandrite crystals. Section 7.2 introduces the experimental setup and methods employed. Section 7.3 presents detailed continuous wave lasing results. In Section 7.4, we summarize the results and provide a general discussion.

7.1 Introduction

Ti:sapphire has the broadest gain bandwidth among all solid-state laser media, facilitating tuning from 680 to 1180 nm [83], as well as direct generation of pulses as short as 5 fs [84]. The ideal pump wavelength for Ti:Sapphire is around 500 nm [85]. However, due to the lack of suitable low-cost and high-power diode lasers in this spectral region, currently Ti:sapphire lasers are pumped by GaN diodes at 450 nm [86-89]. In a recent

work, using two 1.2 W multimode, single emitter diodes as the pump source, Durfee et al. generated 15-fs pulses with 34 mW average power from a Kerr-lens mode-locked Ti:Sapphire laser [88]. Cw powers as high as 159 mW and mode-locked powers as high as 101 mW (111 fs long pulses) have also been reported from a similar diode pumped system [90]. Progress in directly diode-pumped Ti:sapphire laser systems is promising. Currently the optical-to-optical conversion efficiency of the systems is rather low (5%), partly due to the low pump beam quality and high passive losses of the Ti:Sapphire gain medium [86]. We also note here that, frequency doubled tapered diode lasers have also been recently demonstrated as a possible pump source for Ti:Sapphire [91].

Similar to Ti:sapphire, Cr^{3+}-doped laser materials also possess broad emission bands around 800 nm. Moreover, their strong and broad absorption bands in the visible region of the spectrum enable wavelength and polarization flexible direct diode pumping by low-cost red diodes (630-690 nm). There exists a relatively large number of Cr^{3+}-doped materials in which lasing has been reported [74]. Only a few like Cr:Colquiriites (Cr: LiSAF [92], Cr:LiCAF [74], Cr:LiSGaF [93]), emerald ($Cr:B_3Al_2(SiO_3)_6$) [94, 95] and Alexandrite ($Cr:BeAl_2O_4$) [96-100] are suitable for efficient laser operation with slope efficiencies above 50% since most of the other candidates suffer from strong excited-state absorption. In this work, our attention has been focused on Alexandrite due to its blue-shifted gain profile compared to Cr:colquiriites. The peak emission of Alexandrite is around 750 nm. This wavelength is quite important for optimum excitation of several widely used fluorophores in multiphoton microscopy, including DAPI (4',6-diamidino-2-phenylindole dihydrochloride), Alexa flour 488, indo-1, and fura-2 [28-31].

Table 7.1.1 Comparison of the spectroscopic and laser parameters of the gain media Ti:sapphire, Cr:LiCAF and Alexandrite.

Gain Medium	$Ti^{3+}:Al_2O_3$ (Ti:Sapphire)	$Cr^{+3}:LiCaAlF_6$ (Cr:LiCAF)	$Cr^{+3}:BeAl_2O_4$ (Alexandrite)
Maximum gain wavelength (nm)	790 [101]	780[101]	750 [98]
Tuning range (nm)	660-1180 [83]	720-887 [74, 102]	701-858[98, 103]
Peak emission cross section (σ_{em}) ($x10^{-20}$ cm^2)	41 [104]	1.3 [104]	0.7 [99]
Room-temperature fluorescence lifetime (τ_f) (μs)	3.2 [104]	175 [104]	262 [99]
$\sigma_{em}\tau_f$ (μs $x10^{-20}$ cm^2)	131 [104]	228 [104]	183 [99]
Intrinsic slope efficiency (%)	64 [105]	67 [74], 69[102]	65 [106]
Relative strength of excited-state absorption	0 [85]	0.18 [107]	~0.1 [108]
Passive losses (%/cm)	2 [86]	0.15[109]	0.06 [106]
Crystal figure of merit (FOM)	150 [86]	2150 [109]	3000
Thermal conductivity (W/K.m)	28 [110]	5.1[110]	23 [99]
$T_{1/2}$, $\tau_F(T_{1/2})=0.5\tau_R(C)$	~100 [85]	255[111],190 [112]	225 [98]

Alexandrite (Cr-doped chrysoberyl) was first shown to lase in 1978 by Walling et al [97]. It has many superior optical and thermal properties (see Table 7.1.1), including an intrinsic slope efficiency of 65% [106], a broad tuning range from 700 to 860 nm [98, 103], lack of concentration quenching of fluorescence lifetime [101] and, interestingly, increased laser performance at elevated temperatures above room temperature [103]. Due to all of these, Alexandrite was one of the most popular tunable lasers in the market during the 1980s [101]. This continued until the emergence of Ti:sapphire systems, at which time attention paid to Alexandrite lasers began to diminish. However, we believe that with the recent progress in laser diode technology, Alexandrite lasers can now offer a low-cost,

efficient, and compact alternative to the existing Ti:sapphire laser technology in selected areas of applications, especially for multi-photon microscopy.

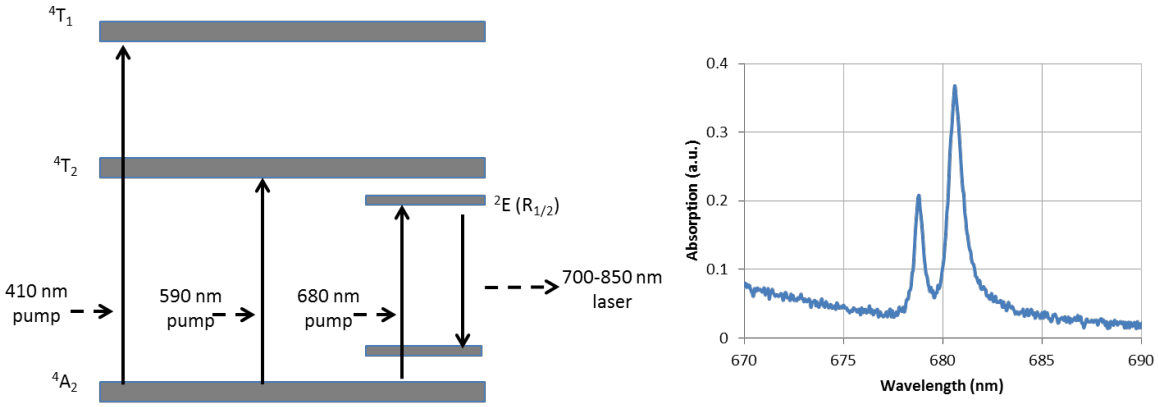

(a) (b)

Figure 7.1.1 (a) Simplified energy level diagram for the Alexandrite gain medium. Lasing occurs between the vibronically broadened $^4T_2$ and $^4A_2$ levels. (b) Measured variation of the absorption coefficient as a function of wavelength for the transition from the $^4A_2$ ground level to the doublet of the ^2E level for the E//b axis (in absorption coefficient scale).

Figure 7.1.1 shows a simplified energy level structure for Alexandrite in E//b orientation. Transitions from the ground state to the vibronically broadened $^4T_1$ and $^4T_2$ states generate two broad (FWHM around 100 nm) and strong absorption bands with peaks around 410 nm and 590 nm [97]. These states have relatively short lifetimes (the intrinsic lifetime of $^4T_2$ state is around 6.6 μs). Moreover, similar to ruby [1], the metastable ^2E state lies below the vibronically broadened $^4T_2$ level in Alexandrite. Hence, ions excited to the $^4T_1$ and $^4T_2$ states rapidly decay to the metastable ^2E state with a lifetime of around 1.54 ms [99]. Using transitions from the ^2E level to the ground state ($^4A_2$), lasing at the sharp line around 680.4 nm could be obtained (three-level lasing mode). The same transition produces lasing at 694.3 nm in ruby [1].

One can directly pump Alexandrite laser ions to the storage level (in line pumping to level ^2E) to reduce the energy difference between the pump and lasing wavelengths and hence to minimize the quantum defect. The ^2E level is actually an orbital doublet (R_1 and R_2 lines), and the $^4A_2 \rightarrow R_{1/2}$ transitions (zero-phonon transitions) create two narrow (FWHM around 0.5 nm) absorption peaks at 678.5 nm and 680.4 nm [98]. The graph in Fig. 7.1.1 (b) shows the measured absorption spectrum of Alexandrite in this region. Diverse excitation bands (broadband $^4T_{1/2}$ excitations and narrowband $R_{1/2}$ excitations) allow different pump options for Alexandrite. Flashlamps [113], Xe/Hg arc lamps [99, 114], krypton ion lasers (647 nm) [115], dye lasers (615-680 nm) [106], frequency doubled neodymium lasers around 530 nm [116, 117] and even sun light [118] have been used for pumping continuous-wave (cw) Alexandrite lasers. With lamp pumping, output powers as high as 60 W could be obtained. However, the systems are complex and bulky. Maximum reported slope efficiencies are 1.5 % (optical-to-optical with respect to incident pump power) [99, 114]. On the other hand, single transverse-mode pump sources like dye lasers or Argon ion lasers resulted in more efficient laser operation (up to 64 %) [106, 115]. However, for these cases, the pump source itself is an expensive laser system. Hence, none of these pump sources could provide the advantages of direct diode pumping and cannot compete with the Ti:sapphire lasers in the market.

Alexandrite lasers were first pumped by diodes in 1990, using two 5 mW single-mode diodes around 680.5 nm [119]. The Alexandrite laser output power was less than 1 mW [119]. The same group has then pumped Alexandrite lasers using two 250 mW multimode diodes around 640 nm and obtained 25 mW of cw output power [106]. In a study published in 2005, using a high power (10W) diode array consisting of many single-emitter multimode diodes around 680 nm, cw output powers as high as 1.3 W have been obtained from Alexandrite lasers [120]. However, the transverse intensity profile of the emission from the diode array was quite structured. This resulted in a multimode laser output (M^2 of

2.8) as well as relatively low slope efficiencies. Recently, Damzen et al. obtained cw output powers as high as 6.4 W from an Alexandrite laser system side-pumped by two 29 W diode arrays at 635 nm [121]. In this study, the slope efficiencies remained below 20 %.

In this work, to our knowledge, we present the first demonstration of high-brightness tapered diode lasers (TDL) as pump sources for the Alexandrite gain medium. The TDL provided up to 1 W of output power with a tunable optical spectrum centered around 678.5 nm or 680.4 nm that is suitable for in-line pumping of Alexandrite by populating the R-lines. The diodes possess M^2 values of 1.1 in the fast axis and 5 in the slow axis, and a brightness of about 500 mW/μm^2 which represents a 2-fold improvement compared to the state-of-the-art single-mode and broad-stripe single-emitter diodes in the same wavelength range[80]. While pumping at the 678.5 nm line, using a 0.5% output coupler, we have obtained output powers as high as 168 mW, slope efficiency as high as 38%, and a cw tuning range from 724 nm to 816 nm. The laser output was multimode with M^2 values of 1.25 and 4.5 in the horizontal and vertical axes, respectively. Upon insertion of a slit near the output coupler, we could also obtain a beam profile close to TEM_{00} at an output power of 112 mW. Using Findlay-Clay analysis, the round-trip loss of the cavity was estimated to be around 0.4 %. Caird analysis gave a value of 0.3% for the round-trip loss and 63% for the intrinsic slope efficiency. Lastly, upon pumping at the 680.4 nm line with a stronger absorption, cw output powers as high as 200 mW could be obtained. These results demonstrate the suitability of recently available tapered diode technology as efficient pump sources for Alexandrite lasers. This initial study has the potential to pave the way for the development of low-cost, compact femtosecond Alexandrite lasers near 750 nm as optimal pump sources for multiphoton microscopy.

7.2 Experimental Setup

We start this section with a brief description of the tapered diode (TD) that was employed as a pump source for Alexandrite. Similar TDs have been used to pump Cr:LiCAF and Cr:LiSAF gain media to minimize the complexity in pumping geometry [80]. Similarly, we believe that the TDs which provide the highest brightness output at these wavelengths will considerably simplify the complexity and lower the cost of continuous wave Alexandrite lasers. The TDs used in this study were grown and characterized at the facilities of Ferdinand Braun Institute [122]. The TD has a total cavity length of 2 mm. It consists of a 500 μm long ridge waveguide section and a 1.5 mm long tapered amplifier section with a flared angle of 3°. At the output the TD has an aperture with a width of 80 μm. The front facet and rear facts of the TD have reflectivities of 1% and 94%, respectively. The TD is mounted on standard C-mounts, with p-side down with copper tungsten submounts using AuSn solder. A commercial c-mount diode fixture (ILX LDM-4409) with thermoelectric cooling is used for housing the diode.

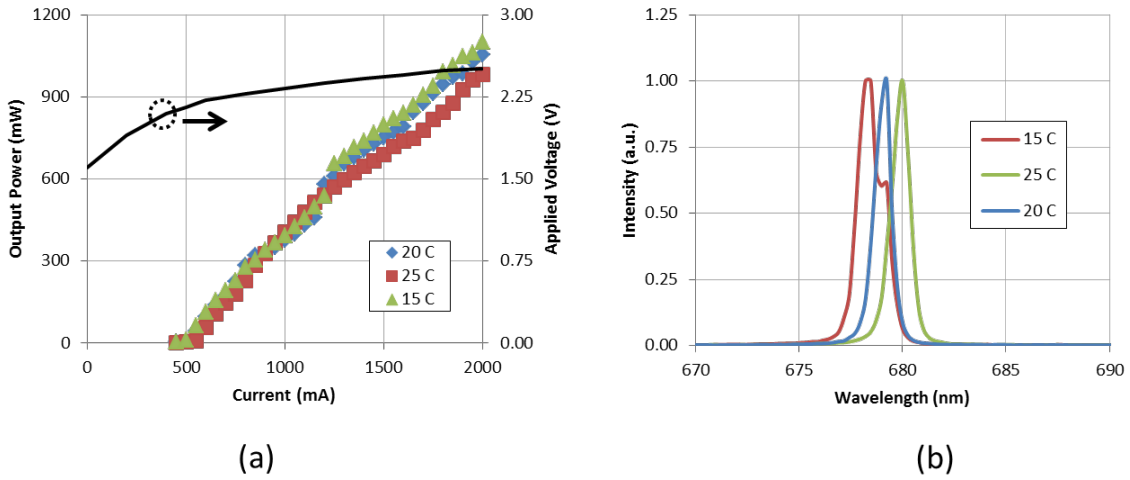

Figure 7.2.1 (a) Measured variation of optical output power with input current for the tapered diode laser at the diode holder temperatures of 15 °C, 20 °C and 25 °C. Corresponding voltage values of the tapered diode for 25 °C operation are also shown. (b) Measured optical spectrum of the tapered diode at 2 A diode current and at the diode holder temperatures of 15 °C, 20 °C and 25 °C. By adjusting diode current and temperature, it is possible to tune the central wavelength of emission to the absorption peaks at 678.5 and 680.4 nm.

Figure 7.2.1 (a) shows the measured variation of the optical output power of the tapered diode with drive current at the diode holder temperatures of 15 °C, 20 °C, and 25 °C. At 15 °C, the TD has a lasing threshold of 500 mA and a slope efficiency of 0.75 W/A. At a drive current of 2 A, the diode provides up to 1100 mW of output power, with a diode voltage of 2.5 V, which corresponds to an electrical-to-optical conversion efficiency of about 22 %. The diode spectrum is centered at 678.5 nm and has a width of about 1.5 nm (FWHM) at 15 °C case temperature and 2 A diode current. We note here that this wavelength directly matches the R_2 line of the Alexandrite crystal. As we can see from Fig. 7.2.1 (b), by increasing the diode case temperature to 25-30 °C it was possible to shift the diode wavelength to the R_1 line of Alexandrite, which actually has a stronger absorption [98] (Fig. 7.1.1 (b)). However, the diode output power is lower for this case (980 mW at 2 A

and 25 °C) due to the increased temperature. In most of our lasing experiments, we have exploited the R_2 line for pumping. For comparison, lasing results obtained while pumping the R_1 transition will be presented in Fig. 7.3.7.

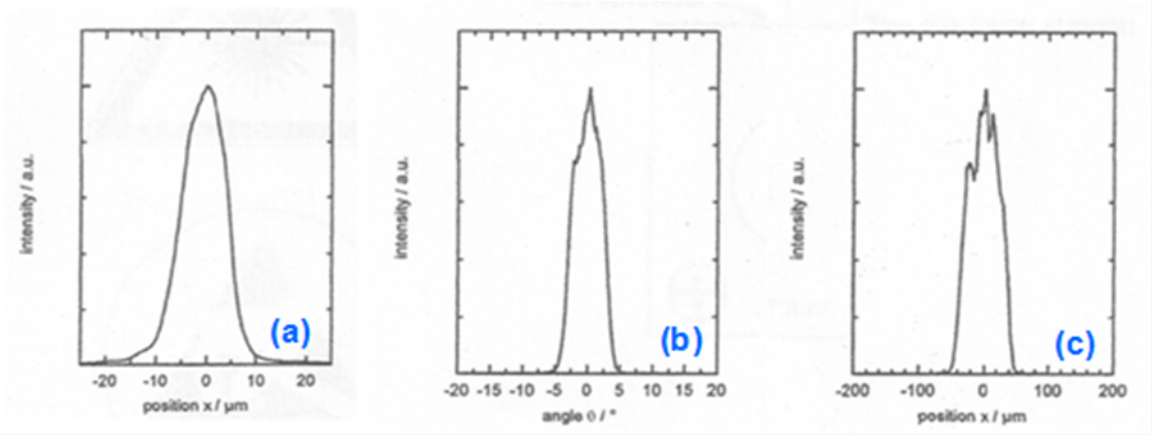

Figure 7.2.2 (a) Beam waist, (b) far field and (c) near field profile for the slow axis of the tapered diode laser (TDL) measured at 1 W of output power and at a cooling temperature of 15 °C.

The method of the moving slit (ISO Standard 11146, Annex A) is applied to measure the beam quality of the tapered diode. The intensity profiles of the beam waist, the intensity distribution along the front facet, and the astigmatism of the diode output are also investigated. During the measurements, the laser spot is magnified by using a telescope with a magnification of about 60. The studies were carried out at a diode output power of 1 W and at the diode holder temperature of 15 °C. The beam waist, far field and near field profiles of the tapered diode laser in the slow axis are shown in Fig. 7.2.2. Around 96% of the emitted power originates from the central lobe of the beam waist. We have found a beam waist of 16.4 µm at the $1/e^2$-level, and a far field angle of 7.5° ($1/e^2$), which leads to a beam propagation ratio of 5 ($1/e^2$). In the fast axis, the beam propagation ratio is determined to be better than 1.1 at the $1/e^2$ level, and the beam divergence was about 30°. The astigmatism of the diode is measured to be 650 µm. Using the above mentioned parameters, the brightness of the laser device is estimated as B = 500 mW/µm^2 which is

about 2 times higher than the commercial single mode diodes and single-emitter devices in the market. However, it is possible to grow tapered diodes with brightness approaching 1000 mW/μm^2 [80, 122]. Hence, the results presented in this study are likely to be improved in the near future by using even higher quality tapered diodes.

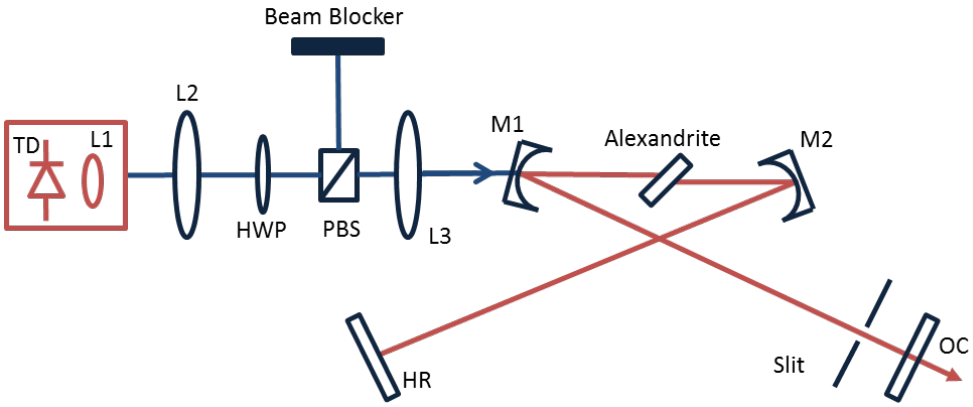

Figure 7.2.3 Schematic of the continuous wave Alexandrite oscillator pumped by a tapered diode laser (TD). M1-M2: Curved pump mirrors with a ROC of 75 mm. OC: Output coupler.L1: Collecting & collimating aspheric lens. L2: Cylindrical collimating lens (matches the divergence in both axes). L3: Focusing lens. HWP: Half-wave plate. PBS: polarizing beam splitter cube.

Figure 7.2.3 shows a schematic of the tapered diode pumped Alexandrite laser. The diode output beam was first collimated with a 4.5 mm focal length aspheric lens with a numerical aperture of 0.54 (L1 in Fig 7.2.3). A cylindrical lens with a focal length of 50 mm (L2, acting on fast axis) matched the diode divergences in both axes to minimize astigmatism. Then the pump beam was focused inside the Alexandrite crystal, using an achromatic doublet with a focal length of 60 mm (L3). A half-wave plate (HWP) and a polarizing beam splitter cube (PBS) were used to adjust the incident pump power on the crystal. Variation of the diode current changes the output wavelength. Therefore, the diode current was kept at 2 A in all the experiments. The incident pump power on the crystal at the maximum drive current was 925 mW (lower than 1.1 W due to the transmission losses of the optics). The cw laser experiments are based on an astigmatically-compensated x-

cavity consisting of two curved mirrors (M1 and M2, ROC = 75 mm), a flat end mirror (HR) and a flat output coupler (OC). The HR mirrors have a reflectivity greater than 99.9% from 725 nm to 925 nm and a pumping window with transmission above 98% in the red spectral region. The length of the long cavity arm was adjusted to 45 cm to obtain a beam waist of approximately 20 μm inside the gain medium. The short arm length was 35 cm long in all the experiments. A Brewster-cut, 10-mm-long, Alexandrite crystal (Northrop Grumman) with a thickness of 3 mm and a width of 5 mm (chromium doping level 0.2%) is used in the study. The crystal absorbs 73% and 95% of the incident TM polarized pump light at 678.5 and 680.4 nm, respectively. The crystal was mounted with indium foil in a copper holder which is temperature stabilized to 25 °C with a circulating water chiller. We note that we have observed a strong tendency of Alexandrite lasers for self-pulsing (also known as self-Q-switching as described in the previous chapter) [123]. Similar phenomena have also been reported in other Cr^{3+}-doped materials such as Cr:LiCAF [123], Cr:LiSAF [5, 63] and Ruby [54-57]. However, it is possible to obtain pure cw operation by fine adjustment of the separation of the curved mirrors.

7.3 Results and Discussion

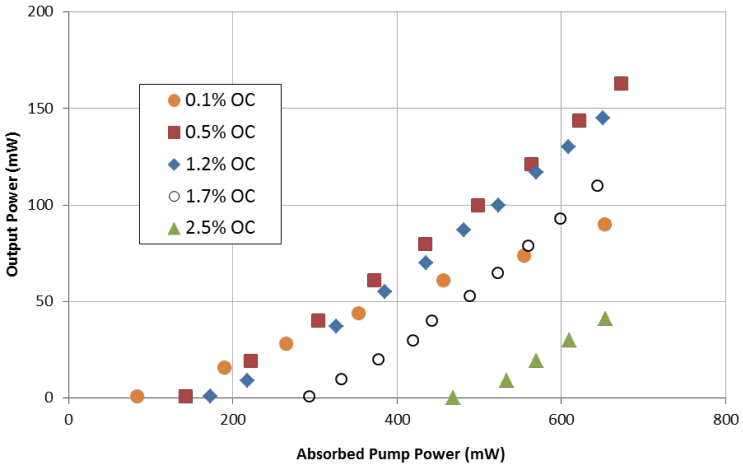

Figure 7.3.1 Measured continuous-wave output power of the tapered diode pumped Alexandrite laser as a function of the absorbed pump power at various levels of output coupling between 0.1% and 2.5%.

Figure 7.3.1 shows the measured efficiency curves of the continuous-wave Alexandrite laser using several different output couplers, with transmission ranging from 0.1% to 2.5 %. The highest power was obtained using a 0.5 % output coupler. With this OC, the laser produced 168 mW at an absorbed pump power level of 670 mW. The free running laser wavelength was 755 nm. The laser slope efficiency was 25 % at low incident power levels and then increased to 38% at higher pump powers (an overall fit gave an average slope efficiency of 31%). This unusual effect is clearly visible in Fig. 7.3.1. We believe that this is possibly due to an improvement in mode-matching between the cavity and pump modes at increased pump power levels. The overall optical-to-optical and electrical-to-optical conversion efficiencies were ~15% (168 mW / 1100 mW) and ~3.4% (168 mW / 5 W), respectively. We note here that while using the 0.5% output coupler, 30 mW of total laser power was found to be leaking from the cavity high reflectors (a total of 5 bounces, 2 bounces from M1, 2 bounces from M2 and one bounce from HR, Fig. 7.2.3). With the 0.5% OC, the estimated intra-cavity power was 32.6 W. This finding shows that the cavity

mirrors have a leakage loss of about 0.1% (30mW/32.6 W), corresponding to a leakage loss level of 0.02% per bounce. Using high reflectors with improved coating, the obtained output power can exceed 200 mW from this configuration.

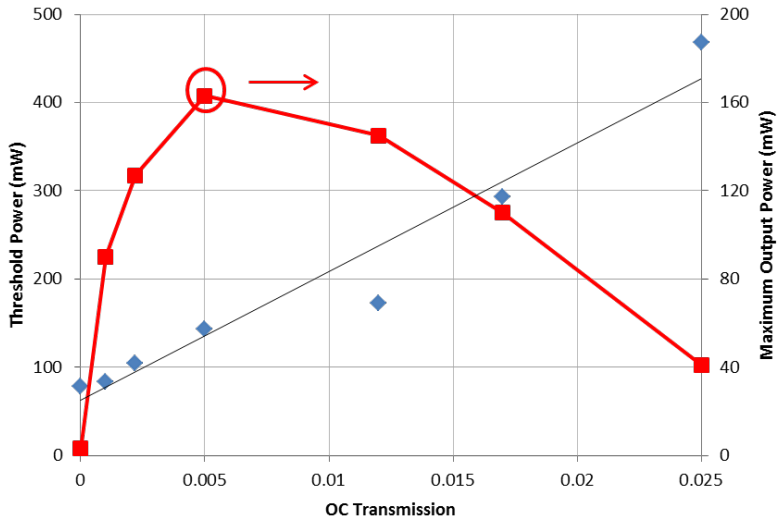

Figure 7.3.2 Measured variation of lasing threshold and maximum obtainable output power as a function of the output coupler transmission.

Figure 7.3.2 demonstrates the measured variation of lasing threshold as a function of the output coupler transmission. Variation of maximum obtainable power with output coupler transmission is also shown in the same graph (at the maximum absorbed pump power of 670 mW). First of all, the optimum output coupling is 0.5-1 %, as a result of the low-gain nature of the material. This fact also underlines the importance of using high quality crystals and mirrors with low passive losses in the resonator to attain high slope efficiencies.

The measured lasing threshold was 143 mW with the 0.5 % output coupler (optimum output coupling, Fig. 7.3.2). A lasing threshold of 83 mW was measured using a 0.1 % output coupler. Moreover, operating a cavity with all high reflective mirrors, a lasing

threshold of 78 mW was achieved. We have determined the best linear fit to the experimental data as P_{th}≈60+148T (in mW units, solid line in Fig. 7.3.2). According to the Findlay-Clay analysis (Eq. 2.3.2), the total round trip cavity loss (L) was estimated to be 0.4± 0.1 %.

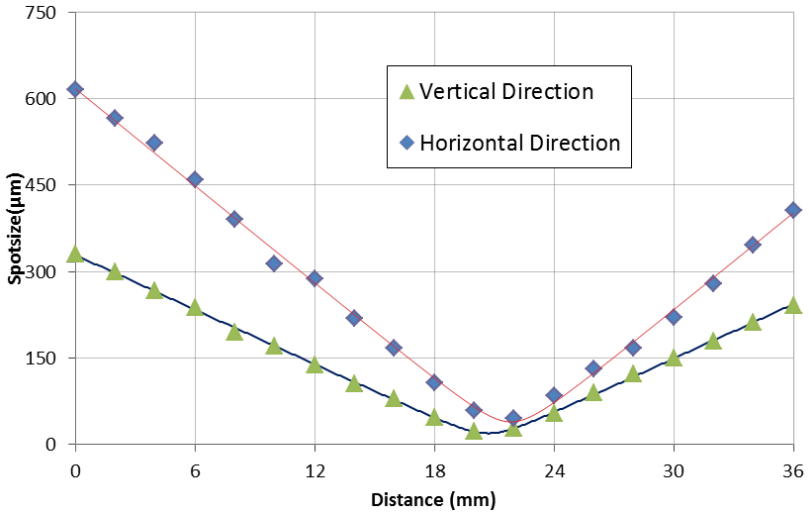

Figure 7.3.3 Measured position dependence of the spot size ($1/e^2$) function from the Alexandrite laser near the focus of a 6 cm lens in the z and y axes.

Due to the multimode nature of the pump beam in the slow axis, the Alexandrite laser output was also multimode in the corresponding axis. Figure 7.3.3 shows the measured position dependence of the spot size function of the Alexandrite laser near the focus of a 6 cm lens. The best fit value for M^2 was determined to be 1.25 and 4.5 in the x and y axes, respectively. We note here that, despite the multimode pump beam, it was possible to push the Alexandrite to operate with a TEM_{00} mode. To this end, we have inserted a circular slit near the output coupler and decreased the aperture size until the laser produced a circular beam profile. The inserted slit generates a high level of losses for the higher-order modes and the laser power predominantly appeared in the fundamental mode (Fig. 7.3.4). However, this has a negative effect on the mode matching between the pump and cavity modes. Hence, with the insertion of the slit, using the 0.5% output coupler, the laser slope

efficiency decreased from 38% to 25% and the obtained output powers decreased from 168 mW to 112 mW.

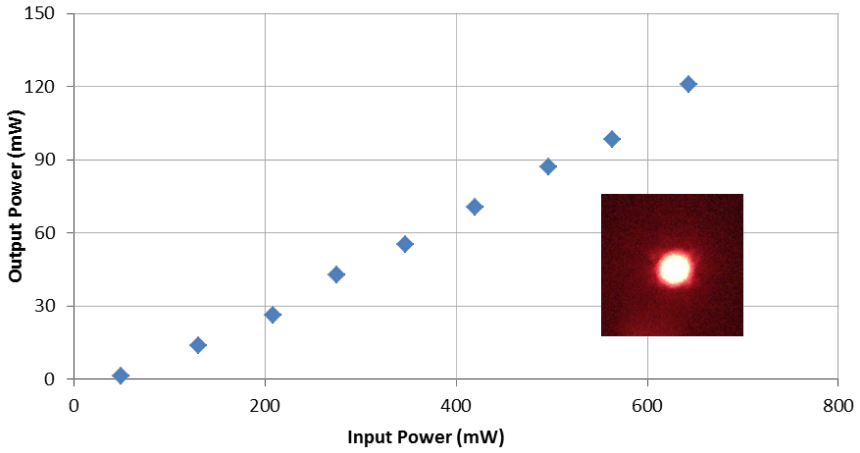

Figure 7.3.4 Continuous-wave output power versus absorbed pump power for the tapered diode pumped Alexandrite laser taken using a 0.5% output coupler and an intracavity slit.

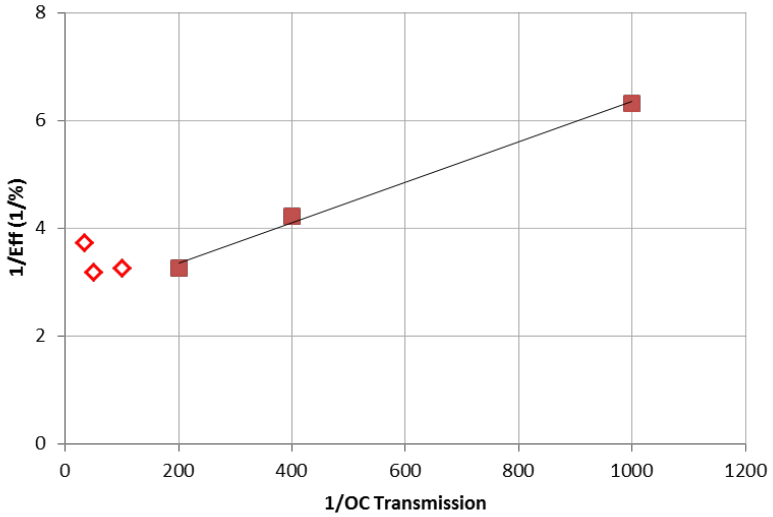

Figure 7.3.5 Measured variation of the inverse of the slope efficiency as a function of the inverse of the output coupling for the tapered diode-pumped Alexandrite laser.

We have also used the measured variation of the slope efficiency with output coupler transmission (Fig. 7.3.5) to estimate the resonator losses at the lasing wavelength (Caird analysis Eq.2.3.1). Least-squares fitting to the experimentally measured data gave best-fit L and η_0 values of (0.3 ± 0.1) % and (63 ± 5) %, respectively. We note here that in the Caird analysis, we have only considered the slope efficiency data taken with 0.1, 0.22 and 0.5% output couplers (filled squares in Fig. 7.3.5) and ignored the data taken with 1.2, 1.7, and 2.5% output couplers (empty squares in Fig. 7.3.5). In conflict with theory, the obtained slope efficiencies at high output coupling would start to decrease. A similar effect is also observed in Cr:colquiriites where it is due to the presence of Auger energy upconversion processes [109]. Here, the decrease in the slope efficiency is a side-effect of increasing lasing threshold due to the decrease in fluorescence lifetime. We suspect that a similar mechanism might also be at work in the Alexandrite gain medium, though this needs further verification.

The cavity loss estimate using Findlay-Clay (0.4 ± 0.1%) and Caird (0.3± 0.1%) analyses are in relatively good agreement with each other. As we have discussed earlier, due to the non-optimum reflectivity bandwidths of the high reflector mirror set that was used in this study, we had about 0.1% leakage loss from the HRs. Other parasitic losses of the HRs are specified to be about 0.005%, so we estimate that an additional loss of 0.05% will be present from all the bounces on the cavity optics (four bounces on curved high reflector mirrors, one bounce on the flat cavity high reflector and the output coupler). The remaining 0.2 % loss should be attributed to the Alexandrite crystal, where in each pass one roughly gets a loss of 0.1%. For the 10-mm-long Alexandrite crystal, this corresponds to a quite low loss level of only about 0.1% per cm, which is similar to what can be achieved with Cr:LiCAF (0.14% per cm [109]) and Cr:LiSAF (0.2 % per cm [124]), and much better than typical Ti:Sapphire crystals (2 % per cm [86]). This also shows itself in the crystal figure of merit (FOM) values, which is defined as the ratio of the absorption coefficient at

the pump wavelength to the absorption coefficient at the lasing wavelength. The Alexandrite crystal that was used in this study has an estimated FOM of about 3000 (≅3/0.001), which is relatively high in comparison with Cr:LiCAF (2150 [109]), Cr:LiSAF (1500 [124]) and Ti:Sapphire (150 [86]). On the other hand Scheps at al. reported a passive loss level of 0.06% per cm from a 0.2% chromium doped Alexandrite crystal (the crystal probably had even lower losses since they assumed that the cavity optics did not contribute to the resonator losses) [106]. Hence, the slope efficiencies that were reported in this study could be further improved by using better quality Alexandrite crystals and cavity optics.

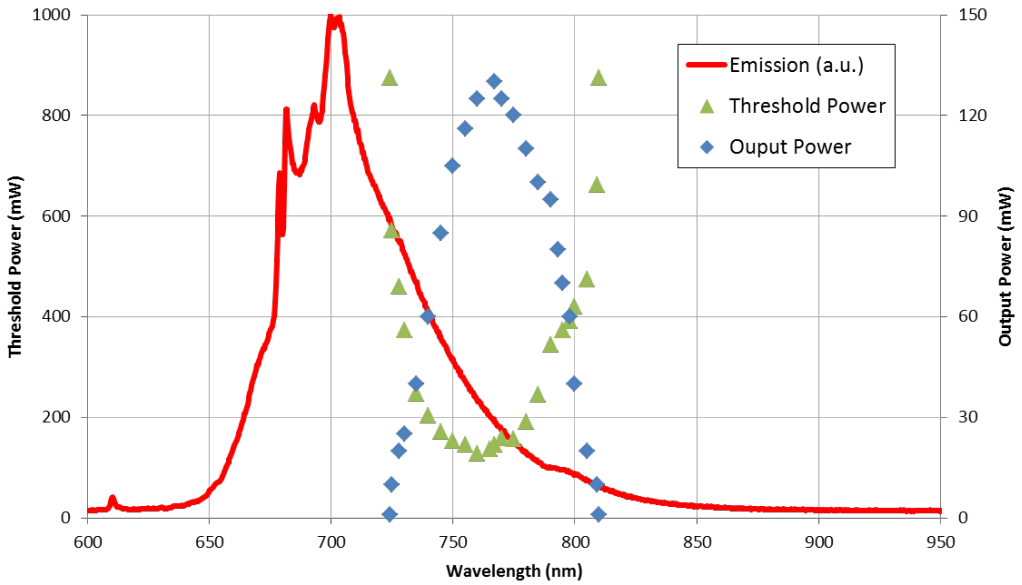

Figure 7.3.6 Continuous-wave tuning curve of the Alexandrite laser taken with the 0.5 % output coupler, at an absorbed pump power of 670 mW. Measured variation of lasing threshold with wavelength and room-temperature emission spectrum (E//b) of the Alexandrite is also shown.

Fig. 7.3.6 shows the measured cw tuning range of the Alexandrite laser using the 0.5% output coupler. For comparison, we have also included the emission spectrum of the

material (note the sharp R lines that were used for pumping). Fig. 7.3.6 also includes the measured variation of lasing threshold with wavelength. The laser wavelength was tuned by (i) inserting an SF11 prism into the HR arm or by (ii) inserting a birefringent tuning plate. Both methods give similar results in terms of tuning range and output power, but the spectra were narrower with the birefringent plate (0.5 nm FWHM). With the 0.5 % output coupler, the Alexandrite laser could be tuned smoothly from 724 nm to 810 nm (86 nm). When we replaced the output coupler with a high reflector, the long wavelength edge could be extended up to 816 nm. We believe tuning below 724 nm was prevented due to the increased passive losses of the cavity high reflectors, which had reflectivity above 99.9% from 725 nm to 925 nm. On the long wavelength side, the mirrors had good reflectivity, but the emission cross section of the material becomes too low to have sufficient gain above 816 nm.

In earlier studies, using flashlamp pumping, Walling et al. demonstrated tuning of a pulsed Alexandrite laser from 701 nm to 818 nm [98]. Pulsed pumping with high lamp energies (100 J) and use of a lower Cr^{3+} doping of the crystal (0.043%) was effective in reaching the short wavelength (701 nm) limit in that study [98]. Later, a tuning range extending up to 858 nm has been reported by Kuper et al. from a flash lamp pumped pulsed Alexandrite laser at elevated temperatures above room temperature [103]. With temperature, the emission profile of the Alexandrite shifts to longer wavelengths and the emission cross section also increases due to the increased role of the storage level [98, 103]. In particular, reaching the 858 nm range required an Alexandrite rod temperature of 513 °C and a pump energy of 105 J [103].

So far, we have presented continuous wave laser results of the Alexandrite laser taken while pumping at the 678.5 nm line. For this case, the incident pump power was 925 mW, the absorption of the Alexandrite crystal was 73% and the total absorbed pump power was 675 mW. As mentioned earlier, by adjusting the diode temperature, it was possible to tune

the tapered diode wavelength to the other R-line (680.5 nm). At this line, the incident pump power on the crystal decreased to 865 mW. However, the crystal absorption climbed to 95%, resulting in an overall absorbed pump power of 820 mW. Therefore, we expect a rise in the obtainable output powers from the Alexandrite crystal. The efficiency curves taken with 0.22%, 0.5% and 1.2% output couplers are shown in Fig. 7.3.7. Using a 0.5% output coupler, we measure output powers as high as 195 mW. The lasing threshold values and the slope efficiencies remained almost the same as those obtained in the case of 678.5 nm pumping.

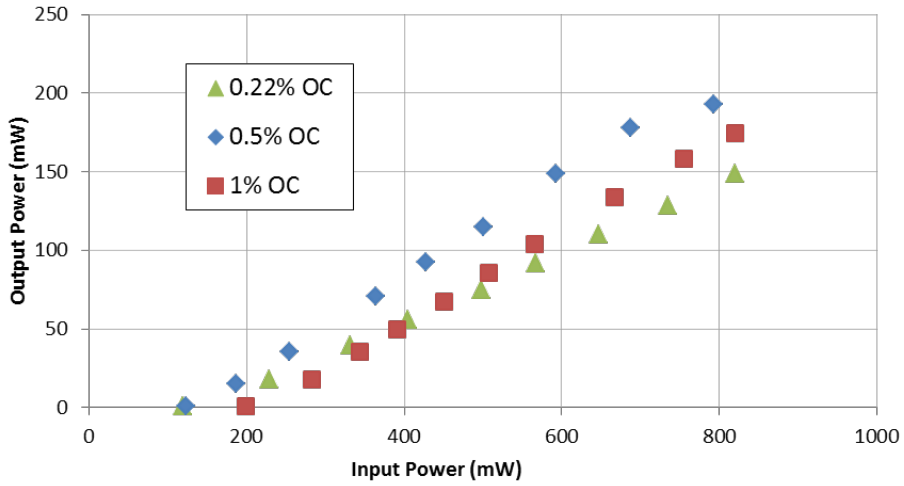

Figure 7.3.7 Measured continuous-wave output power as a function of the absorbed pump power for the tapered diode pumped Alexandrite laser taken at 0.25 %, 0.5 % and 1.2% output coupling. The laser is pumped at the 680.5 nm (R1) line.

7.4 Conclusion

To provide a comparison with earlier work, Table 7.4.1 represents a summary of the published laser results for continuous wave Alexandrite lasers in the literature. Results obtained in this work have also been listed at the end of the table (marked with *). As

mentioned earlier, the broad emission bands of Alexandrite in the visible enables the use of a variety of pump sources including flashlamps [113], Hg & Xe lamps[99, 114, 125], sun light [118] and second harmonic of Nd-based systems [116, 117]. Using these pump sources, tens of watts of continuous wave output power have been obtained from Alexandrite lasers. However, these pump sources are complicated, which limits the usability of Alexandrite lasers. On the other hand, there are only a handful of studies that report diode-pumped cw Alexandrite lasers.

Earlier studies on diode pumping of cw Alexandrite lasers have used low brightness sources that were available at the time, resulting in limited levels of output power [106, 119]. Later studies using high-power diode arrays as pump sources resulted in the generation of cw output powers as high as 1.3 W [120] and 6.4 W [121]. Here we have reported pumping of cw Alexandrite lasers with high-brightness tapered diode lasers for the first time. Moreover, this is probably the first report of pumping Alexandrite via the R_2 transition at 678.5 nm. The obtained slope efficiencies are the highest achieved so far from diode-pumped cw Alexandrite lasers and the obtained output powers (200 mW) are also sufficient for many applications. We also note here that there is a great potential for future improvements by using better quality Alexandrite crystals and cavity optics as well as higher brightness tapered diodes. Our present results clearly show that the recent advances in tapered diode technology are key factors that result in the development of low-cost, compact, and efficient cw Alexandrite lasers with moderate output power levels.

Table 7.4.1 Summary of results from literature obtained for continuous-wave Alexandrite lasers. For comparison, pump source, pump wavelength, pump power, laser power, laser slope efficiency, and laser beam quality have been specified for each case. Results obtained under diode pumping have been listed at the bottom of the table.* Denotes the experimental results obtained in this work.

Pump source	Pump wavelength (nm)	Pump power (W)	Laser power (mW)	Slope efficiency (%)	Laser output (M^2 value)	Year	Ref.
Flashlamp	Broadband	3,000	6,500	0.8	Multimode	80	[113]
Hg Arc lamp	Broadband	6,000	60,000	1.5	Multimode	85	[99, 114]
Xe Arc lamp	Broadband	8,000	20,000	0.5	Multimode	85	[99]
Xe Arc lamp	Broadband	-	2,000	-	TEM00	85	[99]
Krypton laser	647	1.6	600	51	-	83	[115]
Hg Arc lamp	Broadband	8,000	17,000	0.5	-	93	[125]
Dye laser	615	0.3	150	64	-	93	[106]
Sun-light	Broadband	~1000	12,000	1.2	-	99	[118]
SH of Nd:YAG	532	0.215	11	10.5	-	05	[116]
SH of Nd:YVO4	532	5	1,420	36	TEM00	06	[117]
Single mode diode	680.4	2 x 0.005	-	25	-	90	[119]
Multimode diode	640	2x0.25	25	28	-	93	[106]
Multimode diode array	680.4	10	1,300	24	2.8	05	[120]
Multimode diode array	635	2x29	6,400	~15-20	-	13	[121]
Tapered diode	678.5	1	112	25	<1.2	13	*
Tapered diode	678.5	1	168	38	~2.4	13	*
Tapered diode	680.4	1	200	34	~2.4	13	*

Chapter 8

FURTHER STUDIES on the DEVELOPMENT of LOW-THRESHOLD Cr^{3+}-DOPED TUNABLE SOLID-STATE LASERS

In this chapter, some of the collaborative work conducted with other members of the Koç University Laser Research Laboratory will be described briefly. These studies can be considered in the scope of this PhD thesis. In the first section of this chapter, the single-mode diode pumped Alexandrite laser will be introduced. Different from the previous Alexandrite study, in this project temperature dependent performance of the laser system was examined. Next, a single-mode diode pumped efficient and robust Kerr-lens mode-locked (KLM) Cr:LiSAF laser will be presented. In this project, a different output coupler design (Gain Matched Output Coupler) was used to increase the mode locking stability of the laser system. Later, the tapered diode pumping scheme was employed to the Cr:LiSAF laser to improve the mode-locking performance and the obtainable peak powers. In the last section of this chapter, we will briefly describe this project and present the results.

8.1 Alexandrite Laser Pumped by a Single-Mode Laser Diode

The power performance of the Alexandrite laser systems depends on the crystal temperature [126]. At elevated temperatures the operating wavelength and the gain of the system changes accordingly. Unfortunately, this phenomenon cannot be observed with inline excitation technique, which we used in the tapered diode pumped Alexandrite laser because, the absorption band of the system shifts as the temperature of the crystal varies. However, due to the fixed spectrum of the diode, the comparison at different temperatures will not tell any meaningful information about the laser performance. On the other hand,

the Alexandrite crystal also has a broad absorption band around 590 nm (530-650 nm) [113]. Moreover, state-of-art single mode diodes operating at 635 commercially exist in today's market. Hence, the crystal properties and laser performance can be examined by using these diodes. Moreover, the low-threshold operation of this system can be examined effectively with these diodes, because of having diffraction limited beam quality (M^2~1). As a result, in this study we used these didoes as an input source to determine the crystal behavior at different temperatures. In this section, first we introduce the experimental setup and the methods employed in the spectroscopic and laser characterization experiments. Next, we present experimental results on the emission spectrum, fluorescence lifetime and continuous wave laser performance at different temperatures. Finally, we summarize the results and provide a general discussion.

8.1.1 Experimental Setup

In our experiments, an Alexandrite crystal with a Cr^{3+} doping level of 0.2 % was used (Synoptics, Inc.). It is 10 mm long, 5 mm wide and 3 mm thick and Brewster/Brewster cut to minimize reflection losses at the pump and lasing wavelengths. Moreover, it was cut so that, for TM polarized incident light, the direction of the electric field of the electromagnetic wave inside the crystal is parallel to the crystal b axis. It is mounted with a gold foil in a copper holder. The temperature of the copper crystal holder was stabilized by using a controller and can be adjusted in the 25 - 300 ^{o}C range.

Emission spectrum and fluorescence lifetime measurements were carried out using a pulsed green source based on the frequency doubled output of a commercial Nd-vanadate laser at 1064 nm. The pulses had a full-width-half-maximum (FWHM) of around 70 ns. A pulse repetition rate of 250 Hz was used in lifetime and emission spectrum measurements. Pulse energies of around 1 μJ were sufficient to perform the measurements. For each case,

the pump beam was focused at the center of the Alexandrite samples to a spot size of around 30 μm using a converging lens with a focal length of 60 mm. The fluorescence signal was collected with a MgF_2 lens with a focal length of 8 cm at 90° with respect to the direction of the excitation beam. For emission spectrum measurements, we used a commercial spectrometer (Ocean Optics, model USB2000-VIS-NIR) which had a resolution of 1.5 nm and a spectral responsivity covering the range from 350 nm to 1000 nm. The time dependent fluorescence decay signal was measured using a fast (1 GHz) Si detector and recorded with a 500 MHz digital sampling oscilloscope. The temperature dependence of the emission spectrum and the fluorescence decay time were measured for crystal holder temperatures ranging from 25 °C to 300 °C. We note here that due to the relatively high thermal conductivity of the Alexandrite crystal, the calculated temperature difference between the crystal holder and the center of the crystal is at most 2-3 °C. Hence, we assumed that the center temperature of the crystal is nearly equal to the holder temperature.

Figure 8.1.1.1 shows a schematic of the Alexandrite cavity that was used in the continuous-wave (cw) laser experiments. A linearly polarized, 635 nm AlGaInP single-mode diode was used to pump the alexandrite crystal. The SMD temperature was stabilized to 20 °C with a thermoelectric cooler. The SMD provided a maximum output power of 170 mW at a diode drive current of 300 mA. The output of the SMD was first collimated using a plano-concave lens with a focal length of 4.5 mm. An anamorphic prism pair with a magnification of 2 was then used to transform the elliptical output beam to a nearly circular profile. The pump beam was focused inside the alexandrite crystal using an anti-reflection coated achromatic doublet with a focal length of 60 mm (L2). The cavity elements were the same with the ones used in tapered diode pumped experiments. Using the software we developed, arm lengths of 30 cm and 55 cm gave an estimated beam waist of around 20 μm inside the Alexandrite gain medium near the center of the cavity stability region. The laser

performance was investigated in detail by varying the crystal holder temperature and by using output couplers with different transmission. In the cw tuning experiments, a quartz birefringent filter was used to vary the laser output wavelength.

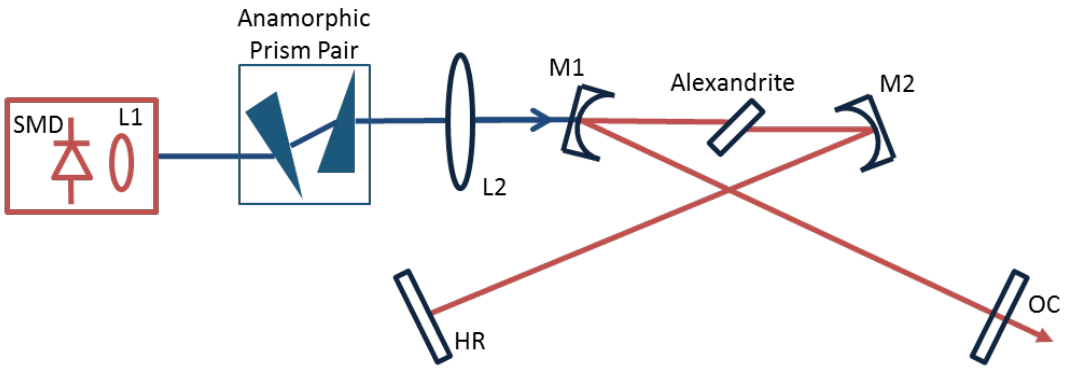

Figure 8.1.1.1 Experimental setup of the single-mode diode pumped continuous-wave Alexandrite laser.

8.1.2 Experimental Results

In the previous chapter, a simplified energy level diagram of the Cr^{3+} ions in the Alexandrite gain medium was given for the E//b orientation (Fig. 7.1.1 (a)). As mentioned in the previous chapter, Alexandrite possesses two strong and broad absorption bands (each with widths of approximately 100 nm) with absorption peaks located near 410 nm and 590 nm [97]. Four-level lasing operation in Alexandrite has been obtained using the transition of excited ions from the $^4T_2$ level to the $^4A_2$ level. So, we will investigate the temperature dependence of the emission spectrum and fluoresce lifetime for the $^4T_2$ and ^2E levels to understand the effects of increased temperature on the cw laser parameters. Here, we note once again that the dynamics of the $^4T_2$ level cannot be separated from that of the metastable ^2E level, which acts as a reservoir of ions for the $^4T_2$ level.

Figure 8.1.2.1 shows the measured variation of the fluorescence lifetime as a function of the crystal temperature for temperatures ranging from 25 °C to 300 °C. We measured the

room temperature (25 °C) fluorescence lifetime of the alexandrite crystal to be 268 µs. Considering the experimental error bars (±5 µs), the measured fluorescence lifetimes can be considered to be in good agreement with the previously reported values in the literature [99]. The lifetime for the sample decreases monotonically, and reaches a value of 55 µs at 300 °C. In this temperature range, a similar decrease in the fluorescence lifetime was also reported in previous studies [99].

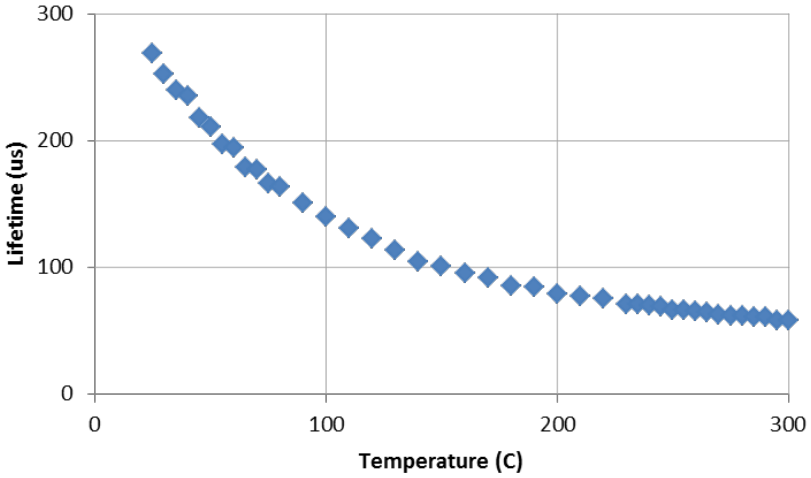

Figure 8.1.2.1 Measured variation of the fluorescence lifetime as a function of the crystal temperature

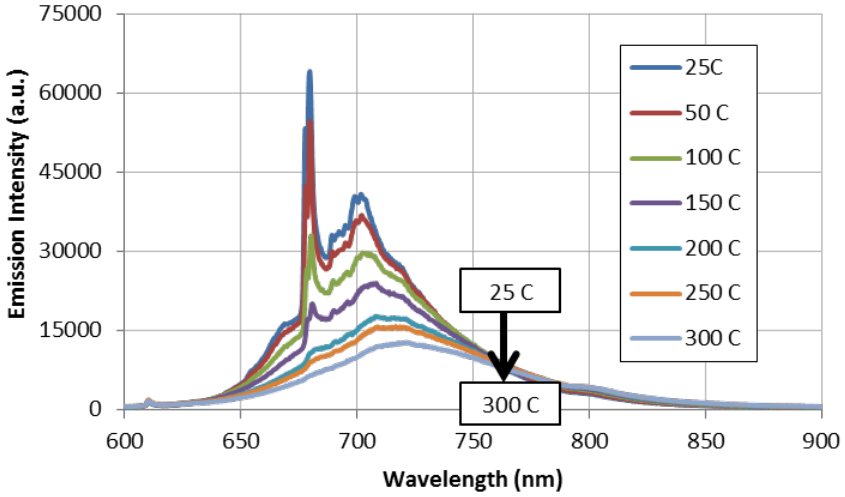

Figure 8.1.2.2 Emission spectra of the alexandrite crystal measured between 25°C and 300°C.

Figure 8.1.2.2 shows the measured variation in the fluorescence spectrum of the Alexandrite crystal around 800 nm, as a function of the crystal temperature, for temperatures ranging from 25 °C to 300°C. We first note that the emission strength (emitted number of photons at each wavelength) decreases as the crystal temperature is increased. This is mainly due to the decrease in the fluorescent lifetime at increased temperatures (the decrease in the fluorescence lifetime is stronger than the increase in the effective emission cross section). Second, the peak emission wavelength for the $^4T_2 \rightarrow {}^4A_2$ transition shifts from around 700 nm at room temperature to around 725 nm at 300 °C. A much slower shift is also observed in the peak wavelength of emission resulting from the transition from the ^2E ($R_{1/2}$) level to the ground state (emission from the R lines) [127, 128]. Moreover, note that, with increasing temperature, the strength of the ^2E emission decreases sharply. For example, in the emission curve taken at 300 °C, we don't even see any structure around 680 nm any more. Basically at these temperatures the effective emission cross section of the $^4T_2$ transition is much higher than the ^2E level due to the increased phonon dynamics at elevated temperatures.

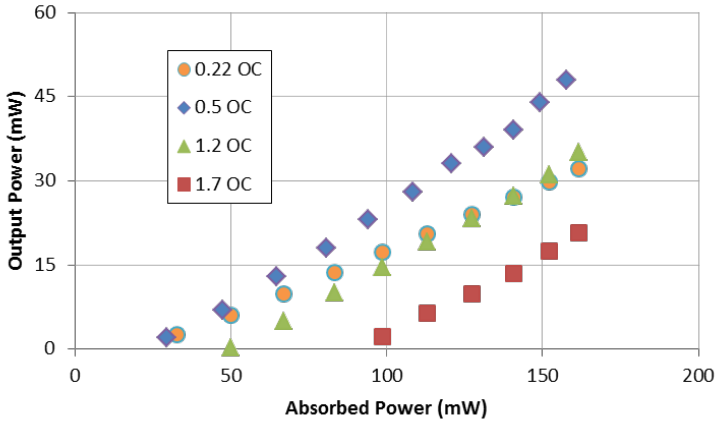

Figure 8.1.2.3 Measured output power variation as a function of the absorbed pump power for the cw alexandrite laser taken with various output couplers (OCs)

Figure 8.1.2.3 shows the measured cw laser efficiency of the Alexandrite laser at room temperature using five different output couplers with transmissions ranging from 0.22% to 1.7%. The free running laser wavelength was around (760 ± 10) nm with all the output couplers. The spectral width (FWHM) of the laser output was around 3 nm. The laser output beam had a TEM_{00} beam profile. Output powers as high as 48 mW and slope efficiencies as high as 36% were obtained using a 0.5% output coupler. The absorbed pump power level was 166 mW, which corresponds to an optical-to-optical conversion efficiency of 29%. The measured lasing threshold was 28 mW. The measured threshold pump power was as low as 13 mW when we replaced the output coupler with a highly reflecting mirror.

Note from Fig. 8.1.2.3 that, the slope efficiencies obtained with 1.2 % (31%) and 1.7% (29%) output couplers are lower than what can be achieved with the 0.5% (36%) output coupler. Similar trends have also been reported in our previous chapter where we discussed cw Alexandrite lasers pumped by tapered diodes at 680 nm [129]. This unexpected decrease of the slope efficiency at increased output coupling values limited the obtained slope efficiencies (36%) and output power levels (48 mW) in our study. A similar effect is also observed in Cr:Colquiriites due to the presence of Auger energy transfer upconversion

(known as ETU) [130]. In the literature, we could not come across previous work that identified ETU as a possible transfer process in Alexandrite. While further detailed investigation is necessary, based on our power efficiency measurements, a likely cause of the abrupt decrease in the laser efficiency with output coupling could be possibly attributed to ETU.

Figure 8.1.2.4 shows the power efficiency curves taken at the crystal temperatures of 25 °C, 100 °C, and 200 °C, by using the 0.5% output coupler. First of all, note that, as the crystal temperature was increased, the lasing threshold values increased dramatically. For example, the lasing threshold increased 3.4 fold, from 28 mW to 95 mW as the Alexandrite crystal temperature increased from 25 °C to 200 °C. This is an expected result and is mostly due to the observed decrease in the fluorescence lifetime (decreases by a factor of 3.3 from 265 μs to 80 μs). Second, we also observed a decrease in the power efficiencies with increasing temperature. For example, the measured laser efficiency decreased from 36 % to 12 % (3 fold decrease), as the Alexandrite crystal temperature increased from 25 °C to 200 °C. The decrease in the slope efficiencies with temperature might be partly due to the increased role of excited state absorption at longer lasing wavelengths [131]. Moreover, there is a slight increase in the quantum defect due to the increase observed in the laser output wavelength from 760 nm to 805 nm. However, this effect will only decrease the efficiencies by about 6%. The observed decrease in the slope efficiencies (3 fold) should be attributed to the increased role of additional loss mechanisms such as excited state absorption at longer wavelengths.

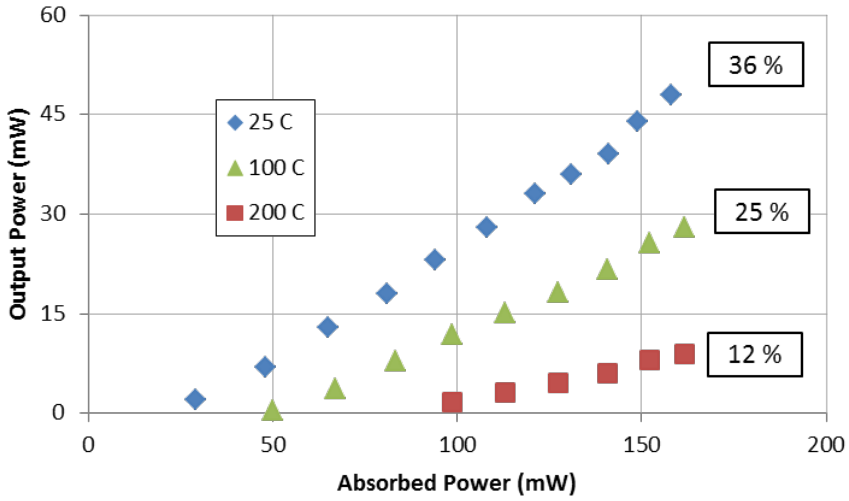

Figure 8.1.2.4 Power efficiency curves measured at 25°C, 100 °C, and 200 °C using the 0.5% transmitting output coupler showed a monotonic decrease in the slope efficiency with increasing temperature.

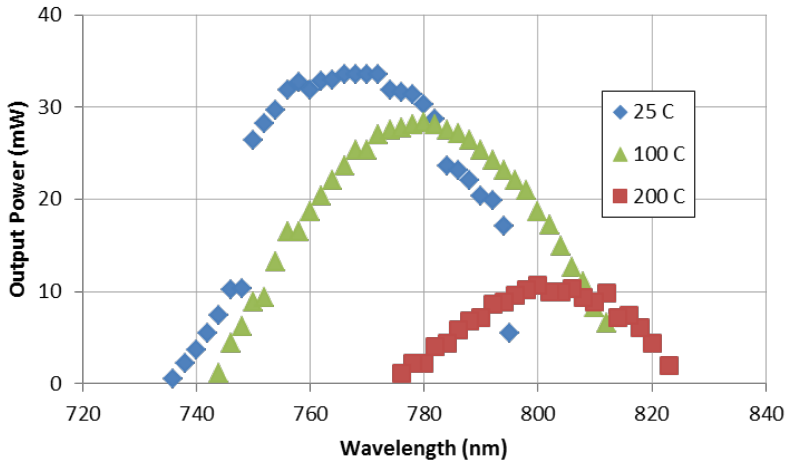

Figure 8.1.2.5 Continuous-wave tuning curves of the alexandrite laser taken at the crystal temperatures of 25°C, 100°C, and 200°C by using the 0.5% output coupler. The pump power was 170 mW.

We have also investigated the cw tuning capability of the single-mode diode pumped Alexandrite laser. Figure 8.1.2.5 shows the variation of the laser output power with output wavelength measured by using the 0.5 % output coupler, at an incident pump power of 170

mW. The data were taken at three different crystal temperatures to observe the effect of temperature increase on the wavelength tuning capability. The obtained output powers are slightly lower (for example, at the peak wavelength of 760 at 25 °C, the output power decreased from 48 mW to 34 mW), due the insertion of the birefringent tuning plate that introduced some unwanted losses. At room temperature, we could smoothly tune our cw laser wavelength from 736 nm to 795 nm. Note that, tuning on the short wavelength side was limited by the reflectivity bandwidth of the cavity high reflectors whose transmission increased below 750 nm (for example, the transmission was about 0.1% at 735 nm). Earlier studies reported tuning down to 701 nm in a pulsed high energy Alexandrite laser [98]. More studies are required with broader bandwidth high reflectors to investigate the cw tuning limit of Alexandrite on the short wavelength side. We also note here that increased role of excited state absorption and self-absorption losses are also a limiting factor on the short wavelength end [108].

On the long wavelength side, the tuning limit was 795 nm at room temperature. An upper limit of 816 nm was reported earlier for the cw tuning from a cw Alexandrite laser operated at room temperature [129]. We believe that the limited pump power available in our study could be one of the factors in the observed decrease in the overall tuning range. On the other hand, we have seen that, by increasing the Alexandrite crystal temperature, the long wavelength tuning limit can be shifted up to 823 nm. Earlier, a tuning range extending up to 858 nm wasreported by Kuper et al. from a pulsed Alexandrite laser at a crystal temperature of 513 °C [103].

8.1.3 Conclusions and Summary

In this study, we investigated in detail the continuous-wave and self-Q-switched operation of a low-threshold and efficient Alexandrite laser system. The Alexandrite laser

was pumped by one single-mode diode providing up to 170 mW of pump power at 635 nm. Laser output powers as high as 48 mW, laser slope efficiencies of 36%, lasing thresholds as low as 13 mW were demonstrated during cw operation. The cw laser output wavelength could be tuned from 736 nm to 795 nm at room temperature, and from 776 nm to 823 nm at 200 °C. We believe that this compact, low-cost and efficient Alexandrite laser has the potential to become an attractive source of 800-nm radiation for several applications.

8.2 Single-Mode Diode Pumped Mode-Locked Cr:LiSAF Laser

The Kerr effect is the intensity-dependent response of the material to light. At high intensities the refractive index can be considered as a summation of the linear (n) and nonlinear (n_2) contributions (i.e $n(I) = n + n_2 I$ where I is the intensity of the light) due to the presence of third-order nonlinear light-matter interactions. Hence, a laser beam may undergo focusing or defocusing due to the Kerr-effect while passing through the gain medium. Inside a solid-state laser, when the intra-cavity laser beam is further focused, it will be occupy a smaller volume inside the gain medium and could overlap better with the pump beam. (Of course, initially the pump spotsize should be smaller than the laser spotsize inside the medium) Since an intense laser beam will experience higher gain, the presence of the Kerr effect will favor the operation of the laser in the mode-locked regime where higher intensities are available.

Mode-locking with Kerr nonlinearity (Kerr-lens mode-locking, KLM) is a very well-known and successful technique that is widely used for generation of ultrashort pulses from broadband gain media such as Ti:Sapphire [84, 132], Cr:ZnSe [133], Cr:Forsterite [134], Cr:LiSAF [135], Cr:LiCAF [136] and others. KLM generates an artificial saturable absorber with an instantaneous lensing effect that shortens the circulating intracavity pulsewidth via self-amplitude modulation (SAM). Hence, unlike saturable Bragg reflectors, KLM does not impose any bandwidth limitation effect and the obtainable pulsewidths are

limited only by the gain bandwidth of the lasing material and dispersion bandwidth of the laser cavity. However, to achieve the shortest pulses: (i) flat dispersion profile over the whole gain bandwidth should be utilized, and (ii) strong gain filtering effect of the active medium should be overcome. To fulfill the second requirement a large SAM is desired, which necessitates use of low output coupling, high pump powers and critical cavity alignment, and operation near the edge of the stability range. These result in low laser beam quality, low laser efficiency, high mode locking threshold, low laser stability and problems in long-term operation. These issues are even more significant in gain media with a low nonlinear refractive index (n_2) such as Cr:LiSAF (0.8 $x10^{-16}$ cm^2/W, which is four times lower than Ti:Sapphire [101]). Even though pulses as short as 10 fs have been demonstrated from low-cost diode-pumped Cr:LiSAF lasers [135], the technology could not go beyond research laboratory demonstration.

To overcome the above mentioned limitations imposed by KLM, the gain filtering effect should be minimized. In that respect, recently Chen et al. suggested the use of gain matched output couplers with a transmission profile that matches the gain profile of the laser active medium[137]. This creates a loss profile that has the same shape as the cavity gain, which results in a broadband flat net gain profile (the gain matched output couplers is also named as inverse gain output couplers (IGOC)). Then this minimizes the need to generate strong SAM, and an arbitrarily low KLM action (nonlinearity) is sufficient for sustaining ultrashort pulses. By employing a 4% IGOC in a Ti:Sapphire laser, Chen et al. demonstrated robust mode-locking at greatly-reduced Kerr nonlinearity requirements [137], and the laser produced sub-8-fs pulses with excellent beam quality.

In this study, we demonstrated long–term stable and robust KLM operation of a diode-pumped, low-cost Cr:LiSAF laser with a gain matched output coupler. The laser is pumped by a single-spatial-mode diode with 125 mW of diffraction-limited output power around 660 nm. A 0.7% IGOC has been used as the output coupler. In this section, first we

introduce the experimental setup. Next, we present experimental results on KLM performance of the laser. Finally, we summarize the results and provide a general discussion.

8.2.1 Experimental Setup

Figure 8.2.1.1 shows a schematic of the KLM Cr:LiSAF laser. The pump diode beam was first collimated with a 4.5 mm focal length aspheric lens (L1), and then focused into the Cr:LiSAF crystal using a 60 mm focal length achromatic doublet (L2). The Cr:LiSAF crystal was 1.5% Cr-doped, had a length of 6 mm and absorbed around 98% of the incident pump power. The Cr:LiSAF laser cavity consisted of two curved mirrors with a radius of curvature of 75 mm (M1, M2), one flat high reflector (HR), two fused silica prism pair (FS) and the GMOC mirror. The GMOC had a transmission of around 0.7% around the gain peak and the spectral transmission profile of the GMOC matched quite well to the gain profile of Cr:LiSAF (Fig. 8.2.1.2). The curved pump mirrors and the cavity high reflector were custom-made double-chirped mirrors (M1, M2, and HR) with transmission above 98% from 625 nm to 685 nm to transmit the pump beam. Their reflectivity was above 99.9% from 790 nm to 940 nm and provided around -80±10 fs^2 of group delay dispersion (GDD) per bounce in the 780-950 nm wavelength range. A fused silica prism pair with a separation of 30 cm was also used to fine tune the net cavity dispersion.

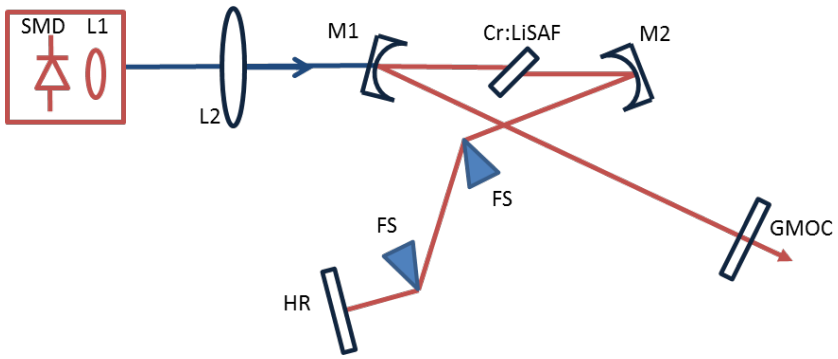

Figure 8.2.1.1 Schematic of the single-mode diode (SMD) pumped Kerr-lens mode-locked Cr:LiSAF laser with a gain matched output coupler.

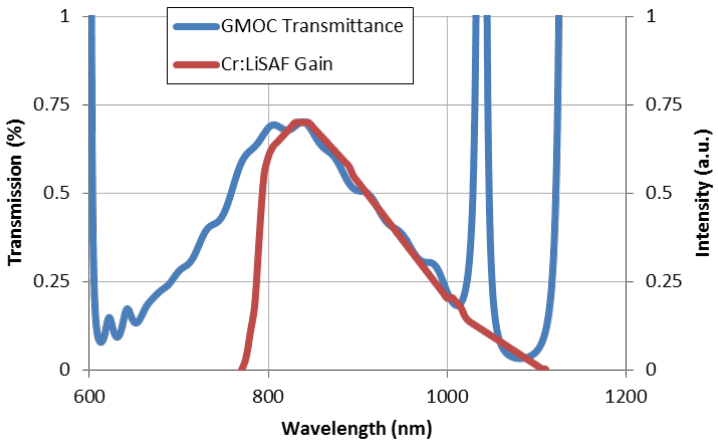

Figure 8.2.1.2 Gain profile of Cr:LiSAF crystal and the designed transmission of the gain matched output coupler.

8.2.2 Results and Discussion

Fig. 8.2.2.1 shows the measured variation of the Cr:LiSAF laser output power with incident pump power. The cw lasing threshold is around 15 mW, and the laser operates in only pure cw regime for pump powers up to around 40 mW. The slope efficiency in the cw

regime is around 35%. For pump powers above 50 mW, it was possible to initiate mode-locked operation by slightly translating one of the cavity mirrors.

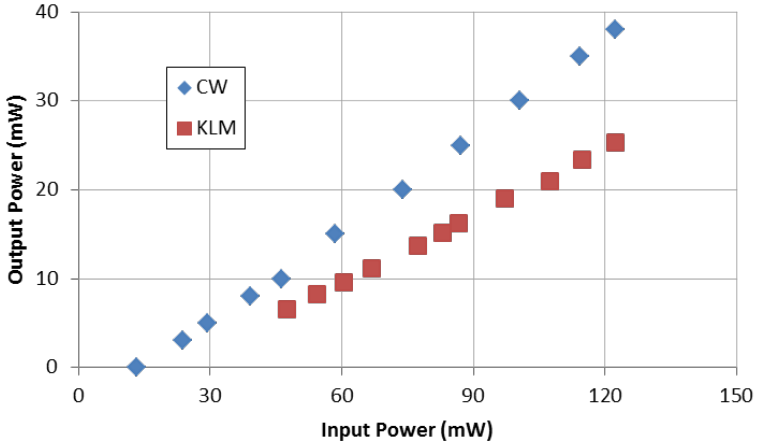

Figure 8.2.2.1 Measured variation of theCr:LiSAF laser output power as a function of incident pump power at CW and KLM regimes.

The optical spectrum extends from 750 nm to 980 nm (Fig. 8.2.2.2 (a)), and is broad enough to support 11.8-fs pulses (calculated transform-limited pulsewidth). The minimum achievable time bandwidth product for this spectral shape is calculated to be 0.45. We have also calculated the autocorrelation deconvolution factor for this spectrum as 1.78. With these parameters, the measured pulsewidth was 13-fs (Fig.8.2.2.2 (b)) and the pulses were slightly chirped with a time-bandwidth product of 0.5. The average power of the pulses was measured as 25 mW at the incident pump power of 120 mW. This corresponds to pulse energy of 200 pJ for the 126 MHz cavity. The peak power of the pulses was as high as 15 kW. The corresponding optical-to-optical and electrical-to-optical conversion efficiencies of the system were 21% and 7%, respectively.

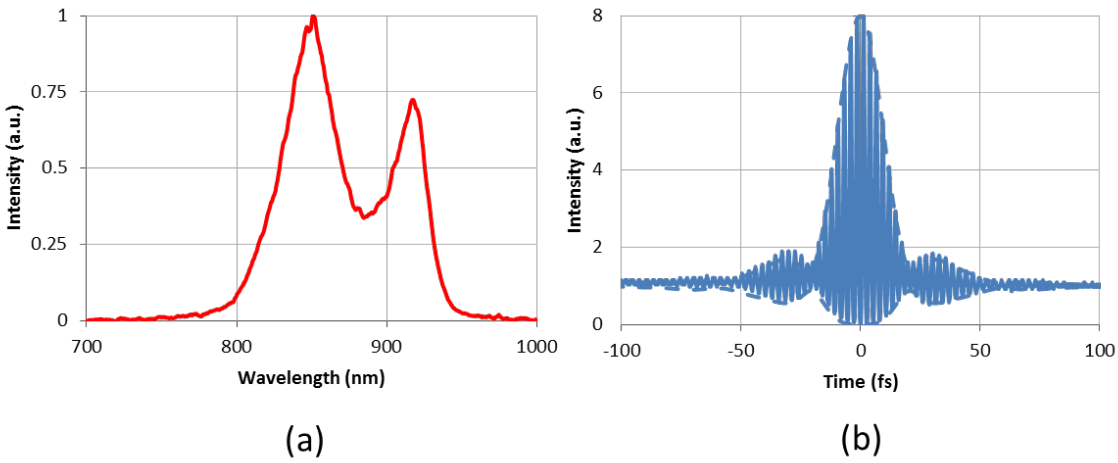

Figure 8.2.2.2 (a) Measured optical spectrum (b) interferometric autocorrelation of the generated pulses

8.2.3 Conclusion

In conclusion, we have employed a gain-matched output coupler to demonstrate robust and efficient KLM operation of a diode-pumped, low-cost Cr:LiSAF laser with long-term stability. An electrical-to-optical conversion efficiency of around 7% was attained, which is around two orders of magnitude better than what is achievable with today's commercial Ti:Sapphire systems. We believe that, with future progress, low-cost, compact and efficient KLM Cr:LiSAF lasers with GMOC technology have the potential to serve as attractive laser sources for many scientific and technological applications.

8.3 Tapered Diode Pumped Mode-Locked Cr:LiSAF Laser

In this study, we applied the tapered diode pumping scheme to the mode-locked Cr:LiSAF laser system described in the previous section to improve laser performance in terms of peak power and pulse energy. First, we briefly describe the experimental setup.

Then, we present the results obtained from the laser and finally we summarize our results and finish the section with a general discussion.

8.3.1 Experimental Setup

Fig. 8.3.1.1shows the schematic of the tapered diode (TD) pumped Cr.LiSAF laser. The TD and correction/focusing elements are the same as those we used in the TD pumped continuous wave Alexandrite system. Similarly, an astigmatically compensated, x-folded laser cavity was employed in the tapered diode pumped mode-locked Cr:LiSAF laser experiment. The resonator had two curved pump mirrors (M1 and M2, R=75 mm), with a reflectivity above 99.9% from 790 nm to 940 nm and a transmission above 98% from 625 nm to 685 nm to transmit the pump beams. Dispersion compensation was employed by using double-chirped mirrors (HR1, HR2) and/or fused silica prism pairs. Two different dispersive mirrors were available during the experiments with group delay dispersion of -80±20 fs^2 (780-950 nm, HR1) and -40±20 fs^2 (750-920 nm, HR2) per bounce. A fused silica prism pair separation of 45 cm was used for dispersion compensation. The gain medium was the same we used in SMD pumped system and was mounted with indium foil in a copper holder. The crystal absorbed about 93% of the incident TM polarized pump light at 680 nm. The crystal holder temperature was controlled with circulating water from a chiller. In this system, the low transmission of the GMOC mirror limited the obtainable output pulse energies due to intracavity nonlinearities. Hence, a double bounce configuration on the GMOC mirror was used to increase the total output coupling to 1.4 % level, which enabled us to reach higher pulse energies from this system.

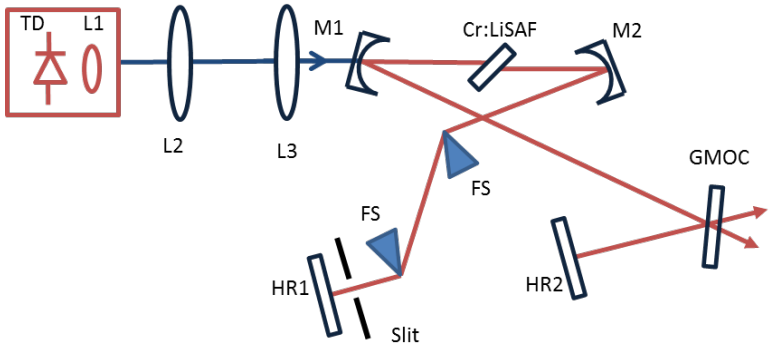

Figure 8.3.1.1 Schematic of the tapered diode (TDL) pumped Kerr-lens mode-locked Cr:LiSAF lasers.

8.3.2 Results

Due to TD's higher brightness and higher average powers, the TD pumped system enabled us to investigate the power scalability of ultrashort pulse Cr:LiSAF laser. Figure 8.3.2.1 shows the measured variation of the Cr:LiSAF laser output power as a function of the incident pump power. All the data were taken by using the GMOC. Data with the square markers were taken near the center of the outer stability range, where the continuous-wave (cw) laser power was optimized (CW optimum in Fig. 8.3.2.1). For this case, the measured cw lasing threshold and laser slope efficiency were 160 mW and 34%, respectively. The laser produced a total of 232 mW of cw output power around 850 nm from its two outputs (116 mW from each), at an absorbed pump power of 875 mW. To minimize thermal effects, the crystal holder temperature was kept at 15 °C during these measurements.

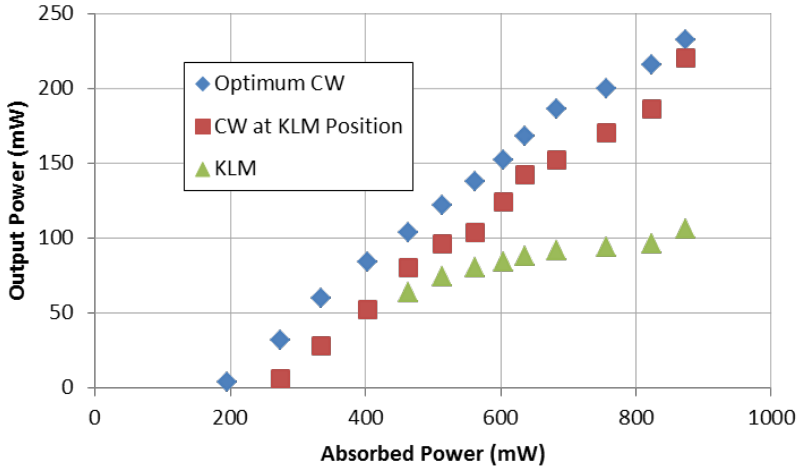

Figure 8.3.2.1 Measured variation of the Cr:LiSAF laser output power as a function of the absorbed pump power.

Lasing thresholds as low as 45 mW and slope efficiencies as high as 47% have been reported earlier, in a TDL pumped cw Cr:LiSAF laser using a 0.5% output coupler [80]. The modest performance we have observed here is partly due to the use of dispersion optimized broadband DCM pairs, which had higher passive losses than cw laser optimized high reflectors. Moreover, the insertion loss of the fused silica prism pair might have contributed to the observed decrease in the cw laser performance. Lastly, the effective output coupling in our case was 1.5 % (two bounces on the GMOC), which is slightly above the optimum output coupling value. For example, it is well-known that, increased role of Auger transfer up-conversion process, increases the thermal effects and limits the obtainable power levels at high output coupling [80]. One should note that, there is an optimum output coupling value for fs Cr:LiSAF oscillators (that also depend on available pump power levels). Use of an output coupling higher than the optimum, limits the obtainable average power levels due to thermal effects. On the opposite side, if one uses too low output coupling, the intracavity nonlinearities limit the obtainable peak power levels.

Data shown with the red square markers in Fig. 8.3.2.1 summarize the measured cw performance at the KLM operation point. Note that obtained cw powers decrease only slightly, from 232 mW to 220 mW, at the KLM position, indicating similarly good mode-matching conditions. KLM operation could be initiated by slightly translating one of the cavity mirrors. Once mode-locked, the laser stayed in the mode-locked regime for hours. 106 mW of mode-locked average power could be obtained from this system.

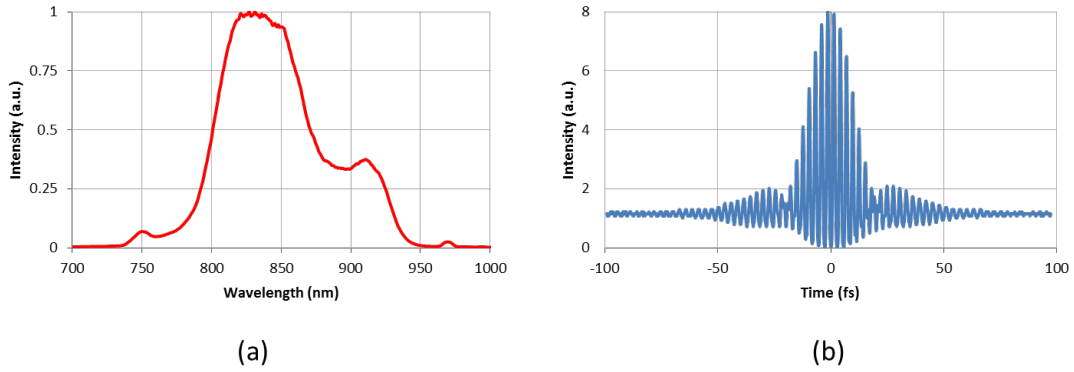

Figure 8.3.2.2 Measured (a) optical spectrum, (b) interferometric autocorrelation

Figure 8.3.2.2 summarizes the properties of the shortest pulses obtained from the TDL pumped Cr:LiSAF laser. The optical spectrum extends from 740 nm to 950 nm and is broad enough to support 12.5-fs pulses (calculated transform-limited pulsewidth). The minimum achievable time bandwidth product and autocorrelation deconvolution factor for this spectral shape is calculated to be 0.36 and 1.3, respectively. With these parameters, the measured pulsewidth was 14.5-fs and the pulses were slightly chirped with a time-bandwidth product of 0.42. The average power of the pulses was measured as 106 mW at an absorbed pump power of 850 mW. This corresponds to a pulse energy of 940 pJ for the 113 MHz cavity. The peak power of the pulses was as high as 60 kW. These, we believe, are the highest peak powers directly obtained from any diode pumped Cr:LiSAF oscillator to date. The corresponding optical-to-optical conversion efficiency of the system was 11%.

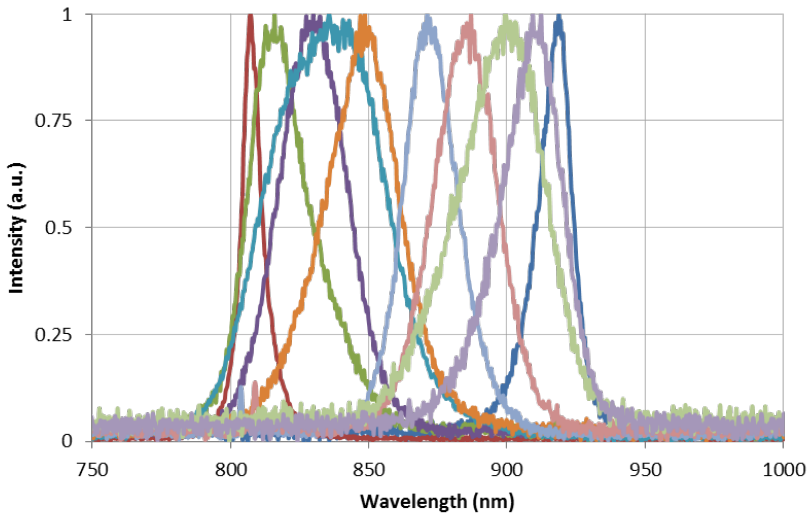

Figure 8.3.2.3 Typical spectra from the Cr:LiSAF laser showing tunability of central the wavelength from 807 nm to 919 nm (112 nm bandwidth), for sub-50-fs pulses

As we have mentioned earlier, broad tunability in the mode-locked regime is quite important for applications such as multiphoton microscopy, time-resolved photoluminescence, or pump–probe spectroscopy. In that respect, we have also investigated tuning capability of our KLM Cr:LiSAF laser in the fs regime. Tuning of the central wavelength of the optical spectra was achieved by using an adjustable slit after the fused silica prism pair (Fig. 8.3.1.1). For each central wavelength, we have optimized the dispersion of the cavity, for the generation of the shortest pulses. In that way, continuous tuning of the center wavelength of the spectra from 807 nm to 919 nm was achieved. Figure 8.3.2.3 shows typical spectra obtained in the tuning range. Femtosecond tuning ranges of 835–910 nm [138] and 809–910nm [139] have been demonstrated from KLM Cr:LiSAF lasers earlier. A broadband SBR has also been employed to obtain fs tuning in the 800-905 nm range, from an SBR mode-locked Cr:LiSAF laser. The tuning range obtained in this study slightly extends the earlier results into the infrared region [140]. We

believe that, a dispersion optimized Cr:LiSAF cavity employing a GMOC, could potentially extend the fs tuning range to above 1000 nm in future studies.

8.3.3 Conclusions and Summary

To summarize, we have developed a low cost and efficient Kerr-lens mode-locked Cr:LiSAF laser systems by using a gain-matched output coupler. The laser is pumped by 1-W tapered diode lasers around 680 nm. Use of the GMOC mirror enabled long-term stable and robust KLM operation. Pulse-widths as low as 14.5-fs, peak powers as high as 60 kW and optical-to-optical conversion efficiencies as high as 11%, and a fs tuning range extending from 807 nm to 919 nm have been demonstrated. To our knowledge, these are the highest peak powers as well as the broadest fs tuning range demonstrated from Cr:LiSAF laser oscillators to date. We believe that, the obtained results clearly demonstrates the usefulness of GMOC mirrors in reducing the requirements of Kerr lens mode locking even in gain media with a low n_2 like Cr:LiSAF, resulting in significant improvement in long-term stability as well as the efficiency of the laser. Demonstrated pulsewidths and fs tuning ranges in this study were limited by the reflectivity and dispersion bandwidth of the available optics. In future studies, KLM Cr:LiSAF lasers based on GMOC technology have the potential to generate pulsewidths down to 7-fs, fs tuning ranges covering the 800-1000 nm region, and peak powers exceeding 100 kW level.

Chapter 9

CONCLUSIONS

In this thesis, we have developed energy efficient low-cost tunable solid-state laser systems in different wavelength bands and operating regimes. Employing low-cost laser diodes, the cost of the lasers is greatly reduced. Designing resonators that enable laser operations with low threshold pump power, increase the efficiency of the lasers.

Determination of the optimum cavity parameters is hard and a bit challenging. To overcome these difficulties we have developed a comprehensive computer program that simplifies the design of the resonators in an efficient way.

Then, we apply these techniques, at first, to the Tm:YAG and Tm:LuAG lasers. In those systems we used two low-cost single-mode laser diodes operating at 785 nm as pump sources. In the experiments, continuous-wave and Q-switched mode-locking regimes are examined. In the continuous wave experiments, the slope efficiencies are very close to the theoretical limits. In particular, from Tm:YAG systems we have obtained 29 mW output power with 22% slope efficiency. The limit for the slope efficiency of this system is 24%. Also from this system as low as 25 mW lasing threshold was obtained. From Tm:LuAG system, similarly, we have obtained 23 mW output power with 19% slope efficiency where the limit of this system was 22%. Moreover, by inserting a birefringent tuning plate into the systems a smooth tuning between 1935-2035 nm and 1945-2045 nm were obtained from Tm:YAG and Tm:LuAG lasers, respectively. In the Q-switched mode-locking experiments we inserted a transmissive SESAM into the cavities and obtained Q-switched mode-locked pulses. The average powers of these systems are around 20 mW. The Q-switched mode-locked pulses carry more than 250 pJ pulse energies at a 170 MHz repetition rate.

Next, we characterize the self-pulsing properties of Cr:LiCAF lasers operating at 795 nm. In this experiment, we used one single-mode low-cost laser diodes operating at 660 nm. In this study, by carefully arranging curved mirror separations, we obtained Q-switched pulses at kHz level repetition rates. In particular, we have obtained 4 microsecond long pulses at a repetition rate 24 kHz. The average output power of the pulses was 40 mW corresponding to 1.6 μJ pulse energy and 400 mW peak power. From that configuration, 10 nm spectral broadening centered around 790 nm was obtained. Furthermore, we estimate the modulation depth of the self-pulsing mechanism 0.5%.

Moreover, Alexandrite laser was pumped with a recently developed high-brightness tapered diode. The tapered diodes can provide up to 1 W output power around 680 nm. From this system we have obtained 200 mW output powers near 755 nm. The intrinsic slope efficiency of this system was 63% where the theoretical limit of this value was 65%.

In the last part of this thesis, we briefly described some of the further improvements of Cr^{3+} doped laser systems using the low-threshold and low-cost diode pump methods. In those experiments, Alexandrite laser is pumped with low-cost single-mode diodes at 635 nm and its low-threshold and temperature dependent characterization are studied. In this system, as low as 13 mW lasing threshold is obtained. By changing temperature from room-temperature up to 200 ^{o}C, the laser tuning was obtained between 723-823 nm. Furthermore, Kerr-lens mode-locked Cr:LiSAF lasers pumped by single-mode and tapered diodes were investigated. From single-mode pumping system as short as 13 fs pulses with 200 pJ pulse energies were obtained. From tapered diode system, the pulse durations are 14.5 fs long and each pulse carries 940 pJ energy. By inserting an extra slit into the tapered diode pumped Cr:LiSAF system, femtosecond tuning was obtained in the 807-919 nm range.

All of these studies clearly demonstrate that the low-threshold cavity design technique is very effective way of obtaining low-cost tunable solid-state lasers operating in the 700-

2100 nm wavelength region. The lasers developed in these projects have a great potential to integrate numerous applications in the biomedical, material processing, range finding and spectroscopy fields.

Appendix A: ERSEN'S ABCD

The software we developed in this thesis to estimate optimum laser configuration is described in chapter 3. Here we will provide the MATLAB code of the program and simple use of it by solving standard four mirror cavity example described in section 3.1.

The MATLAB code for this program as follows:

```
1  - function []=ersensabcd()
2  -
3  - global Cavity;Cavity=[];
4  - global Cavity2;Cavity2=[];
5  - global numElements;numElements=0;
6  - global numElements2;numElements2=0;
7  - global scsize;scsize=get(0,'ScreenSize');
8  - global names;names={};
9  - global fm;fm=1;
10 - global cm;cm=1;
11 - global Xtal;Xtal=1;
12 - global A; A=0.05;
13 - global B; B=1;
14 - global h;
15 -
16 - h.fig=figure('Position',[scsize(3)*0.005 scsize(4)*0.05 scsize(3)*0.99
     scsize(4)*0.915],'menubar','none','resize','off','Name','ersen''s abcd','numbertitle','off');
17 - h.noBut=uicontrol('Style','text','Parent',h.fig,'Units','Normalized','position',[0.005 0.825
     0.24 0.175],'enable','off','BackgroundColor',get(h.fig,'color'));
18 - h.buttonFlat=uicontrol('Parent',h.fig,'style','pushbutton','Units','Normalized','position',[0.0
     05 0.825 0.05 0.05],'string','Flat Mirror');
19 - h.buttonCurved=uicontrol('Parent',h.fig,'style','pushbutton','Units','Normalized','position',[
     0.06 0.825 0.05 0.05],'string','Curved Mirror');
20 - h.buttonXtal=uicontrol('Parent',h.fig,'style','pushbutton','Units','Normalized','position',[0.1
     15 0.825 0.05 0.05],'string','Substrate','enable','off');
21 - h.buttonRemove=uicontrol('Parent',h.fig,'style','pushbutton','Units','Normalized','position',
     [0.17 0.825 0.05 0.05],'string','Remove Element','enable','off');
```

```
22 - h.radioAstig=uicontrol('Parent',h.fig,'style','checkbox','Units','Normalized','position',[0.003
     0.88 0.075
     0.04],'string','Astigmatism','BackgroundColor',get(h.fig,'color'),'FontSize',10,'visible','off','e
     nable','off');
23 - h.drawButton=uicontrol('Parent',h.fig,'style','pushbutton','Units','Normalized','Position',[0.
     12 0.9 0.1 0.05],'string','Draw','enable','off');
24 - h.wvTextBox=uicontrol('Parent',h.fig,'style','text','Units','Normalized','position',[0.003
     0.935 0.075 0.026],'string','Wavelength
     (nm):','HorizontalAlignment','center','FontSize',10,'BackgroundColor',get(h.fig,'color'));
25 - h.wvText=uicontrol('Parent',h.fig,'style','edit','Units','Normalized','position',[0.077 0.93
     0.035 0.04],'FontSize',10);
26 -
27 - h.cavityName=uicontrol('Parent',h.fig,'style','text','Units','Normalized','position',[0.005 0.8
     0.24 0.025],'string','Cavity
     Sketch:','HorizontalAlignment','left','FontSize',10,'BackgroundColor',get(h.fig,'color'));
28 - h.mirrorPanel=uipanel('Parent',h.fig,'Position',[0.005 0.005 0.24
     0.77],'BorderWidth',0,'BackgroundColor',get(h.fig,'color'));
29 - h.cavityScroll=uicontrol('Parent',h.fig,'Style','slider','Units','normalized','Position',[0.23
     0.005 0.015 0.765],'Value',1,'enable','off','visible','off');
30 - h.drawLines=axes('Parent',h.fig,'Position',[0.005 0.005 0.24
     0.77],'color',get(h.fig,'color'),'visible','off');
31 -
32 - h.distanceName=uicontrol('Parent',h.fig,'style','text','Units','Normalized','position',[0.247
     0.98 0.3
     0.02],'string','Distances:','HorizontalAlignment','left','FontSize',10,'BackgroundColor',get(h.f
     ig,'color'));
33 - h.sliderPanel=uipanel('Parent',h.fig,'Units','Normalized','Position',[0.247 0.005 0.3
     0.88],'BorderWidth',0,'BackgroundColor',get(h.fig,'color'));
34 - h.distanceScroll=uicontrol('Parent',h.fig,'Style','slider','Units','normalized','Position',[0.547
     0.005 0.015 0.925],'Value',1,'enable','off','visible','off');
35 -
36 - h.stabilityRes=uicontrol('Parent',h.fig,'style','text','Units','Normalized','position',[0.58 0.1
     0.4 0.2],'BackgroundColor',get(h.fig,'color'));
37 - h.drawPanel=axes('Parent',h.fig,'Position',[0.58 0.5 0.4 0.45]);
38 - h.drawPanel2=uipanel('Parent',h.fig,'Position',[0.58 0.005 0.4
     0.45],'BorderWidth',0,'BackgroundColor',get(h.fig,'color'));
39 -
40 - h.cursorButton=uicontrol('Parent',h.fig,'style','toggle','Units','Normalized','Position',[0.61
     0.4 0.1 0.05],'string','Cursor','enable','off');
41 - h.zoomInButton=uicontrol('Parent',h.fig,'style','toggle','Units','Normalized','Position',[0.73
```

```
      0.4 0.1 0.05],'string','Zoom In','enable','off');
42  - h.zoomOutButton=uicontrol('Parent',h.fig,'style','push','Units','Normalized','Position',[0.85
      0.4 0.1 0.05],'string','Zoom Out','enable','off');
43  - set(h.cursorButton,'callback',{@dataCursor});
44  - set(h.zoomInButton,'callback',{@zoomIn});
45  - set(h.zoomOutButton,'callback',{@zoomOut});
46  -
47  - h.signature=uicontrol('Parent',h.fig,'style','text','Units','Normalized','position',[0.58 0.005
      0.4 0.025],'string','designed & powered by Ersen Beyatlı & Alphan
      Sennaroğlu','BackgroundColor',get(h.fig,'color'));
48  -
49  - set(h.buttonFlat,'callback',{@addFlatDialog});
50  - set(h.buttonCurved,'callback',{@addCurvedDialog});
51  - set(h.buttonXtal,'callback',{@addXtalDialog});
52  -
53  - set(h.buttonRemove,'callback',{@removeButton});
54  -
55  - set(h.drawButton,'callback',{@draw});
56  -
57  - function []=addFlatDialog(hObj,evData)
58  - global numElements;
59  - global scsize;
60  - global fm;
61  - global names;
62  -
63  - if numElements==0
64  - h2.dlg=dialog('Position',[scsize(3)*0.4 scsize(4)*0.4 scsize(3)*0.2 scsize(4)*0.1],'Name','Flat
      Mirror Input');
65  - h2.textName=uicontrol('style','text','Units','Normalized','position',[0.01 0.4 0.48
      0.4],'string','Name of the mirror:','HorizontalAlignment','left');
66  - h2.editName=uicontrol('Parent',h2.dlg,'style','edit','Units','Normalized','position',[0.5 0.4
      0.48 0.4],'string',['Fm' num2str(fm)]);
67  - h2.buttonFlatOk=uicontrol('Parent',h2.dlg,'style','pushbutton','Units','Normalized','position
      ',[0.75 0.01 0.2 0.29],'string','Ok');
68  - set(h2.dlg,'KeyPressFcn',{@flatEnterOk,h2});
69  - set(h2.buttonFlatOk,'callback',{@flatOk,h2},'KeyPressFcn',{@flatEnterOk,h2});
70  - else
```

```
71 - h2.dlg=dialog('Position',[scsize(3)*0.4 scsize(4)*0.4 scsize(3)*0.2 scsize(4)*0.1],'Name','Flat
     Mirror Input');
72 - h2.textName=uicontrol('style','text','Units','Normalized','position',[0.01 0.7 0.48
     0.3],'string','Name of the mirror:','HorizontalAlignment','left');
73 - h2.editName=uicontrol('Parent',h2.dlg,'style','edit','Units','Normalized','position',[0.5 0.7
     0.48 0.3],'string',['Fm' num2str(fm)]);
74 - h2.textDistance=uicontrol('style','text','Units','Normalized','position',[0.01 0.4 0.48
     0.3],'string',['Distance to ' names{end} ':'],'HorizontalAlignment','left');
75 - h2.editDistance=uicontrol('Parent',h2.dlg,'style','edit','Units','Normalized','position',[0.5 0.4
     0.48 0.3]);
76 - h2.buttonFlatOk=uicontrol('Parent',h2.dlg,'style','pushbutton','Units','Normalized','position
     ',[0.75 0.01 0.2 0.29],'string','Ok');
77 - set(h2.dlg,'KeyPressFcn',{@flatEnterOk,h2});
78 - set(h2.buttonFlatOk,'callback',{@flatOk,h2},'KeyPressFcn',{@flatEnterOk,h2});
79 - end
80 -
81 - function []=flatEnterOk(hObj,evData,h2)
82 - if strcmp(evData.Key,'return')
83 - flatOk(hObj,evData,h2);
84 - end
85 -
86 - function []=addCurvedDialog(hObj,evData)
87 - global numElements;
88 - global scsize;
89 - global cm;
90 - global names;
91 -
92 - if numElements==0
93 - h2.dlg=dialog('Position',[scsize(3)*0.4 scsize(4)*0.4 scsize(3)*0.2
     scsize(4)*0.1],'Name','Curved Mirror Input');
94 - h2.textName=uicontrol('style','text','Units','Normalized','position',[0.01 0.7 0.48
     0.3],'string','Name of the mirror:','HorizontalAlignment','left');
95 - h2.editName=uicontrol('Parent',h2.dlg,'style','edit','Units','Normalized','position',[0.5 0.7
     0.48 0.3],'string',['Cm' num2str(cm)]);
96 - h2.textFocal=uicontrol('style','text','Units','Normalized','position',[0.01 0.4 0.48
     0.3],'string','Focal Length of the Mirror:','HorizontalAlignment','left');
97 - h2.editFocal=uicontrol('Parent',h2.dlg,'style','edit','Units','Normalized','position',[0.5 0.4
     0.48 0.3]);
```

```
 98 - h2.buttonCurvedOk=uicontrol('Parent',h2.dlg,'style','pushbutton','Units','Normalized','posi
      tion',[0.75 0.01 0.2 0.29],'string','Ok');
 99 - set(h2.dlg,'KeyPressFcn',{@curvedEnterOk,h2});
100 - set(h2.buttonCurvedOk,'callback',{@curvedOk,h2},'KeyPressFcn',{@curvedEnterOk,h2});
101 - else
102 - h2.dlg=dialog('Position',[scsize(3)*0.4 scsize(4)*0.4 scsize(3)*0.2
      scsize(4)*0.1333],'Name','Curved Mirror Input');
103 - h2.textName=uicontrol('style','text','Units','Normalized','position',[0.01 0.8 0.48
      0.2],'string','Name of the mirror:','HorizontalAlignment','left');
104 - h2.editName=uicontrol('Parent',h2.dlg,'style','edit','Units','Normalized','position',[0.5 0.8
      0.48 0.2],'string',['Cm' num2str(cm)]);
105 - h2.textFocal=uicontrol('style','text','Units','Normalized','position',[0.01 0.6 0.48
      0.2],'string','Focal Length of the Mirror:','HorizontalAlignment','left');
106 - h2.editFocal=uicontrol('Parent',h2.dlg,'style','edit','Units','Normalized','position',[0.5 0.6
      0.48 0.2]);
107 - h2.textDistance=uicontrol('style','text','Units','Normalized','position',[0.01 0.4 0.48
      0.2],'string',['Distance to ' names{end} ':'],'HorizontalAlignment','left');
108 - h2.editDistance=uicontrol('Parent',h2.dlg,'style','edit','Units','Normalized','position',[0.5 0.4
      0.48 0.2]);
109 - h2.buttonCurvedOk=uicontrol('Parent',h2.dlg,'style','pushbutton','Units','Normalized','posi
      tion',[0.75 0.01 0.2 0.29],'string','Ok');
110 - set(h2.dlg,'KeyPressFcn',{@curvedEnterOk,h2});
111 - set(h2.buttonCurvedOk,'callback',{@curvedOk,h2},'KeyPressFcn',{@curvedEnterOk,h2});
112 - end
113 -
114 - function []=curvedEnterOk(hObj,evData,h2)
115 - if strcmp(evData.Key,'return')
116 - curvedOk(hObj,evData,h2);
117 - end
118 -
119 - function []=addXtalDialog(hObj,evData)
120 -
121 - global scsize;
122 - global Xtal;
123 - global names;
124 -
125 - h2.dlg=dialog('Position',[scsize(3)*0.4 scsize(4)*0.4 scsize(3)*0.2
      scsize(4)*0.1666],'Name','Substrate Input');
```

```
126 - h2.textName=uicontrol('style','text','Units','Normalized','position',[0.01 0.85 0.48
      0.15],'string','Name of the mirror:','HorizontalAlignment','left');
127 - h2.editName=uicontrol('Parent',h2.dlg,'style','edit','Units','Normalized','position',[0.5 0.85
      0.48 0.15],'string',['Xtal' num2str(Xtal)]);
128 - h2.textRefIn=uicontrol('style','text','Units','Normalized','position',[0.01 0.7 0.48
      0.15],'string','Refractive Index:','HorizontalAlignment','left');
129 - h2.editRefIn=uicontrol('Parent',h2.dlg,'style','edit','Units','Normalized','position',[0.5 0.7
      0.48 0.15]);
130 - h2.textLength=uicontrol('style','text','Units','Normalized','position',[0.01 0.55 0.48
      0.15],'string','Length:','HorizontalAlignment','left');
131 - h2.editLength=uicontrol('Parent',h2.dlg,'style','edit','Units','Normalized','position',[0.5 0.55
      0.48 0.15]);
132 - h2.textDistance=uicontrol('style','text','Units','Normalized','position',[0.01 0.4 0.48
      0.15],'string',['Distance to ' names{end} ':'],'HorizontalAlignment','left');
133 - h2.editDistance=uicontrol('Parent',h2.dlg,'style','edit','Units','Normalized','position',[0.5 0.4
      0.48 0.15]);
134 - h2.buttonXtalOk=uicontrol('Parent',h2.dlg,'style','pushbutton','Units','Normalized','position
      ',[0.75 0.01 0.2 0.29],'string','Ok');
135 - set(h2.dlg,'KeyPressFcn',{@xtalEnterOk,h2});
136 - set(h2.buttonXtalOk,'callback',{@xtalOk,h2},'KeyPressFcn',{@xtalEnterOk,h2});
137 -
138 - function []=xtalEnterOk(hObj,evData,h2)
139 - if strcmp(evData.Key,'return')
140 - xtalOk(hObj,evData,h2);
141 - end
142 -
143 - function []=flatOk(hObj,evData,h2)
144 - global Cavity;
145 - global Cavity2;
146 - global numElements;
147 - global numElements2;
148 - global names;
149 - global fm;
150 - global Xtal;
151 - global h;
152 - global A;
153 - global B;
154 -
```

```
155 - if numElements==0
156 - name=get(h2.editName,'string');
157 - if ~isempty(name)
158 - names{end+1}=name;
159 - Cavity=flat();
160 - Cavity2=flat();
161 - numElements=numElements+1;
162 - numElements2=numElements2+1;
163 - set(h.buttonXtal,'enable','on');
164 - set(h.buttonRemove,'enable','on');
165 - fm=fm+1;
166 - h.mirrorButton(numElements)=uicontrol('style','pushbutton','parent',h.mirrorPanel,'Units',
      'normalized','position',[A B-0.075 0.2 0.075],'string',names{end});
167 - set(h.mirrorButton(numElements),'callback',{@flatButtons,numElements});
168 - if A==0.05
169 - A=0.69;
170 - else
171 - A=0.05;
172 - end
173 - B=B-0.075;
174 - delete(h2.dlg);
175 - cla(h.drawPanel,'reset');
176 - set(h.cursorButton,'value',0,'enable','off');dataCursor();
177 - set(h.zoomInButton,'value',0,'enable','off');zoom(h.drawPanel,'off');
178 - set(h.zoomOutButton,'enable','off');
179 - set(h.stabilityRes,'string','');
180 - set(h.drawButton,'enable','on');
181 - else
182 - errordlg('You should enter a name','error');
183 - end
184 - else
185 - name=get(h2.editName,'string');
186 - if ~isempty(name)
187 - dist2prev=get(h2.editDistance,'string');
188 - if ~isnan(str2double(dist2prev)) && ~isempty(str2double(dist2prev)) &&
      str2double(dist2prev)>0
189 - names{end+1}=name;
```

```
190 - dist2prev=str2double(dist2prev);
191 - if Cavity2(2,end)~=1
192 - set(h.lines(numElements-1),'visible','off');
193 - end
194 -
195 - Cavity=[Cavity dist(dist2prev) flat()];
196 - Cavity2=[Cavity2 dist(dist2prev) flat()];
197 - h.distMin(numElements)=uicontrol('style','edit','parent',h.sliderPanel,'Units','normalized','
      position',[0 B-0.075*(Xtal-1)+0.1 0.15
      0.04],'callback',{@sliderMinVal,numElements},'string',num2str(0.5*dist2prev));
198 - h.distMax(numElements)=uicontrol('style','edit','parent',h.sliderPanel,'Units','normalized','
      position',[0.85 B-0.075*(Xtal-1)+0.1 0.15
      0.04],'callback',{@sliderMaxVal,numElements},'string',num2str(1.5*dist2prev));
199 - h.distVal(numElements)=uicontrol('style','edit','parent',h.sliderPanel,'Units','normalized','p
      osition',[0.65 B+0.0375-0.075*(Xtal-1)+0.087 0.15
      0.04],'callback',{@sliderVal,numElements,numElements2},'string',num2str(dist2prev));
200 - h.distText(numElements)=uicontrol('style','text','parent',h.sliderPanel,'Units','normalized','
      position',[0.15 B+0.0375-0.075*(Xtal-1)+0.09 0.5 0.03],'string',['Distance between '
      names{end-1} '-'
      names{end}],'HorizontalAlignment','Left','FontSize',10,'BackgroundColor',get(h.fig,'color'));
201 - h.distSlider(numElements)=uicontrol('style','slider','parent',h.sliderPanel,'Units','normalize
      d','position',[0.15 B-0.075*(Xtal-1)+0.1 0.7
      0.025],'callback',{@sliderCall,numElements,numElements2},'min',0.5*dist2prev,'max',1.5*
      dist2prev,'val',dist2prev);
202 -
203 - if A==0.69
204 - h.lines(numElements)=plot(h.drawLines,[0.25,0.69],[B+0.0375,B-0.0375]);
205 - else
206 - h.lines(numElements)=plot(h.drawLines,[0.69,0.25],[B+0.0375,B-0.0375]);
207 - end
208 - hold(h.drawLines,'on');
209 - set(h.drawLines,'Xlim',[0,1],'Ylim',[0,1],'color',get(h.fig,'color'),'visible','off');
210 - numElements=numElements+1;
211 - numElements2=numElements2+2;
212 - fm=fm+1;
213 - h.mirrorButton(numElements)=uicontrol('style','pushbutton','parent',h.mirrorPanel,'Units',
      'normalized','position',[A B-0.075 0.2 0.075],'string',names{end});
214 - set(h.mirrorButton(numElements),'callback',{@flatButtons,numElements});
```

```
215 - if A==0.05
216 - A=0.69;
217 - else
218 - A=0.05;
219 - end
220 - B=B-0.075;
221 -
222 - if B<=0
223 - uistack(h.noBut,'top');
224 - uistack(h.buttonFlat,'top');
225 - uistack(h.buttonCurved,'top');
226 - uistack(h.buttonXtal,'top');
227 - uistack(h.buttonRemove,'top');
228 - uistack(h.radioAstig,'top');
229 - uistack(h.drawButton,'top');
230 - uistack(h.wvTextBox,'top');
231 - uistack(h.wvText,'top');
232 - uistack(h.cavityName,'top');
233 -
234 - set(h.mirrorPanel,'Position',[0.005 0.005 0.24 0.77]);
235 - set(h.cavityScroll,'enable','on','visible','on');
236 - pos=get(h.mirrorPanel,'Position');
237 - set(h.cavityScroll,'callback',{@mirrorScroll,pos},'min',1-abs(B),'max',1,'val',1);
238 -
239 - if B-0.075*(Xtal-1)+0.075<=0
240 - set(h.distanceScroll,'enable','on','visible','on');
241 - set(h.sliderPanel,'Position',[0.247 0.005 0.3 0.88]);
242 - pos2=get(h.sliderPanel,'Position');
243 - set(h.distanceScroll,'callback',{@sliderScroll,pos2},'min',1-abs(B),'max',1,'val',1);
244 - end
245 -
246 - end
247 - cla(h.drawPanel,'reset');
248 - set(h.cursorButton,'value',0,'enable','off');dataCursor();
249 - set(h.zoomInButton,'value',0,'enable','off');zoom(h.drawPanel,'off');
250 - set(h.zoomOutButton,'enable','off');
```

```
251 - set(h.stabilityRes,'string','');
252 - set(h.drawButton,'enable','on');
253 - delete(h2.dlg);
254 - else
255 - errordlg('You should enter a valid distance','error');
256 - end
257 - else
258 - errordlg('You should enter a name','error');
259 - end
260 - end
261 -
262 - function []=curvedOk(hObj,evData,h2)
263 - global Cavity;
264 - global Cavity2;
265 - global numElements;
266 - global numElements2;
267 - global names;
268 - global cm;
269 - global Xtal;
270 - global h;
271 - global A;
272 - global B;
273 -
274 - if numElements==0
275 - name=get(h2.editName,'string');
276 - if ~isempty(name)
277 - fcm=get(h2.editFocal,'string');
278 - if ~isnan(str2double(fcm)) && ~isempty(str2double(fcm)) && str2double(fcm)>0
279 - names{end+1}=name;
280 - fcm=str2double(fcm);
281 - Cavity=lens(fcm);
282 - Cavity2=lens(fcm);
283 - numElements=numElements+1;
284 - numElements2=numElements2+1;
285 - set(h.buttonXtal,'enable','on');
286 - set(h.buttonRemove,'enable','on');
```

```
287 -
288 - cm=cm+1;
289 - h.mirrorButton(numElements)=uicontrol('parent',h.mirrorPanel,'Units','normalized','positi
      on',[A B-0.075 0.2 0.075],'string',names{end});
290 - set(h.mirrorButton(numElements),'callback',{@curvedButtons,numElements,numElements
      2});
291 - if A==0.05
292 - A=0.69;
293 - else
294 - A=0.05;
295 - end
296 - B=B-0.075;
297 - set(h.stabilityRes,'string','');
298 - cla(h.drawPanel,'reset');
299 - set(h.cursorButton,'value',0,'enable','off');dataCursor();
300 - set(h.zoomInButton,'value',0,'enable','off');zoom(h.drawPanel,'off');
301 - set(h.zoomOutButton,'enable','off');
302 - set(h.drawButton,'enable','on');
303 - delete(h2.dlg);
304 - else
305 - errordlg('You should enter a valid focal length','error');
306 - end
307 - else
308 - errordlg('You should enter a name','error');
309 - end
310 - else
311 - name=get(h2.editName,'string');
312 - if ~isempty(name)
313 - fcm=get(h2.editFocal,'string');
314 - if ~isnan(str2double(fcm)) && ~isempty(str2double(fcm)) && str2double(fcm)>0
315 - dist2prev=get(h2.editDistance,'string');
316 - if ~isnan(str2double(dist2prev)) && ~isempty(str2double(dist2prev)) &&
      str2double(dist2prev)>0
317 - if Cavity2(2,end)~=1
318 - set(h.lines(numElements-1),'visible','off');
319 - end
320 - names{end+1}=name;
```

```
321 - fcm=str2double(fcm);
322 - dist2prev=str2double(dist2prev);
323 - Cavity=[Cavity dist(dist2prev) lens(fcm)];
324 - Cavity2=[Cavity2 dist(dist2prev) lens(fcm)];
325 - h.distMin(numElements)=uicontrol('style','edit','parent',h.sliderPanel,'Units','normalized','
      position',[0 B-0.075*(Xtal-1)+0.1 0.15
      0.04],'callback',{@sliderMinVal,numElements},'string',num2str(0.5*dist2prev));
326 - h.distMax(numElements)=uicontrol('style','edit','parent',h.sliderPanel,'Units','normalized','
      position',[0.85 B-0.075*(Xtal-1)+0.1 0.15
      0.04],'callback',{@sliderMaxVal,numElements},'string',num2str(1.5*dist2prev));
327 - h.distVal(numElements)=uicontrol('style','edit','parent',h.sliderPanel,'Units','normalized','p
      osition',[0.65 B+0.0375-0.075*(Xtal-1)+0.087 0.15
      0.04],'callback',{@sliderVal,numElements,numElements2},'string',num2str(dist2prev));
328 - h.distText(numElements)=uicontrol('style','text','parent',h.sliderPanel,'Units','normalized','
      position',[0.15 B+0.0375-0.075*(Xtal-1)+0.09 0.5 0.03],'string',['Distance between '
      names{end-1} '-'
      names{end}],'HorizontalAlignment','Left','FontSize',10,'BackgroundColor',get(h.fig,'color'));
329 - h.distSlider(numElements)=uicontrol('style','slider','parent',h.sliderPanel,'Units','normalize
      d','position',[0.15 B-0.075*(Xtal-1)+0.1 0.7
      0.025],'callback',{@sliderCall,numElements,numElements2},'min',0.5*dist2prev,'max',1.5*
      dist2prev,'val',dist2prev);
330 -
331 - if A==0.69
332 - h.lines(numElements)=plot(h.drawLines,[0.25,0.69],[B+0.0375,B-0.0375]);
333 - else
334 - h.lines(numElements)=plot(h.drawLines,[0.69,0.25],[B+0.0375,B-0.0375]);
335 - end
336 - hold(h.drawLines,'on');
337 - set(h.drawLines,'Xlim',[0,1],'Ylim',[0,1],'color',get(h.fig,'color'),'visible','off');
338 - numElements=numElements+1;
339 - numElements2=numElements2+2;
340 -
341 - cm=cm+1;
342 - h.mirrorButton(numElements)=uicontrol('parent',h.mirrorPanel,'Units','normalized','positi
      on',[A B-0.075 0.2 0.075],'string',names{end});
343 - set(h.mirrorButton(numElements),'callback',{@curvedButtons,numElements,numElements
      2});
344 - if A==0.05
```

```
345 - A=0.69;
346 - else
347 - A=0.05;
348 - end
349 - B=B-0.075;
350 -
351 - if B<=0
352 - uistack(h.noBut,'top');
353 - uistack(h.buttonFlat,'top');
354 - uistack(h.buttonCurved,'top');
355 - uistack(h.buttonXtal,'top');
356 - uistack(h.buttonRemove,'top');
357 - uistack(h.radioAstig,'top');
358 - uistack(h.drawButton,'top');
359 - uistack(h.wvTextBox,'top');
360 - uistack(h.wvText,'top');
361 - uistack(h.cavityName,'top');
362 -
363 - set(h.mirrorPanel,'Position',[0.005 0.005 0.24 0.77]);
364 - set(h.cavityScroll,'enable','on','visible','on');
365 - pos=get(h.mirrorPanel,'Position');
366 - set(h.cavityScroll,'callback',{@mirrorScroll,pos},'min',1-abs(B),'max',1,'val',1);
367 -
368 - if B-0.075*(Xtal-1)+0.075<=0
369 - set(h.sliderPanel,'Position',[0.247 0.005 0.3 0.88]);
370 - set(h.distanceScroll,'enable','on','visible','on');
371 - pos2=get(h.sliderPanel,'Position');
372 - set(h.distanceScroll,'callback',{@sliderScroll,pos2},'min',1-abs(B),'max',1,'val',1);
373 - end
374 - end
375 - cla(h.drawPanel,'reset');
376 - set(h.cursorButton,'value',0,'enable','off');dataCursor();
377 - set(h.zoomInButton,'value',0,'enable','off');zoom(h.drawPanel,'off');
378 - set(h.zoomOutButton,'enable','off');
379 - set(h.stabilityRes,'string','');
380 - set(h.drawButton,'enable','on');
```

```
381 - delete(h2.dlg);
382 - else
383 - errordlg('You should enter a valid distance','error');
384 - end
385 - else
386 - errordlg('You should enter a valid focal length','error');
387 - end
388 - else
389 - errordlg('You should enter a name','error');
390 - end
391 - end
392 -
393 - function []=xtalOk(hObj,evData,h2)
394 - global Cavity;
395 - global Cavity2;
396 - global numElements;
397 - global numElements2;
398 - global names;
399 - global Xtal;
400 - global h;
401 - global B;
402 -
403 - name=get(h2.editName,'string');
404 - if ~isempty(name)
405 - leng=get(h2.editLength,'string');
406 - if ~isnan(str2double(leng)) && ~isempty(str2double(leng)) && str2double(leng)>0
407 - refIn=get(h2.editRefIn,'string');
408 - if ~isnan(str2double(refIn)) && ~isempty(str2double(refIn)) && str2double(refIn)>1
409 - dist2prev=get(h2.editDistance,'string');
410 - if ~isnan(str2double(dist2prev)) && ~isempty(str2double(dist2prev)) &&
      str2double(dist2prev)>0
411 - names{end+1}=name;
412 - leng=str2double(leng);
413 - refIn=str2double(refIn);
414 - dist2prev=str2double(dist2prev);
415 - Cavity=[Cavity dist(dist2prev) xtal(leng,refIn)];
```

```
416 - Cavity2=[Cavity2 dist(dist2prev) xtal2(leng,refIn)];
417 - h.distMin(numElements)=uicontrol('style','edit','parent',h.sliderPanel,'Units','normalized','
      position',[0 B-0.075*(Xtal-1)+0.1 0.15
      0.04],'callback',{@sliderMinVal,numElements},'string',num2str(0.5*dist2prev));
418 - h.distMax(numElements)=uicontrol('style','edit','parent',h.sliderPanel,'Units','normalized','
      position',[0.85 B-0.075*(Xtal-1)+0.1 0.15
      0.04],'callback',{@sliderMaxVal,numElements},'string',num2str(1.5*dist2prev));
419 - h.distVal(numElements)=uicontrol('style','edit','parent',h.sliderPanel,'Units','normalized','p
      osition',[0.65 B+0.0375-0.075*(Xtal-1)+0.087 0.15
      0.04],'callback',{@sliderVal,numElements,numElements2},'string',num2str(dist2prev));
420 - h.distText(numElements)=uicontrol('style','text','parent',h.sliderPanel,'Units','normalized','
      position',[0.15 B+0.0375-0.075*(Xtal-1)+0.09 0.5 0.03],'string',['Distance between '
      names{end-1} '-'
      names{end}],'HorizontalAlignment','Left','FontSize',10,'BackgroundColor',get(h.fig,'color'));
421 - h.distSlider(numElements)=uicontrol('style','slider','parent',h.sliderPanel,'Units','normalize
      d','position',[0.15 B-0.075*(Xtal-1)+0.1 0.7
      0.025],'callback',{@sliderCall,numElements,numElements2},'min',0.5*dist2prev,'max',1.5*
      dist2prev,'val',dist2prev);
422 - numElements=numElements+1;
423 - numElements2=numElements2+4;
424 - if B-0.075*(Xtal-1)+0.075<=0
425 - set(h.sliderPanel,'Position',[0.247 0.005 0.3 0.88]);
426 - set(h.distanceScroll,'enable','on','visible','on');
427 - pos2=get(h.sliderPanel,'Position');
428 - set(h.distanceScroll,'callback',{@sliderScroll,pos2},'min',1-abs(B),'max',1,'val',1);
429 - end
430 -
431 - Xtal=Xtal+1;
432 - addXtalButtons();
433 - cla(h.drawPanel,'reset');
434 - set(h.cursorButton,'value',0,'enable','off');dataCursor();
435 - set(h.zoomInButton,'value',0,'enable','off');zoom(h.drawPanel,'off');
436 - set(h.zoomOutButton,'enable','off');
437 - set(h.stabilityRes,'string','');
438 - set(h.drawButton,'enable','on');
439 - delete(h2.dlg);
440 - else
441 - errordlg('You should enter a valid distance','error');
```

```
442 - end
443 - else
444 - errordlg('You should enter a valid refractive index (should be greater than 1)','error');
445 - end
446 - else
447 - errordlg('You should enter a valid substrate length','error');
448 - end
449 - else
450 - errordlg('You should enter a name','error');
451 - end
452 -
453 - function []=addXtalButtons(hObj,evData)
454 -
455 - global h;
456 - global A;
457 - global B;
458 - global Cavity2;
459 - global numElements;
460 - global numElements2;
461 - global names;
462 -
463 - index=numElements2;
464 - counter=0;
465 - while Cavity2(2,2*index)~=1
466 - counter=counter+1;
467 - index=index-4;
468 - end
469 -
470 - Axtal=(0.44-counter*0.1)/(counter+1);
471 - if A==0.69
472 - Ax=0.69-Axtal-0.1;
473 - elseif A==0.05
474 - Ax=0.25+Axtal;
475 - end
476 - Bxtal=0.075/(counter+1);
477 - Bx=B-(counter)*Bxtal;
```

```
478 - h.mirrorButton(numElements)=uicontrol('parent',h.mirrorPanel,'Units','normalized','positi
      on',[Ax Bx 0.1 0.075],'string',names{end});
479 - set(h.mirrorButton(numElements),'callback',{@xtalButtons,numElements,numElements2});
480 -
481 - if A==0.69
482 - h.lines(numElements-1)=plot(h.drawLines,[0.25,Ax+0.05],[B+0.0375,Bx+0.0375]);
483 - else
484 - h.lines(numElements-1)=plot(h.drawLines,[0.69,Ax+0.05],[B+0.0375,Bx+0.0375]);
485 - end
486 - hold(h.drawLines,'on');
487 - set(h.drawLines,'Xlim',[0,1],'Ylim',[0,1],'color',get(h.fig,'color'),'visible','off');
488 -
489 - for ii=1:counter-1
490 - if A==0.69
491 - Ax=0.69-(ii+1)*Axtal-(ii+1)*0.1;
492 - elseif A==0.05
493 - Ax=0.25+(ii+1)*Axtal+ii*0.1;
494 - end
495 - Bx=B-(counter-ii)*Bxtal;
496 - set(h.mirrorButton(numElements-ii),'position',[Ax Bx 0.1 0.075]);
497 - set(h.lines(numElements-ii-1),'visible','off');
498 - end
499 -
500 - function []=sliderCall(hObj,evData,index,index2)
501 -
502 - global h;
503 - global Cavity;
504 - global Cavity2;
505 -
506 - distValue=get(h.distSlider(index),'value');
507 - set(h.distVal(index),'string',num2str(distValue));
508 - Cavity(1,4*index)=distValue;
509 - Cavity2(1,2*index2+2)=distValue;
510 - if strcmp(get(h.drawButton,'enable'),'off')==1
511 - draw();
512 - end
```

```
513 -
514 - function []=sliderMinVal(hObj,evData,index)
515 -
516 - global h;
517 -
518 - distMin=get(h.distMin(index),'string');
519 - distMin=str2double(distMin);
520 -
521 - distVal=get(h.distVal(index),'string');
522 - distVal=str2double(distVal);
523 -
524 - if distMin<distVal
525 - set(h.distSlider(index),'min',distMin);
526 - else
527 - set(h.distSlider(index),'min',0.9*distVal);
528 - set(h.distMin(index),'string',num2str(0.9*distVal));
529 - end
530 -
531 - function []=sliderMaxVal(hObj,evData,index)
532 -
533 - global h;
534 -
535 - distMax=get(h.distMax(index),'string');
536 - distMax=str2double(distMax);
537 -
538 - distVal=get(h.distVal(index),'string');
539 - distVal=str2double(distVal);
540 -
541 - if distMax>distVal
542 - set(h.distSlider(index),'max',distMax);
543 - else
544 - set(h.distSlider(index),'max',1.1*distVal);
545 - set(h.distMax(index),'string',num2str(1.1*distVal));
546 - end
547 -
548 - function []=sliderVal(hObj,evData,index,index2)
```

```
549 -
550 - global h;
551 - global Cavity;
552 - global Cavity2;
553 -
554 - distValue=get(h.distVal(index),'string');
555 - distValue=str2double(distValue);
556 -
557 - minValue=get(h.distSlider(index),'min');
558 - maxValue=get(h.distSlider(index),'max');
559 -
560 - if distValue<minValue
561 - set(h.distVal(index),'string',num2str(minValue));
562 - elseif distValue>maxValue
563 - set(h.distVal(index),'string',num2str(maxValue));
564 - end
565 -
566 - distValue=get(h.distVal(index),'string');
567 - distValue=str2double(distValue);
568 - set(h.distSlider(index),'val',distValue);
569 - Cavity(1,4*index)=distValue;
570 - Cavity2(1,2*index2+2)=distValue;
571 -
572 - if strcmp(get(h.drawButton,'enable'),'off')==1
573 - draw();
574 - end
575 -
576 - function []=flatButtons(hObj,evData,index)
577 - global names;
578 - global scsize;
579 - h2.dlg=dialog('Position',[scsize(3)*0.4 scsize(4)*0.4 scsize(3)*0.2 scsize(4)*0.1],'Name','Flat
      Mirror Input');
580 - h2.textName=uicontrol('style','text','Units','Normalized','position',[0.01 0.4 0.48
      0.4],'string','Name of the mirror:','HorizontalAlignment','left');
581 - h2.editName=uicontrol('Parent',h2.dlg,'style','edit','Units','Normalized','position',[0.5 0.4
      0.48 0.4],'string',names{index});
582 - h2.buttonFlatOk=uicontrol('Parent',h2.dlg,'style','pushbutton','Units','Normalized','position
```

```
',[0.75 0.01 0.2 0.29],'string','Ok');
583 - set(h2.dlg,'KeyPressFcn',{@flatButtonsEnterOk,h2,index});
584 - set(h2.buttonFlatOk,'callback',{@flatButtonsOk,h2,index},'KeyPressFcn',{@flatButtonsEnte
rOk,h2,index});
585 -
586 - function []=flatButtonsEnterOk(hObj,evData,h2,index)
587 - if strcmp(evData.Key,'return')
588 - flatButtonsOk(hObj,evData,h2,index);
589 - end
590 -
591 - function []=curvedButtons(hObj,evData,index,index2)
592 - global names;
593 - global scsize;
594 - global Cavity;
595 - h2.dlg=dialog('Position',[scsize(3)*0.4 scsize(4)*0.4 scsize(3)*0.2
scsize(4)*0.1],'Name','Curved Mirror Input');
596 - h2.textName=uicontrol('style','text','Units','Normalized','position',[0.01 0.7 0.48
0.3],'string','Name of the mirror:','HorizontalAlignment','left');
597 - h2.editName=uicontrol('Parent',h2.dlg,'style','edit','Units','Normalized','position',[0.5 0.7
0.48 0.3],'string',names{index});
598 - fcm=-1/Cavity(2,4*index-3);
599 - h2.textFocal=uicontrol('style','text','Units','Normalized','position',[0.01 0.4 0.48
0.3],'string','Focal Length of the Mirror:','HorizontalAlignment','left');
600 - h2.editFocal=uicontrol('Parent',h2.dlg,'style','edit','Units','Normalized','position',[0.5 0.4
0.48 0.3],'string',num2str(fcm));
601 - h2.buttonCurvedOk=uicontrol('Parent',h2.dlg,'style','pushbutton','Units','Normalized','posi
tion',[0.75 0.01 0.2 0.29],'string','Ok');
602 - set(h2.dlg,'KeyPressFcn',{@curvedButtonsEnterOk,h2,index,index2});
603 - set(h2.buttonCurvedOk,'callback',{@curvedButtonsOk,h2,index,index2},'KeyPressFcn',{@c
urvedButtonsEnterOk,h2,index,index2});
604 -
605 - function []=curvedButtonsEnterOk(hObj,evData,h2,index,index2)
606 - if strcmp(evData.Key,'return')
607 - curvedButtonsOk(hObj,evData,h2,index,index2);
608 - end
609 -
610 - function []=xtalButtons(hObj,evData,index,index2)
611 -
```

```
612 - global names;
613 - global scsize;
614 - global Cavity2;
615 - h2.dlg=dialog('Position',[scsize(3)*0.4 scsize(4)*0.4 scsize(3)*0.2
      scsize(4)*0.1],'Name','Substrate Input');
616 - h2.textName=uicontrol('style','text','Units','Normalized','position',[0.01 0.8 0.48
      0.2],'string','Name of the mirror:','HorizontalAlignment','left');
617 - h2.editName=uicontrol('Parent',h2.dlg,'style','edit','Units','Normalized','position',[0.5 0.8
      0.48 0.2],'string',names{index});
618 - refIn=Cavity2(2,2*index2);
619 - h2.textRefIn=uicontrol('style','text','Units','Normalized','position',[0.01 0.6 0.48
      0.2],'string','Refractive Index:','HorizontalAlignment','left');
620 - h2.editRefIn=uicontrol('Parent',h2.dlg,'style','edit','Units','Normalized','position',[0.5 0.6
      0.48 0.2],'string',num2str(refIn));
621 - leng=Cavity2(1,2*index2-2);
622 - h2.textLength=uicontrol('style','text','Units','Normalized','position',[0.01 0.4 0.48
      0.2],'string','Length:','HorizontalAlignment','left');
623 - h2.editLength=uicontrol('Parent',h2.dlg,'style','edit','Units','Normalized','position',[0.5 0.4
      0.48 0.2],'string',num2str(leng));
624 - h2.buttonXtalOk=uicontrol('Parent',h2.dlg,'style','pushbutton','Units','Normalized','position
      ',[0.75 0.01 0.2 0.29],'string','Ok');
625 - set(h2.dlg,'KeyPressFcn',{@xtalButtonsEnterOk,h2,index,index2});
626 - set(h2.buttonXtalOk,'callback',{@xtalButtonsOk,h2,index,index2},'KeyPressFcn',{@xtalButt
      onsEnterOk,h2,index,index2});
627 -
628 - function []=xtalButtonsEnterOk(hObj,evData,h2,index,index2)
629 - if strcmp(evData.Key,'return')
630 - xtalButtonsOk(hObj,evData,h2,index,index2);
631 - end
632 -
633 - function []=flatButtonsOk(hObj,evData,h2,index)
634 - global names;
635 - global h;
636 - global numElements;
637 - if ~isempty(get(h2.editName,'string'))
638 - names{index}=get(h2.editName,'string');
639 - set(h.mirrorButton(index),'string',get(h2.editName,'string'));
640 - if index==1
```

```
641 - if numElements~=1
642 - set(h.distText(index),'string',['Distance between ' names{index} '-' names{index+1}]);
643 - end
644 - elseif index==length(names)
645 - set(h.distText(index-1),'string',['Distance between ' names{index-1} '-' names{index}]);
646 - else
647 - set(h.distText(index-1),'string',['Distance between ' names{index-1} '-' names{index}]);
648 - set(h.distText(index),'string',['Distance between ' names{index} '-' names{index+1}]);
649 - end
650 -
651 - set(h.drawButton,'enable','on');
652 - cla(h.drawPanel,'reset');
653 - set(h.cursorButton,'value',0,'enable','off');dataCursor();
654 - set(h.zoomInButton,'value',0,'enable','off');zoom(h.drawPanel,'off');
655 - set(h.zoomOutButton,'enable','off');
656 - set(h.stabilityRes,'string','');
657 -
658 - delete(h2.dlg);
659 - else
660 - errordlg('You should enter a name','error');
661 - end
662 -
663 - function []=curvedButtonsOk(hObj,evData,h2,index,index2)
664 - global names;
665 - global h;
666 - global numElements;
667 - global Cavity;
668 - global Cavity2;
669 - if ~isempty(get(h2.editName,'string'))
670 - fcm=get(h2.editFocal,'string');
671 - if ~isnan(str2double(fcm)) && ~isempty(str2double(fcm)) && str2double(fcm)>0
672 - names{index}=get(h2.editName,'string');
673 - set(h.mirrorButton(index),'string',get(h2.editName,'string'));
674 - if index==1
675 - if numElements~=1
676 - set(h.distText(index),'string',['Distance between ' names{index} '-' names{index+1}]);
```

```
677 - end
678 - elseif index==length(names)
679 - set(h.distText(index-1),'string',['Distance between ' names{index-1} '-' names{index}]);
680 - else
681 - set(h.distText(index-1),'string',['Distance between ' names{index-1} '-' names{index}]);
682 - set(h.distText(index),'string',['Distance between ' names{index} '-' names{index+1}]);
683 - end
684 -
685 - fcm=str2double(fcm);
686 - Cavity(2,4*index-3)=-1/fcm;
687 - Cavity2(2,2*index2-1)=-1/fcm;
688 -
689 - set(h.drawButton,'enable','on');
690 - cla(h.drawPanel,'reset');
691 - set(h.cursorButton,'value',0,'enable','off');dataCursor();
692 - set(h.zoomInButton,'value',0,'enable','off');zoom(h.drawPanel,'off');
693 - set(h.zoomOutButton,'enable','off');
694 - set(h.stabilityRes,'string','');
695 -
696 - delete(h2.dlg);
697 - else
698 - errordlg('You should enter a valid focal length','error');
699 - end
700 - else
701 - errordlg('You should enter a name','error');
702 - end
703 -
704 - function []=xtalButtonsOk(hObj,evData,h2,index,index2)
705 - global names;
706 - global h;
707 - global Cavity;
708 - global Cavity2;
709 - if ~isempty(get(h2.editName,'string'))
710 - leng=get(h2.editLength,'string');
711 - if ~isnan(str2double(leng)) && ~isempty(str2double(leng)) && str2double(leng)>0
712 - refIn=get(h2.editRefIn,'string');
```

```
713 - if ~isnan(str2double(refIn)) && ~isempty(str2double(refIn)) && str2double(refIn)>1
714 - names{index}=get(h2.editName,'string');
715 - set(h.mirrorButton(index),'string',get(h2.editName,'string'));
716 - if index==1
717 - set(h.distText(index),'string',['Distance between ' names{index} '-' names{index+1}]);
718 - elseif index==length(names)
719 - set(h.distText(index-1),'string',['Distance between ' names{index-1} '-' names{index}]);
720 - else
721 - set(h.distText(index-1),'string',['Distance between ' names{index-1} '-' names{index}]);
722 - set(h.distText(index),'string',['Distance between ' names{index} '-' names{index+1}]);
723 - end
724 -
725 - refIn=str2double(refIn);
726 -
727 - leng=str2double(leng);
728 - Cavity(1,4*index-2)=leng/refIn;
729 - Cavity2(:,2*index2-5:2*index2)=xtal2(leng,refIn);
730 -
731 - set(h.drawButton,'enable','on');
732 - cla(h.drawPanel,'reset');
733 - set(h.cursorButton,'value',0,'enable','off');dataCursor();
734 - set(h.zoomInButton,'value',0,'enable','off');zoom(h.drawPanel,'off');
735 - set(h.zoomOutButton,'enable','off');
736 - set(h.stabilityRes,'string','');
737 -
738 - delete(h2.dlg);
739 - else
740 - errordlg('You should enter a valid refractive index greater than 1','error');
741 - end
742 - else
743 - errordlg('You should enter a valid crystal length','error');
744 - end
745 - else
746 - errordlg('You should enter a name','error');
747 - end
748 -
```

```
749 - function []=removeButton(hObj,evData)
750 - global h;
751 - global A;
752 - global B;
753 - global numElements;
754 - global numElements2;
755 - global Cavity;
756 - global Cavity2;
757 - global fm;
758 - global cm;
759 - global Xtal;
760 - global names;
761 -
762 - names{numElements}='';
763 - if numElements==1
764 - fm=1;
765 - cm=1;
766 - Cavity=[];
767 - Cavity2=[];
768 - delete(h.mirrorButton(numElements));
769 - numElements=0;
770 - numElements2=0;
771 - A=0.05;
772 - B=1;
773 - set(h.buttonXtal,'enable','off');
774 - set(h.buttonRemove,'enable','off');
775 - set(h.drawButton,'enable','off');
776 - else
777 - if Cavity(1,end)~=0
778 - delete(h.mirrorButton(numElements));
779 - Cavity=Cavity(:,1:end-4);
780 - Cavity2=Cavity2(:,1:end-8);
781 - numElements=numElements-1;
782 - numElements2=numElements2-4;
783 -
784 - index=numElements2;
```

```
785 - counter=0;
786 - while Cavity2(2,2*index)~=1
787 - counter=counter+1;
788 - index=index-4;
789 - end
790 -
791 - Axtal=(0.44-counter*0.1)/(counter+1);
792 - if A==0.69
793 - Ax=0.69-Axtal-0.1;
794 - elseif A==0.05
795 - Ax=0.25+Axtal;
796 - end
797 - Bxtal=0.075/(counter+1);
798 - for ii=1:counter
799 - if A==0.69
800 - Ax=0.69-(ii)*Axtal-(ii)*0.1;
801 - elseif A==0.05
802 - Ax=0.25+(ii)*Axtal+(ii-1)*0.1;
803 - end
804 - Bx=B-(counter-ii+1)*Bxtal;
805 - set(h.mirrorButton(numElements-ii+1),'position',[Ax Bx 0.1 0.075]);
806 - end
807 - Xtal=Xtal-1;
808 - else
809 - if A==0.05
810 - A=0.69;
811 - else
812 - A=0.05;
813 - end
814 - B=B+0.075;
815 - delete(h.mirrorButton(numElements));
816 - numElements=numElements-1;
817 - numElements2=numElements2-2;
818 - if Cavity(2,end-1)<0
819 - cm=cm-1;
820 - else
```

```
821 - fm=fm-1;
822 - end
823 - Cavity=Cavity(:,1:end-4);
824 - Cavity2=Cavity2(:,1:end-4);
825 - end
826 -
827 - delete(h.distMin(numElements));
828 - delete(h.distMax(numElements));
829 - delete(h.distVal(numElements));
830 - delete(h.distText(numElements));
831 - delete(h.distSlider(numElements));
832 - delete(h.lines(numElements));
833 -
834 - if numElements>1
835 - set(h.lines(numElements-1),'visible','on');
836 - end
837 -
838 - cla(h.drawPanel,'reset');
839 - set(h.cursorButton,'value',0,'enable','off');dataCursor();
840 - set(h.zoomInButton,'value',0,'enable','off');zoom(h.drawPanel,'off');
841 - set(h.zoomOutButton,'enable','off');
842 - set(h.stabilityRes,'string','');
843 - set(h.drawButton,'enable','on');
844 -
845 - set(h.sliderPanel,'Position',[0.247 0.005 0.3 0.88]);
846 - set(h.mirrorPanel,'Position',[0.005 0.005 0.24 0.77]);
847 - set(h.cavityScroll,'min',1-abs(B),'max',1,'val',1);
848 - set(h.distanceScroll,'min',0,'max',1,'val',1);
849 - set(h.drawLines,'Ylim',[0 1]);
850 -
851 - if B-0.075*(Xtal-1)+0.075>0
852 - set(h.distanceScroll,'enable','off','visible','off');
853 - end
854 - if B>0
855 - set(h.cavityScroll,'enable','off','visible','off');
856 - end
```

```
857 - end
858 -
859 - function []=mirrorScroll(hObj,evData,pos)
860 - global h;
861 - slidervalue=get(h.cavityScroll,'Value');
862 - set(h.mirrorPanel,'Position',[pos(1) pos(2)-slidervalue+1 pos(3) pos(4)]);
863 - set(h.drawLines,'Ylim',[slidervalue-1 slidervalue]);
864 -
865 - function []=sliderScroll(hObj,evData,pos)
866 - global h;
867 - slidervalue=get(h.distanceScroll,'Value');
868 - set(h.sliderPanel,'Position',[pos(1) pos(2)-slidervalue+1 pos(3) pos(4)]);
869 -
870 - function []=dataCursor(hObj,evData)
871 - global h;
872 -
873 -
874 - if get(h.cursorButton,'value')==0
875 - datacursormode off;
876 - set(h.drawLines,'HitTest','off')
877 - else
878 - datacursormode on;
879 - set(h.drawLines,'HitTest','off')
880 - end
881 -
882 - function []=zoomIn(hObj,evData)
883 - global h;
884 - x=zoom;
885 - setAllowAxesZoom(x,h.drawLines,false);
886 - if get(h.zoomInButton,'value')==0
887 - zoom(h.drawPanel,'off');
888 - else
889 - zoom(h.drawPanel,'on');
890 - end
891 -
892 - function []=zoomOut(hObj,evData)
```

```
893 - global h;
894 - x=zoom;
895 - setAllowAxesZoom(x,h.drawLines,false);
896 - if get(h.zoomInButton,'value')==0
897 - zoom(h.drawPanel,'off');
898 - else
899 - zoom(h.drawPanel,'out');
900 - end
901 -
902 - function []=draw(hObj,evData)
903 - global h;
904 - global Cavity;
905 - global Cavity2;
906 -
907 - lambda=get(h.wvText,'string');
908 - if ~isnan(str2double(lambda)) && ~isempty(str2double(lambda)) &&
      str2double(lambda)>0
909 - lambda=str2double(lambda);
910 - lambda=lambda*10^-9;
911 -
912 - totaldist=0;
913 - distMatrix=[];
914 - mirrorMatrix=[];
915 - for ii=1:length(Cavity2)/2
916 - if Cavity2(1,2*ii)~=0
917 - totaldist=totaldist+Cavity2(1,2*ii);
918 - distMatrix=[distMatrix [Cavity2(1,2*ii-1) Cavity2(1,2*ii); Cavity2(2,2*ii-1) Cavity2(2,2*ii)]];
919 - else
920 - mirrorMatrix=[mirrorMatrix [Cavity2(1,2*ii-1) Cavity2(1,2*ii); Cavity2(2,2*ii-1)
      Cavity2(2,2*ii)]];
921 - end
922 - end
923 - Mt=[1,0;0,1];
924 - for ii=1:length(Cavity)/2
925 - M=[Cavity(1,2*ii-1) Cavity(1,2*ii); Cavity(2,2*ii-1) Cavity(2,2*ii)];
926 - Mt=Mt*M;
927 - end
```

```
928 - for ii=length(Cavity)/2-1:-1:2
929 - M=[Cavity(1,2*ii-1) Cavity(1,2*ii); Cavity(2,2*ii-1) Cavity(2,2*ii)];
930 - Mt=Mt*M;
931 - end
932 -
933 - stability=(abs((Mt(1,1)+Mt(2,2))/2)<=1);
934 - if stability==0
935 - set(h.stabilityRes,'string','the system is NOT
      stable','BackgroundColor',get(h.fig,'color'),'FontSize',15);
936 - cla(h.drawPanel,'reset');
937 - set(h.cursorButton,'value',0,'enable','off');dataCursor();
938 - set(h.zoomInButton,'value',0,'enable','off');zoom(h.drawPanel,'off');
939 - set(h.zoomOutButton,'enable','off');
940 - set(h.drawButton,'enable','off');
941 - else
942 - set(h.stabilityRes,'string','the system is
      stable','BackgroundColor',get(h.fig,'color'),'FontSize',15);
943 - set(h.cursorButton,'enable','on');
944 - set(h.zoomInButton,'enable','on');
945 - set(h.zoomOutButton,'enable','on');
946 - set(h.drawButton,'enable','off');
947 - resol=0.00001;
948 - n=1;
949 - q=1/((Mt(2,2)-Mt(1,1))/(2*Mt(1,2))-1i*sqrt(1-((Mt(1,1)+Mt(2,2))/2)^2)/abs(Mt(1,2)));
950 - z0=-1/imag(1/q);
951 - distance=0:resol:totaldist;
952 - w0new=zeros(1,length(distance));
953 - counter=1;
954 - counterMatrix=[];
955 - w0new(counter)=sqrt(z0*lambda/pi);
956 - for ii=1:length(distMatrix)/2
957 - M=[mirrorMatrix(1,2*ii-1) mirrorMatrix(1,2*ii);mirrorMatrix(2,2*ii-1) mirrorMatrix(2,2*ii)];
958 - if M(2,2)~=1
959 - n=n/M(2,2);
960 - counterMatrix=[counterMatrix counter];
961 - end
962 - q=(M(1,1)*q+M(1,2))/(M(2,1)*q+M(2,2));
```

```
963 - for jj=1:distMatrix(1,2*ii)/resol
964 - M=dist(resol);
965 - q=(M(1,1)*q+M(1,2))/(M(2,1)*q+M(2,2));
966 - z0=-1/imag(1/q);
967 - counter=counter+1;
968 - w0new(counter)=sqrt(z0*lambda/pi/n);
969 - end
970 - end
971 - plot(h.drawPanel,distance,w0new);
972 - axis(h.drawPanel,[0 max(distance) 0 max(w0new)]);
973 - grid on;
974 - end
975 - else
976 - errordlg('You should enter a valid wavelength','error');
977 - set(h.drawButton,'enable','on');
978 - end
979 -
980 - function res=dist(d)
981 - res=[1 d;0 1];
982 -
983 - function res=flat()
984 - res=[1 0; 0 1];
985 -
986 - function res=lens(f)
987 - res=[1 0; -1/f 1];
988 -
989 - function res=xtal(d,n)
990 - res=[1 d/n; 0 1];
991 -
992 - function res=xtal2(d,n)
993 - M1=[1 0; 0 n];
994 - M2=[1 d; 0 1];
995 - M3=[1 0; 0 1/n];
996 - res=[M3 M2 M1];
```

After running this program, Figure A1 appears in the window. To construct the four mirror cavity fallow the steps described below.

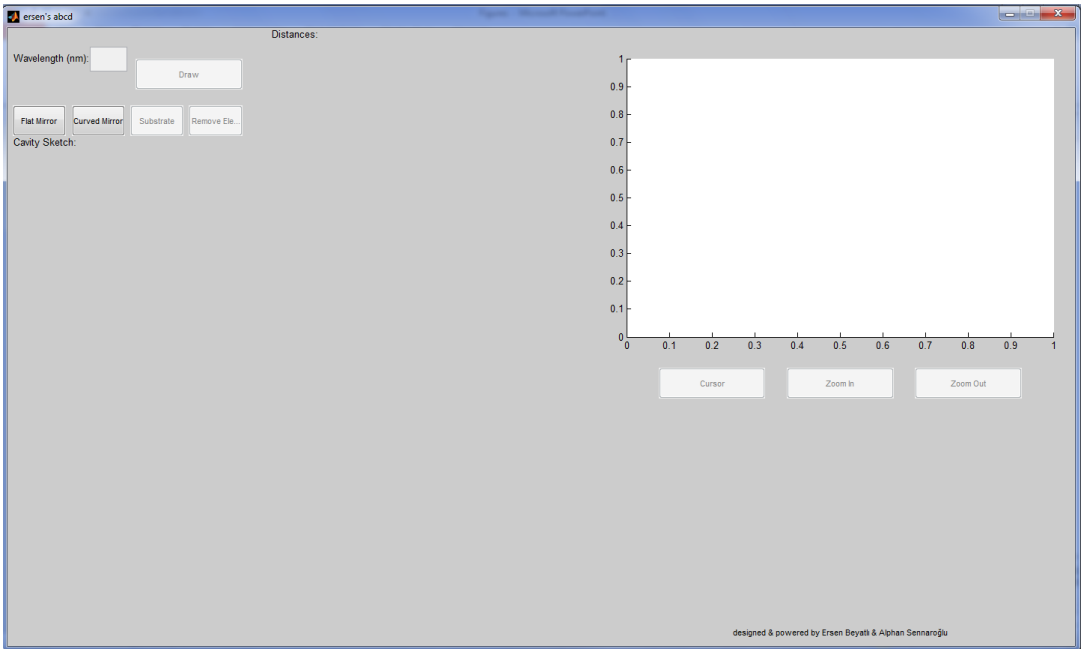

Figure A1: Empty screen of ersen's abcd program

1-) Enter the wavelength of the laser in nanometers to the text box next to the 'Wavelength (nm):' field. (2015 nm)

2-) Press Flat Mirror button to place the output coupler. A dialog box appears (Fig. A2) in the window that asks the name of the mirror. Write OC and press Ok button. This action places a button under the 'Cavity Sketch' field with a name OC

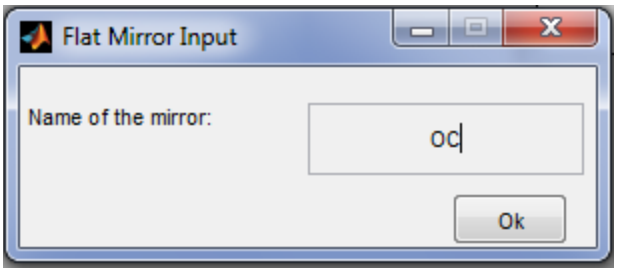

Figure A2: The dialog box appears after pressing the Flat Mirror button

3-) Press Curved Mirror button to place the first curved mirror. A dialog box appears (Fig. A3) in the window that asks the name of the mirror, the focal length and the distance to the previous element i.e. OC. Fill the text boxes as in Fig. A3 then press ok. After that, a sliderbar appears under the 'Distances:' field. Changing this bar changes the distances between Cm1 and OC. There is also three text box appears around the bar. The left one represents the minimum value of the bar, the right one show the maximum value and the upper one shows the current value of the bar. One can change these numbers by changing these fields and the bar updated itself accordingly. Moreover, another button appears in the 'Cavity Skecth:' field named Cm1 and a line between Cm1 and OC buttons that illustrates the path between these mirrors.

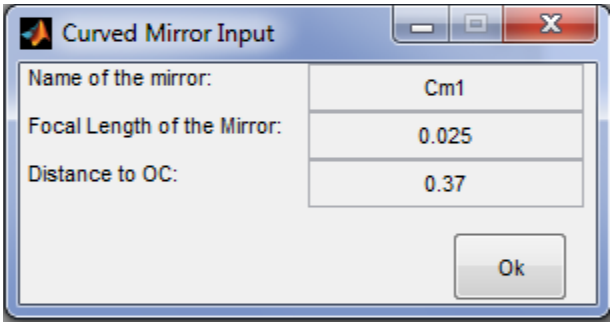

Figure A3: The dialog box appears after pressing the Curved Mirror button

4-) Press Substrate button to place the crystal. Another dialog box appears (Fig. A4) in the window that asks the name of the crystal, the refractive index, the length of the crystal and the distance to the previous element. Fill the text boxes as in Fig. A4 then press ok. This action places a button in the cavity sketch field for the crystal and a connection to Cm1. Moreover, a sliderbar and three different text boxes appear in the 'Distances' fields.

5-) Repeat the step 3 to place second curved mirror. Instead of writing Cm1, write Cm2 for the name of the mirror. Moreover, in this case let the distance to the crystal become 0.03 meter.

6-) Repeat the step 2 to place high reflector to the cavity. Let the initial distance to the previous element become 0.37 meter. At this point the window will become as in Figure A5.

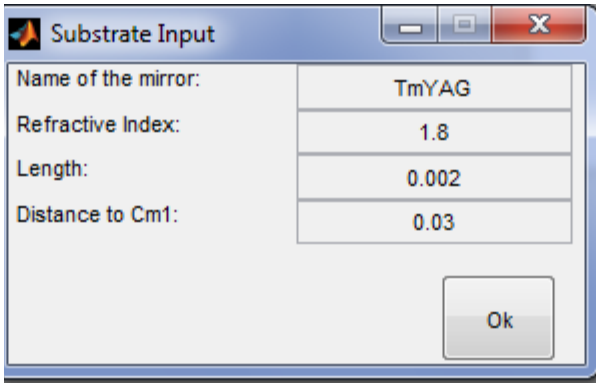

Figure A4: The dialog box appears after pressing the Substrate button

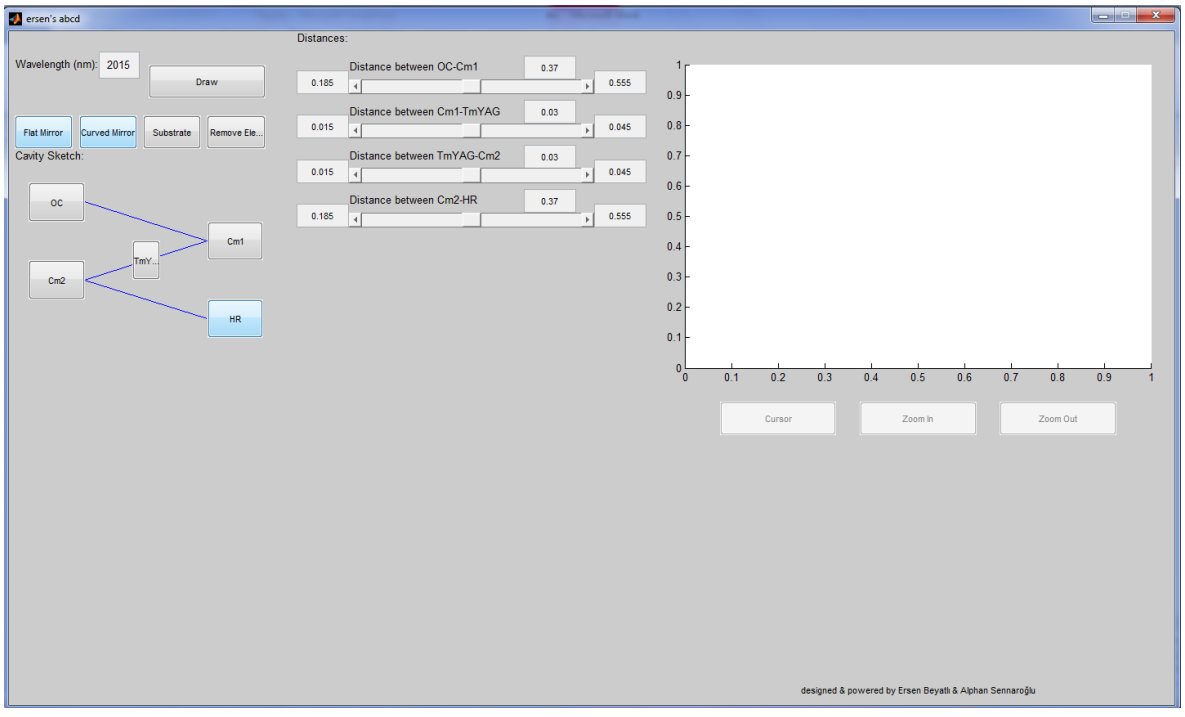

Figure A5: The window appearance after placing each element

7-) Press the Draw button, initially a sentence appears under the graph area 'The system is NOT stable'.

8-) Change the distance sliderbar values of 'Cm1-TmYAG' and 'TmYAG-Cm2' to 0.026 meter. Then a graph appears in the window that shows the spotsizes along the cavity (Fig. A6).

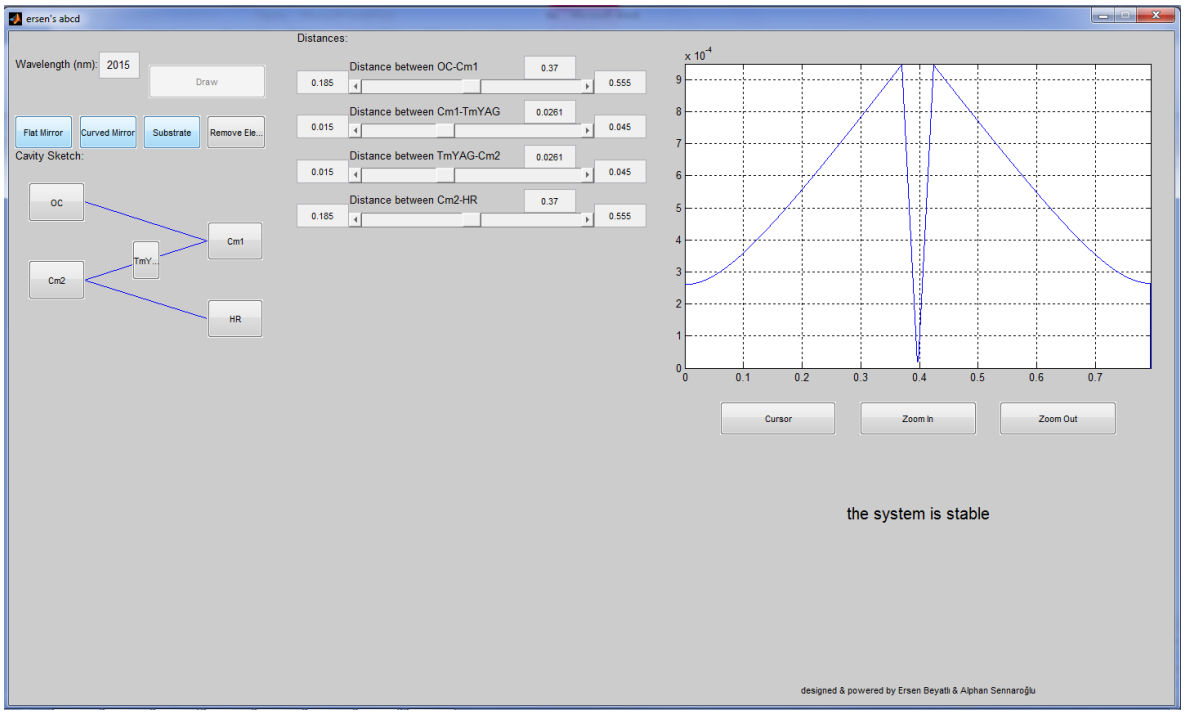

Figure A6: Final window for the 4-mirror Tm:YAG laser cavity

Additional Features:

- To see exact values of the spotsize at the specific locations press Cursor Button
- To zoom in (out) the graph press Zoom In (Zoom Out) button
- To change the properties of the elements press the corresponding buttons. In the opening dialog boxes change the properties accordingly
- To remove an element from the cavity press Remove Element button.

- If you make syntax error while entering the element properties such as writing a letter in the distance fields an error dialog box appears just after pressing Ok button and wants you to enter the value correctly.

VITA & LIST of PUBLICATIONS

Ersen BEYATLI was born in Kerkuk, Iraq on July 1, 1985. He received his BS degree in Electrical and Electronics Engineering from Bilkent University in 2008. He recently obtained his Ph.D. degree in Electrical and Electronics Engineering from Koç University (2014). His research interests include solid-state lasers, ultrafast optics, computational electromagnetism, microwave electronics and image processing. He is currently student member of OSA and SPIE.

Publications:

- H. Cankaya, M. Cizmeciyan, E. Beyatli, A. Gorgulu, A. Kurt, and A. Sennaroglu, "Injection-seeded, gain-switched tunable Cr:ZnSe laser," Opt. Lett. 37, 136-138 (2012).
- E. Beyatli, S. Nagizadeh, A. Kurt, and A. Sennaroglu, "Low-cost low-threshold diode end-pumped Tm:YAG laser at 2.016 μm," Applied Physics B 109, 221-225 (2012).
- E. Beyatli, A. Sennaroglu, and U. Demirbas, "Self-Q-switched Cr:LiCAF laser," J. Opt. Soc. Am. B 30, 914-921 (2013).
- E. Beyatli, I. Baali, B. Sumpf, G. Erbert, A. Leitenstorfer, A. Sennaroglu, and U. Demirbas, "Tapered diode-pumped continuous-wave alexandrite laser," J. Opt. Soc. Am. B 30, 3184-3192 (2013).
- F. Canbaz, E. Beyatli, L. Chen, A. Sennaroglu, F. Kaertner, and U. Demirbas, "Highly efficient and robust operation of Kerr-lens mode-locked Cr:LiSAF lasers using gain-matched output couplers," Opt. Lett. 39, 327-330 (2014).

- I. Yorulmaz, E. Beyatli, A. Kurt, A. Sennaroglu, and U. Demirbas, "Low-cost and low-threshold Alexandrite laser pumped by a single mode-diode," Opt. Mat. Expr. (submitted)
- C. Cihan, E. Beyatli, F. Canbaz, L. Chen, B. Sumpf, G. Erbert, A. Leitenstorfer, F. Kaertner, A. Sennaroglu, and U. Demirbas " Gain-Matched Output Couplers for Efficient Kerr-Lens Mode-Locking of Low-Cost Cr:LiSAF Lasers" (in preparation)
- E. Beyatli, I. Yorulmaz, A. Kurt, and A. Sennaroglu, "Repetitively Q-switched Tm:YAG and Tm:LuAG Lasers Pumped by Low-cost Laser Diodes," (in preparation)

Proceedings:

- H. Cankaya, M. Cizmeciyan, E. Beyatli, A. Gorgulu, A. Kurt, and A. Sennaroglu, "Injection-seeded, narrow-line gain-switched Cr:ZnSe laser," in ASSP 2012
- E. Beyatli, A. Sennaroglu, and U. Demirbas, "Self-Q-switched Cr:LiCAF laser near 800 nm," in Photonics West 2013
- F. Canbaz, E. Beyatli, L. Chen, A. Sennaroglu, F. Kaertner, and U. Demirbas, "Efficient and Robust Kerr-Lens Mode-Locking of Cr:LiSAF Lasers Using Gain-Matched Output Couplers," in ASSL 2013
- E. Beyatli, I. Baali, I. Yorulmaz, A. Kurt, B. Sumpf, G. Erbert, A. Sennaroglu, A. Leitenstorfer, and U. Demirbas, "Efficient and Low-Threshold Alexandrite Lasers Pumped by High-Brightness Diodes," in ASSL 2013
- C. Cihan, E. Beyatli, F. Canbaz, L. Chen, B. Sumpf, G. Erbert, A. Leitenstorfer, F. Kaertner, A. Sennaroglu, and U. Demirbas "Gain-Matched Output Couplers (GMOCs) for Efficient and Robust Kerr-Lens Mode-Locking of Cr:LiSAF lasers" in CLEO 2014 (submitted)

BIBLIOGRAPHY

[1] T. H. Maiman, "Stimulated optical radiation in ruby," *Nature,* vol. 187, pp. 493-494, 1960.

[2] U. Demirbas, A. Sennaroglu, F. X. Kaertner, and J. G. Fujimoto, "Highly efficient, low-cost femtosecond Cr3+: LiCAF laser pumped by single-mode diodes," *Optics Letters,* vol. 33, pp. 590-592, 2008.

[3] U. Demirbas, D. Li, J. R. Birge, A. Sennaroglu, G. S. Petrich, L. A. Kolodziejski, F. X. Kartner, and J. G. Fujimoto, "Low-cost, single-mode diode-pumped Cr:Colquiriite lasers," *Optics Express,* vol. 17, pp. 14374-14388, Aug 3 2009.

[4] U. Demirbas, G. S. Petrich, D. Li, A. Sennaroglu, L. A. Kolodziejski, F. X. Kärtner, and J. G. Fujimoto, "Femtosecond tuning of Cr:colquiriite lasers with AlGaAs-based saturable Bragg reflectors," *J. Opt. Soc. Am. B,* vol. 28, pp. 986-993, 2011.

[5] B. C. Weber and A. Hirth, "Efficient single-pulse emission with submicrosecond duration from a Cr:LiSAF laser," *Optics Communications,* vol. 128, pp. 158-165, Jul 1 1996.

[6] B. C. Weber and A. Hirth, "Presentation of a new and simple technique of Q-switching with a LiSrAlF6:Cr3+ oscillator," *Optics Communications,* vol. 149, pp. 301-306, 1998.

[7] M. Wolters, M. Kramer, J. Becker, M. Christgen, U. Nagele, F. Imkamp, M. Burchardt, A. Merseburger, M. Kuczyk, T. Bach, A. Gross, and T. Herrmann, "Tm:YAG laser en bloc mucosectomy for accurate staging of primary bladder cancer: early experience," *World Journal of Urology,* vol. 29, pp. 429-432, 2011.

[8] D. P. Poppas and D. S. Scherr, "Laser tissue welding: a urological surgeon's perspective," *Hemophilia,* vol. 4, pp. 456-462, 1998.

[9] N. M. Fried, "High-power laser vaporization of the canine prostate using a 110 W thulium fiber laser at 1.91 mu m," *Lasers in Surgery and Medicine,* vol. 36, pp. 52-56, JAN 2005.

[10] R. C. Stoneman and L. Esterowitz, "Efficient, broadly tunable, laser-pumped Tm:YAG and Tm:YSGG cw lasers," *Optics Letters,* vol. 15, pp. 486-488, 1990.

[11] H. Kalaycioglu and A. Sennaroglu, "Low-threshold continuous-wave Tm^{3+}:$YAlO_3$ laser," *Opt. Commun.,* vol. 281, pp. 4071-4074, 2008.

[12] A. Dergachev, K. Wall, and P. F. Moulton, "A CW Side-Pumped Tm:YLF Laser," in *OSA TOPS Advanced Solid State Lasers*, 2002, pp. 343-346.

[13] P. Cerny, J. Sulc, and H. Jelinkova, "Continously tunable diode-pumped Tm:YAP laser," in *SPIE Solid State Lasers and Amplifiers II*, 2006.

[14] N. P. Barnes, M. G. Jani, and R. L. Hutcheson, "Diode-pumped, room-temperature Tm:LuAG laser," *Appl. Opt.,* vol. 34, pp. 4290-4294, 1995.

[15] V. Petrov, F. Guell, J. Massons, J. Gavalda, R. M. Sole, M. Aguilo, F. Diaz, and U. Griebner, "Efficient tunable laser operation of Tm : KGd(WO4)(2) in the continuous-wave regime at room temperature," *IEEE Journal of Quantum Electronics,* vol. 40, pp. 1244-1251, 2004.

[16] H. Saito, S. Chaddha, R. S. F. Chang, and N. Djeu, "Efficient 1.94-μm Tm^{3+} laser in YVO_4 host," *Optics Letters,* vol. 17, pp. 189-191, 1992.

[17] L. Fornasiero, N. Berner, B. M. Dicks, E. Mix, V. Peters, K. Petermann, and G. Huber, "Broadly Tunable Laser Emission from Tm:Y2O3 and Tm:Sc2O3 at 2 μm," in *Advanced Solid State Lasers*, 1999, p. WD5.

[18] L. Fornasiero, N. Berner, B. M. Dicks, E. Mix, V. Peters, K. Petermann, and G. Huber, "Broadly Tunable Laser Emission from Tm:Y2O3 and Tm:Sc2O3 at 2 μm," 1999, p. WD5.

[19] P. Koopmann, S. Lamrini, K. Scholle, P. Fuhrberg, K. Petermann, and G. Huber, "Efficient diode-pumped laser operation of Tm:Lu2O3 around 2μm," *Opt. Lett.,* vol. 36, pp. 948-950, 2011.

[20] N. Coluccelli, G. Galzerano, P. Laporta, F. Cornacchia, D. Parisi, and M. Tonelli, "Tm-doped LiLuF4 crystal for efficient laser action in the wavelength range from 1.82 to 2.06 μm," *Opt. Lett.,* vol. 32, pp. 2040-2042, 2007.

[21] G. J. Quarles, A. Rosenbaum, C. L. Marquardt, and L. Esterowitz, "Efficient Room-Temperature Operation of a Flash-Lamp-Pumped, Cr,Tm-Yag Laser at 2.01 μm," *Optics Letters,* vol. 15, pp. 42-44, 1990.

[22] P. J. M. Suni and S. W. Henderson, "1-mJ/pulse Tm:YAG laser pumped by a 3-W diode laser," *Optics Letters,* vol. 16, pp. 817-819, 1991.

[23] E. C. Honea, R. J. Beach, S. B. Sutton, J. A. Speth, I. V. Mitchell, J. A. Skidmore, M. A. Emanuel, and S. A. Payne, "115-W Tm:YAG CW diode-pumped solid-state laser," *IEEE Journal of Quantum Electronics,* vol. 33, pp. 1592-1600, 1997.

[24] C. Bollig, R. A. Hayward, W. A. Clarkson, and D. C. Hanna, "2-W Ho : YAG laser intracavity pumped by a diode-pumped Tm : YAG laser," *Optics Letters,* vol. 23, pp. 1757-1759, NOV 15 1998.

[25] C. Gao, R. Wang, Z. Lin, M. Gao, L. Zhu, Y. Zheng, and Y. Zhang, "2 μm single-frequency Tm:YAG laser generated from a diode-pumped L-shaped twisted mode cavity," *Applied Physics B: Lasers and Optics,* vol. 107, pp. 67-70, 2012.

[26] C. Li, J. Song, D. Shen, N. S. Kim, and K.-i. Ueda, "Diode-pumped high-effiency Tm:YAG lasers," *Optics Express,* vol. 4, pp. 12-18, 1999.

[27] U. Demirbas, M. Schmalz, B. Sumpf, G. Erbert, G. S. Petrich, L. A. Kolodziejski, J. G. Fujimoto, F. X. Kärtner, and A. Leitenstorfer, "Femtosecond Cr:LiSAF and Cr:LiCAF lasers pumped by tapered diode lasers," *Opt. Express,* vol. 19, pp. 20444-20461, 2011.

[28] W. Denk, J. H. Strickler, and W. W. Webb, "2-Photon Laser Scanning Fluorescence Microscopy," *Science,* vol. 248, pp. 73-76, Apr 6 1990.

[29] W. R. Zipfel, R. M. Williams, and W. W. Webb, "Nonlinear magic: multiphoton microscopy in the biosciences," *Nature Biotechnology,* vol. 21, pp. 1368-1376, Nov 2003.

[30] C. Xu and W. W. Webb, "Measurement of two-photon excitation cross sections of molecular fluorophores with data from 690 to 1050 nm," *Journal of the Optical Society of America B-Optical Physics,* vol. 13, pp. 481-491, Mar 1996.

[31] S. Sakadzic, U. Demirbas, T. R. Mempel, A. Moore, S. Ruvinskaya, D. A. Boas, A. Sennaroglu, F. X. Kartner, and J. G. Fujimoto, "Multi-photon microscopy with a low-cost and highly efficient Cr:LiCAF laser," *Optics Express,* vol. 16, pp. 20848-20863, Dec 8 2008.

[32] A. Sennaroglu, *Photonics and laser engineering : principles, devices, and applications*. New York: McGraw-Hill, 2010.

[33] J. A. Caird, S. A. Payne, P. R. Staber, A. J. Ramponi, L. L. Chase, and W. F. Krupke, "Quantum electronic properties of the Na/sub 3/Ga/sub 2/Li/sub 3/F/sub 12/:Cr/sup 3+/ laser," *Quantum Electronics, IEEE Journal of,* vol. 24, pp. 1077-1099, 1988.

[34] D. Findlay and R. A. Clay, "The measurement of internal losses in 4-level lasers," *Physics Letters,* vol. 20, pp. 277-278, 1966.

[35] K. J. Weingarten, B. Braun, and U. Keller, "In situ small-signal gain of solid-state lasersdetermined from relaxation oscillation frequency measurements," *Optics Letters,* vol. 19, pp. 1140-1142, 1994/08/01 1994.

[36] B. Braun, F. X. Kartner, U. Keller, J.-P. Meyn, and G. Huber, "Passively Q -switched 180-ps Nd:$LaSc_3(BO_3)_4$ microchip laser," *Optics Letters,* vol. 21, pp. 405-407, 15 March 1996 1996.

[37] B. Braun, F. X. Kartner, G. Zhang, M. Moser, and U. Keller, "56-ps passively Q-switched diode-pumped microchip laser," *Optics Letters,* vol. 22, pp. 381-383, 15 March 1997 1997.

[38] T. Bilici, H. O. Tabakoglu, N. Topaloglu, H. Kalaycioglu, A. Kurt, A. Sennaroglu, and M. Gulsoy, "Modulated and continuous-wave operations of low-power thulium (Tm:YAP) laser in tissue welding," *Journal of Biomedical Optics,* vol. 15, p. 038001, 2010.

[39] D. P. Poppas, S. M. Schlossberg, I. L. Richmond, D. A. Gilbert, and C. J. Devine, "Laser-Welding in Urethral Surgery - Improved Results with a Protein Solder," *Journal of Urology,* vol. 139, pp. 415-417, FEB 1988.

[40] M. Talmor, C. B. Bleustein, and D. P. Poppas, "Laser tissue welding: a biotechnological advance for the future," *Archieves Facial Plastic Surgery,* vol. 3, pp. 207-213, 2001.

[41] R. Targ, B. C. Steakley, J. G. Hawley, L. L. Ames, P. Forney, D. Swanson, R. Stone, R. G. Otto, V. Zarifis, P. Brockman, R. S. Calloway, S. H. Klein, and P. A. Robinson, "Coherent lidar airborne wind sensor II: flight-test results at 2 and 10 vm," *Appl. Opt.,* vol. 35, pp. 7117-7127, 1996.

[42] K. Scholle, E. Heumann, and G. Huber, "Single mode Tm and Tm,Ho:LuAG lasers for LIDAR applications," *Laser Physics Letters,* vol. 1, pp. 285-290, 2004.

[43] P. A. Budni, L. A. Pomeranz, C. A. Miller, B. K. Dygan, M. L. Lemons, and E. P. Chickles, "CW and Q-switched Ho:YAG pumped by Tm:YALO," in *OSA Trends in Optics and Photonics on Advanced Solid State Lasers*, Washington, DC, 1998, pp. 204-205.

[44] P. A. Budni, L. A. Pomeranz, M. L. Lemons, C. A. Miller, J. R. Mosto, and E. P. Chicklis, "Efficient mid-infrared laser using 1.9-μm pumped Ho:YAG and $ZnGeP_2$ optical parametric oscillators," *J. Opt. Soc. Amer. B,* vol. 17, pp. 723-728, 2000.

[45] L. A. Pomeranz, P. A. Ketteridge, P. A. Budni, K. M. Ezzo, D. M. Rines, and E. P. Chicklis, "Tm:$YALO_3$ Laser Pumped ZGP Mid-IR Source," in *OSA TOPS on Advanced Solid-State Photonics*, 2003, p. 142.

[46] A. Sennaroglu, A. Kurt, and G. Özen, "Effect of cross relaxation on the 1470 and 1800 nm emissions in Tm^{3+}:TeO_2-$CdCl_2$ glass," *Journal of Physics: Condensed Matter,* vol. 16, pp. 2471-2478, 2004.

[47] J. F. Pinto and L. Esterowitz, "Tunable, flashlamp-pumped operation of a Cr;Tm:YAG laser between 1.945 and 2.014 μm," in *Advanced Solid-State Lasers*, Salt Lake City, Utah, 1990.

[48] G. J. Quarles, J. F. Pinto, and L. Esterowitz, "Broad Tunability of Flashlamp-Pumped, Tm-Activated Garnet Lasers," in *Advanced Solid-State Lasers*, Hilton Head, SC, 1991, pp. 167-171.

[49] L. F. Johnson, J. E. Geusic, and L. G. Van Uitert, "COHERENT OSCILLATIONS FROM Tm3+, Ho3+, Yb3+ and Er3+ IONS IN YTTRIUM ALUMINUM GARNET," *Applied Physics Letters,* vol. 7, pp. 127-129, 1965.

[50] E. D. Filer, N. P. Barnes, and C. A. Morrison, "Theoretical Temperature-Dependent Branching Ratios and Laser Thresholds of the 3F4 to 3H6 Levels of Tm3+ in Ten Garnets," in *Advanced Solid State Lasers*, Hilton Head, South Carolina, 1991, p. MIL8.

[51] F. Cornacchia, D. Parisi, C. Bernardini, A. Toncelli, and M. Tonelli, "Efficient, diode-pumped Tm3+:BaY2F8 vibronic laser," *Opt. Express,* vol. 12, pp. 1982-1989, 2004.

[52] T. Bach, T. R. W. Herrmann, C. Cellarius, and A. J. Gross, "Bladder neck incision using a 70 W 2 micron continuous wave laser (RevoLix)," *World Journal of Urology,* vol. 25, pp. 263-267, JUN 2007.

[53] E. D. Filer, N. P. Barnes, and C. A. Morrison, "Theoretical Temperature-Dependent Branching Ratios and Laser Thresholds of the $^3F_4$ to $^3H_6$ Levels of Tm^{3+} in ten Garnets," in *Advanced Solid-State Lasers*, 1991, pp. 189-200.

[54] I. Freund, "SELF-Q-SWITCHING IN RUBY LASERS," *Applied Physics Letters,* vol. 12, pp. 388-&, 1968.

[55] R. J. Collins, L. O. Braun, and D. R. Dean, "A NEW METHOD OF GIANT PULSING RUBY LASERS," *Applied Physics Letters,* vol. 12, pp. 392-&, 1968.

[56] M. Birnbaum and C. L. Fincher, "THE RUBY LASER: PUMPED BY A PULSED ARGON ION LASER " *Applied Physics Letters,* vol. 12, pp. 225-227, 1968.

[57] A. Szabo and L. E. Erickson, "SELF-Q-SWITCHING OF RUBY LASERS AT 77 DEGREES K," *IEEE Journal of Quantum Electronics,* vol. QE 4, pp. 692-&, 1968.

[58] H. Samelson, A. Lempicki, and V. Brophy, "SELF-Q-SWITCHING OF ND3+ SEOCL2 LIQUID LASER," *Journal of Applied Physics,* vol. 39, pp. 4029-&, 1968.

[59] M. Birnbaum and C. L. Fincher, "SELF-Q-SWITCHED ND3+ - YAG AND RUBY LASERS," *Proceedings of the IEEE,* vol. 57, pp. 804-&, 1969.

[60] A. L. Mikaelyan, V. F. Kuprishov, Y. G. Turkov, Y. V. Andreev, and A. A. Shcherbakova, "New Method for Generating a Giant Pulse in Optical Generators," *Journal of Experimental and Theoretical Physics Letters,* vol. 11, pp. 155-157, 1970.

[61] Z. Zalevsky, Y. Kapellner, I. Eyal, and N. Cohen, "Self Q-switching effect in a Nd : YVO4/KTP lasing unit," *Optical Engineering,* vol. 45, Jul 2006.

[62] A. Szabo, "REPETITIVE SELF-Q-SWITCHING IN A CONTINUOUSLY PUMPED RUBY-LASER," *Journal of Applied Physics,* vol. 49, pp. 533-538, 1978.

[63] B. C. Weber and A. Hirth, "Presentation of a new and simple technique of Q-switching with a LiSrAlf(6): Cr3+ oscillator," *Optics Communications,* vol. 149, pp. 301-306, Apr 15 1998.

[64] R. S. Conroy, T. Lake, G. J. Friel, A. J. Kemp, and B. D. Sinclair, "Self-Q-switched Nd:YVO_4 microchip lasers," *Optics Letters,* vol. 23, pp. 457-459, March 15, 1998 1998.

[65] A. V. Kir'yanov, N. N. Il'ichev, and Y. O. Barmenkov, "Excited-state absorption as a source of nonlinear thermo-induced lensing and self-Q-switching in an all-fiber Erbium laser," *Laser Physics Letters,* vol. 1, pp. 194-198, 2004.

[66] S. Wolff, A. Rodionov, V. E. Sherstobitov, C. Doering, and H. Fouckhardt, "Self-pulsation in broad area lasers with transverse-mode selective feedback," *Optics Communication,* vol. 265, pp. 642-648, 2006.

[67] B. N. Upadhyaya, A. Kuruvilla, U. Chakravarty, M. R. Shenoy, K. Thyagarajan, and S. M. Oak, "Effect of laser linewidth and fiber length on self-pulsing dynamics and output stabilization of single-mode Yb-doped double-clad fiber laser," *Applied Optics,* vol. 49, pp. 2316-2325, 2010.

[68] Y. Tang and J. Xu, "Effects of excited-state absorption on self-pulsing in Tm3+-doped fiber lasers," *Journal of Optical Society of America B,* vol. 27, pp. 179-186 2010.

[69] N. Passilly, E. Haouas, V. Ménard, R. Moncorgé, and K. Aı¨t-Ameur, "Population lensing effect in Cr:LiSAF probed by Z-scan technique," *Optics Communications,* vol. 260, pp. 703–707, 2006.

[70] N. Passilly, M. Fromager, and K. Ait-Ameur, "Improvement of the self-Q-switching behavior of a Cr : LiSrAlF6 laser by use of binary diffractive optics," *Applied Optics,* vol. 43, pp. 5047-5059, Sep 10 2004.

[71] N. Passilly, M. Fromager, K. Ait-Ameur, R. Moncorge, J. L. Doualan, A. Hirth, and G. Quarles, "Experimental and theoretical investigation of a rapidly varying nonlinear lensing effect observed in a Cr3+: LiSAF laser," *Journal of the Optical Society of America B-Optical Physics,* vol. 21, pp. 531-538, Mar 2004.

[72] M. Fromager and K. A. Ameur, "Modeling of the self-Q-switching behavior of lasers based on chromium doped active material," *Optics Communications,* vol. 191, pp. 305-314, May 8 2001.

[73] T. Godin, R. Moncorgé, J.-L. Doualan, M. Fromager, K. Ait-Ameur, R. A. Cruz, and T. Catunda, "Optically pump-induced athermal and nonresonant refractive index changes in the reference Cr-doped laser materials: Cr:GSGG and ruby," *Journal of Optical Society of America B,* vol. 29, pp. 1055-1064, 2012.

[74] S. A. Payne, L. L. Chase, H. W. Newkirk, L. K. Smith, and W. F. Krupke, "$LiCaAlF_6:Cr^{3+}$ a promising new solid-state laser material," *IEEE Journal of Quantum Electronics,* vol. 24, pp. 2243-2252, Nov 1988.

[75] J. J. Deyoreo, L. J. Atherton, and D. H. Roberts, "Elimination of Scattering Centers from Cr-Licaalf6," *Journal of Crystal Growth,* vol. 113, pp. 691-697, Sep 1991.

[76] D. Klimm and P. Reiche, "Nonstoichiometry of the new laser host LiCaAlF6," *Crystal Research and Technology,* vol. 33, pp. 409-416, 1998.

[77] D. Klimm, R. Uecker, and P. Reiche, "Melting behavior and growth of colquiriite laser crystals," *Crystal Research and Technology,* vol. 40, pp. 352-358, 2005.

[78] U. Demirbas, R. Uecker, D. Klimm, and J. Wang, "A low-cost, broadly-tunable (375-433 nm & 746-887 nm) Cr:LiCAF laser pumped by one single-spatial-mode diode " *Applied Optics,* vol. 51, pp. 8440-8448, 2012.

[79] J. G. Fujimoto, C. Pitris, S. A. Boppart, and M. E. Brezinski, "Optical Coherence Tomography: An Emerging Technology for Biomedical Imaging and Optical Biopsy," *Neoplasia,* vol. 2, pp. 9-25, 2000.

[80] U. Demirbas, M. Schmalz, B. Sumpf, G. Erbert, G. S. Petrich, L. A. Kolodziejski, J. G. Fujimoto, F. X. Kärtner, and A. Leitenstorfer, "Femtosecond Cr:LiSAF and Cr:LiCAF lasers pumped by tapered diode lasers," *Optics Express,* vol. 19, pp. 20444-20461, 2011.

[81] U. Demirbas, A. Sennaroglu, F. X. Kartner, and J. G. Fujimoto, "Comparative investigation of diode pumping for continuous-wave and mode-locked Cr3+ : LiCAF lasers," *Journal of the Optical Society of America B-Optical Physics,* vol. 26, pp. 64-79, Jan 2009.

[82] A. W. Tucker, M. Birnbaum, C. L. Fincher, and L. G. DeShazer, "Continuous-wave operation of Nd:YVO_4 at 1.06 and 1.34 m," *Journal of Applied Physics,* vol. 47, pp. 232-234, 1 January, 1976 1976.

[83] L. G. DeShazer and K. W. Kangas, "Extended infared operation of titanium sapphire laser," *Conference on Lasers and Electro Optics,* vol. 14, pp. 296-298, 1987.

[84] R. Ell, U. Morgner, F. X. Kärtner, J. G. Fujimoto, E. P. Ippen, V. Scheuer, G. Angelow, and T. Tschudi, "Generation of 5 fs pulses and octave-spanning spectra directly from a Ti:sapphire laser," *Optics Letters,* vol. 26, pp. 373-375, 2001.

[85] P. F. Moulton, "Spectroscopic and laser characteristics of Ti:Al_2O_3," *JOSA B,* vol. 3, pp. 125-133, 1986.

[86] P. W. Roth, A. J. Maclean, D. Burns, and A. J. Kemp, "Directly diode-laser-pumped Ti:sapphire laser," *Optics Letters,* vol. 34, pp. 3334-3336, 2009.

[87] M. D. Young, S. Backus, C. Durfee, and J. Squier, "Multiphoton imaging with a direct-diode pumped femtosecond Ti:sapphire laser," *Journal of Microscopy,* vol. 249, pp. 83-86, Feb 2013.

[88] C. G. Durfee, T. Storz, J. Garlick, S. Hill, J. A. Squier, M. Kirchner, G. Taft, K. Shea, H. Kapteyn, M. Murnane, and S. Backus, "Direct diode-pumped Kerr-lens mode-locked Ti:sapphire laser," *Optics Express,* vol. 20, pp. 13677-13683, Jun 18 2012.

[89] P. W. Roth, A. J. Maclean, D. Burns, and A. J. Kemp, "Direct diode-laser pumping of a mode-locked Ti:Sapphire laser," *Optics Letters,* vol. 36, pp. 304-306, 2011.

[90] P. W. Roth, D. Burns, and A. J. Kemp, "Power scaling of a directly diode-laser-pumped Ti:sapphire laser," *Optics Express,* vol. 20, pp. 20629-20634, Aug 27 2012.

[91] A. Müller, O. B. Jensen, A. Unterhuber, T. Le, A. Stingl, K.-H. Hasler, B. Sumpf, G. Erbert, P. E. Andersen, and P. M. Petersen, "Frequency-doubled DBR-tapered diode laser for direct pumping of Ti:sapphire lasers generating sub-20 fs pulses," *Optics Express,* vol. 19, pp. 12156-12163, 2011.

[92] S. A. Payne, L. L. Chase, L. K. Smith, W. L. Kway, and H. W. Newkirk, "Laser performance of $LiSAIF_6:Cr^{3+}$," *Journal of Applied Physics,* vol. 66, pp. 1051-1056, 1989.

[93] L. K. Smith, S. A. Payne, W. L. Kway, L. L. Chase, and B. H. T. Chai, "Investigation of the laser properties of Cr^{3+}:$LiSrGaF_6$," *IEEE Journal of Quantum Electronics,* vol. 28, pp. 2612-2618, 1992.

[94] Z. Chen and G. Zhang, "Free-running emerald laser pumped by laser diode," *CHINESE OPTICS LETTERS,* vol. 4, pp. 649-651, 2006.

[95] S. T. Lai, "Highly Efficient Emerald Laser," *Journal of the Optical Society of America B-Optical Physics,* vol. 4, pp. 1286-1290, Aug 1987.

[96] J. C. Walling, "Tunable Cw Alexandrite Lasers," *Journal of the Optical Society of America,* vol. 69, pp. 1436-1436, 1979.

[97] J. C. Walling, H. P. Jenssen, R. C. Morris, E. W. O'Dell, and O. G. Peterson, "Tunable laser performance in $BeAl_2O_4Cr^{3+}$," *Optics Letters,* vol. 4, pp. 182-183, 1979.

[98] J. C. Walling, O. G. Peterson, H. P. Jenssen, R. C. Morris, and E. W. Odell, "Tunable Alexandrite Lasers," *IEEE Journal of Quantum Electronics,* vol. 16, pp. 1302-1315, 1980.

[99] J. C. Walling, D. F. Heller, H. Samelson, D. J. Harter, J. A. Pete, and R. C. Morris, "Tunable Alexandrite Lasers - Development and Performance," *IEEE Journal of Quantum Electronics,* vol. 21, pp. 1568-1581, 1985.

[100] O. Svelto, *Principles of Lasers*. New York: Plenum Press, 1989.

[101] E. Sorokin, "Solid-state materials for few-cycle pulse generation and amplification," in *Few-cycle laser pulse generation and its applications*. vol. 95, F. X. Kartner, Ed., ed Berlin: Springer-Verlag, 2004, pp. 3-71.

[102] U. Demirbas, D. Li, J. R. Birge, A. Sennaroglu, G. S. Petrich, L. A. Kolodziejski, F. X. Kärtner, and J. G. Fujimoto, "Low-cost, single-mode diode-pumped Cr:Colquiriite lasers " *Optics Express,* vol. 17, pp. 14374-14388, 2009.

[103] J. W. Kuper, T. Chin, and H. E. Aschoff, "Extended tuning of Alexandrite laser at elevated temperetures," presented at the Advanced Solid State Lasers, Salt Lake City, Utah, 1990.

[104] F. Druon, F. Balembois, and P. Georges, "New laser crystals for the generation of ultrashort pulses," *Comptes Rendus Physique,* vol. 8, pp. 153-164, Mar 2007.

[105] A. Sanchez, R. E. Fahey, A. J. Strauss, and R. L. Aggarwal, "Room-temperature continuous-wave operation of a Ti:Al_2O_3 laser," *Optics Letters,* vol. 11, pp. 363-364, Jun 1986.

[106] R. Scheps, J. F. Myers, T. R. Glesne, and H. B. Serreze, "Monochromatic End-Pumped Operation Of An Alexandrite Laser," *Optics Communications,* vol. 97, pp. 363-366, Apr 1993.

[107] J. K. Jabczynski, W. Zendzian, Z. Mierczyk, and Z. Frukacz, "Chromium-Doped LiCAF Laser Passively Q Switched with a V^{3+}:YAG Crystal," *Applied Optics,* vol. 40, pp. 6638-6645, 20 December 2001 2001.

[108] M. L. Shand and J. C. Walling, "Excited-State Absorption in the Lasing Wavelength Region of Alexandrite," *IEEE Journal of Quantum Electronics,* vol. 18, pp. 1152-1155, 1982.

[109] U. Demirbas, R. Uecker, D. Klimm, and J. Wang, "Low-cost, broadly tunable (375-433 nm & 746-887 nm) Cr:LiCAF laser pumped by one single-spatial-mode diode," *Applied Optics,* vol. 51, pp. 8440-8448, 2012.

[110] L. J. Atherton, S. A. Payne, and C. D. Brandle, "Oxide and Fluoride Laser Crystals," *Annual Review of Materials Science,* vol. 23, pp. 453-502, 1993.

[111] M. Stalder, M. Bass, and B. H. T. Chai, "Thermal quenching of fluoresence in chromium-doped fluoride laser crystals," *Journal of Optical Society of America B,* vol. 9, pp. 2271-2273, 1992.

[112] J. M. Eichenholz and M. Richardson, "Measurement of thermal lensing in Cr^{3+}-doped colquiriites," *IEEE Journal of Quantum Electronics,* vol. 34, pp. 910-919, May 1998.

[113] J. C. Walling, O. G. Peterson, and R. C. Morris, "Tunable Cw Alexandrite Laser," *IEEE Journal of Quantum Electronics,* vol. 16, pp. 120-121, 1980.

[114] H. Samelson and D. J. Harter, "High-pressure mercury arc lamp excited cw alexandrite lasers," presented at the CLEO, Anaheim, CA, 1984.

[115] S. T. Lai and M. L. Shand, "High efficiency cw laser-pumped tunable alexandrite laser," *J. Appl. Phys.,* vol. 54, pp. 56642-56644, 1984.

[116] J. W. Kuper and D. C. Brown, "Green pumped Alexandrite Lasers," in *Solid State Lasers XIV:Technology and Devices*, Bellingham, WA, 2005, pp. 265-270.

[117] J. W. Kuper and D. C. Brown, "Higly efficient CW green pumped Alexandrtie Lasers," in *Solid State Lasers XV:Technology and Devices*, 2006.

[118] M. Lando, Y. Shimony, R. M. J. Benmair, D. Abramovich, V. Krupkin, and A. Yogev, "Visible solar-pumped lasers," *Optical Materials,* vol. 13, pp. 111-115, 1999.

[119] R. Scheps, B. M. Gately, J. F. Myers, J. S. Krasinski, and D. F. Heller, "Alexandrite Laser Pumped by Semiconductor-Lasers," *Applied Physics Letters,* vol. 56, pp. 2288-2290, Jun 1990.

[120] X. Peng, A. Marrakchi, J. C. Walling, and D. F. Heller, "Watt-level red and UV outputfrom a CW diode array-pumped tunable alexandrite laser," presented at the Lasers and Electro-Optics, 2005.

[121] M. J. Damzen, G. M. Thomas, and A. Minassian, "Multi-watt diode-pumped alexandrite laser operation," presented at the CLEO Europe, Munich, 2013.

[122] B. Sumpf, P. Adamiec, M. Zorn, H. Wenzel, and G. Erbert, "Nearly Diffraction Limited Tapered Lasers at 675 nm with 1 W Output Power and conversion efficiencies above 30%," *IEEE Photonics Technology Letters,* vol. 22, pp. 266-268, 2011.

[123] E. Beyatlı, A. Sennaroglu, and U. Demirbas, "Self-Q-Switched Cr:LiCAF Laser," *Journal of Optical Society of America B,* vol. 30, pp. 914-921, 2013.

[124] U. Demirbas, S. Eggert, and A. Leitenstorfer, "Compact and efficient Cr:LiSAF lasers pumped by one single-spatial-mode diode: a minimal cost approach," *Journal of Optical Society of America B,* vol. 29, pp. 1894-1903, 2012.

[125] K. Torizuka, M. Yamashita, and T. Yabiku, "Continuous-Wave Alexandrite Laser-Pumped by a Direct-Current Mercury Are Lamp," *Applied Optics,* vol. 32, pp. 7394-7398, Dec 20 1993.

[126] J. W. Kuper, T. Chin, and H. E. Aschoff, "Extended Tuning Range of Alexandrite at Elevated Temperatures," 1990, p. CL3.

[127] R. C. Powell, L. Xi, X. Gang, G. J. Quarles, and J. C. Walling, "Spectroscopic Properties of Alexandrite Crystals," *Physical Review B,* vol. 32, pp. 2788-2797, 1985.

[128] A. B. Suchocki, G. D. Gilliland, R. C. Powell, J. M. Bowen, and J. C. Walling, "Spectroscopic Properties of Alexandrite Crystals .2.," *Journal of Luminescence,* vol. 37, pp. 29-37, Apr 1987.

[129] E. Beyatli, I. Baali, B. Sumpf, G. Erbert, A. Leitenstorfer, A. Sennaroglu, and U. Demirbas, "Tapered diode-pumped continuous-wave alexandrite laser," *Journal of Optical Society of America B,* vol. 30, pp. 3184-3192, 2013.

[130] U. Demirbas, "Modeling and optimization of tapered-diode pumped Cr:LiCAF regenerative amplifiers," *Optics Communication,* vol. 311, pp. 90-99, 2013.

[131] M. L. Shand and H. P. Jenssen, "Temperature-Dependence of the Excited-State Absorption of Alexandrite," *Ieee Journal of Quantum Electronics,* vol. 19, pp. 480-484, 1983.

[132] D. E. Spence, Kean, P. N., Sibbett, W., "60-fsec pulse generation from a self-mode-locked Ti:sapphire laser," *Optics Letters,* vol. 16, 1991.

[133] M. N. Cizmeciyan, H. Cankaya, A. Kurt, and A. Sennaroglu, "Kerr-lens mode-locked femtosecond Cr^{2+}:ZnSe laser at 2420 nm," *Optics Letters,* vol. 34, pp. 3056-3058, 2009.

[134] H. Cankaya, J. G. Fujimoto, and A. Sennaroglu, "Low-threshold, 12-MHz, multipass-cavity femtosecond Cr4+:forsterite laser," *Laser Physics,* vol. 19, pp. 281–284, 2009 2009.

[135] S. Uemura and K. Torizuka, "Generation of 10 fs pulses from a diode-pumped Kerr-lens mode-locked Cr : LiSAF laser," *Japanese Journal of Applied Physics Part 1-Regular Papers Short Notes & Review Papers,* vol. 39, pp. 3472-3473, Jun 2000.

[136] P. C. Wagenblast, U. Morgner, F. Grawert, T. R. Schibli, F. X. KÃÂrtner, V. Scheuer, G. Angelow, and M. J. Lederer, "Generation of sub-10-fs pulses from a Kerr-lens mode-locked Cr3+:LiCAF laser oscillator by use of third-order dispersion-compensating double-chirped mirrors," *Opt. Lett.,* vol. 27, pp. 1726-1728, 10/01 2002.

[137] L. J. Chen, M. Y. Sander, and F. X. Kartner, "Kerr-lens mode locking with minimum nonlinearity using gain-matched output couplers," *Optics Letters,* vol. 35, pp. 2916-2918, Sep 1 2010.

[138] N. P. Barry, S. C. W. Hyde, R. Mellish, P. M. W. French, J. R. Taylor, C. J. van der Poel, and A. Valster, "All-solid-state femtosecond diode-pumped Cr:LiSAF regenerative amplifier," *Electronics Letters,* vol. 30, pp. 1761-1762, 1994.

[139] A. Robertson, R. Knappe, and R. Wallenstein, "Diode-pumped broadly tunable (809–910 nm) femtosecond Cr:LiSAF laser," *Optics Communications,* vol. 147, pp. 294-298, 2/15/ 1998.

[140] U. Demirbas, G. S. Petrich, S. Nabanja, J. R. Birge, L. A. Kolodziejski, F. X. Kärtner, and J. G. Fujimoto, "Widely-tunable femtosecond operation of Cr:LiSAF lasers using broadband saturable Bragg reflectors," presented at the CLEO, San Jose, California, 2010.